THE HONG KONG POLYTECHNIC UNIVERSITY
香港理工大學
Pao Yue-kong Library
包玉剛圖書館

Copyright Undertaking

This thesis is protected by copyright, with all rights reserved.

By reading and using the thesis, the reader understands and agrees to the following terms:

1. The reader will abide by the rules and legal ordinances governing copyright regarding the use of the thesis.
2. The reader will use the thesis for the purpose of research or private study only and not for distribution or further reproduction or any other purpose.
3. The reader agrees to indemnify and hold the University harmless from and against any loss, damage, cost, liability or expenses arising from copyright infringement or unauthorized usage.

If you have reasons to believe that any materials in this thesis are deemed not suitable to be distributed in this form, or a copyright owner having difficulty with the material being included in our database, please contact lbsys@polyu.edu.hk providing details. The Library will look into your claim and consider taking remedial action upon receipt of the written requests.

Pao Yue-kong Library, The Hong Kong Polytechnic University, Hung Hom, Kowloon, Hong Kong

http://www.lib.polyu.edu.hk

PREPARATION AND CHARACTERIZATION OF SOL-GEL DERIVED NIOBIUM-DOPED LEAD ZIRCONATE TITANATE FILMS FOR MEMBRANE-ACTUATOR APPLICATIONS

SUBMITTED BY

KWOK KIN PONG

A THESIS SUBMITTED IN PARTIAL FULFILMENT

OF THE REQUIREMENTS FOR THE DEGREE OF

MASTER OF PHILOSOPHY IN PHYSICS

AT

THE DEPARTMENT OF APPLIED PHYSICS

THE HONG KONG POLYTECHNIC UNIVERSITY

AUGUST, 2003

Pao Yue-kong Library
PolyU • Hong Kong

CERTIFICATE OF ORIGINALITY

I hereby declare that this thesis is my own work and that, to the best of my knowledge and belief, it reproduces no material previously published or written nor material which has been accepted for the award of any other degree or diploma, except where due acknowledgement has been made in the text.

_______________________(Signed)

Kwok Kin Pong___________(Name of student)

Table of Contents

Table of Contents i

Abstract iv

Acknowledgement vi

List of Symbols vii

List of Figures viii

List of Tables xv

Chapter One Introduction

1.1 General background 1-1

1.2 Piezoelectric ceramics 1-4

1.2.1 Barium titanate $BaTiO_3$ 1-5

1.2.2 Lead zirconate titanate $Pb(Zr,Ti)O_3$ 1-5

1.3 Piezoelectric thin films 1-11

1.3.1 Techniques for deposition of thin film 1-13

1.3.2 Seeding layer 1-15

1.3.3 Doping effect 1-17

1.4 Microelectromechanical systems 1-20

1.4.1 Lithography 1-22

1.4.2 Light source 1-23

1.4.3 Photomask 1-25

1.4.4 Photoresist 1-26

1.4.5 Exposure systems 1-27

1.4.6 Etching 1-29

1.4.6.1 Wet etching 1-31

1.4.6.2 Dry etching 1-32

1.5 Scope of work 1-33

Chapter Two Preparation and Characterization of PZT Films

2.1 Preparation of lead titanate precursor solutions 2-2

2.2 Deposition of sol-gel films 2-6

2.3 Deposition of top electrodes 2-7

2.3 Crystallite structure of PZT films 2-8

2.4 Microstructure of PZT films 2-12

2.5 Dielectric properties of PZT films 2-13

Chapter Three Effects of Nb Dopant on Piezoelectric Properties of PZT films

3.1 Measurement of longitudinal piezoelectric coefficient 3-1

3.1.1 Sample preparation for the d_{33} measurement 3-5

3.2 Measurement of effective transverse piezoelectric coefficient 3-8

3.3 Result and discussion 3-15

Chapter Four   Fabrication of Silicon-based Membranes

4.1 Fabrication of Silicon-based Membranes 4-1

Chapter Five   Evaluation of Silicon-based Membranes

5.1 Resonance frequency of Silicon-based Membranes 5-1

5.2 Surface displacement of Silicon-based Membranes 5-5

5.3 Signal capture by Silicon-based Membranes 5-13

Chapter Six   Conclusions

References R-1

List of Publication P-1

Abstract

In recent years, lead zirconate titanate (PZT) thin films have been widely studied for use in actuator and sensor applications. In this work, sol-gel derived Nb-doped PZT films have been prepared at a low sintering temperature, and the effects of the Nb dopant on the piezoelectric properties of the PZT films have been studied. The Nb-doped PZT film has been fabricated into micromachined membranes and their performance has been evaluated.

Sol-gel derived Nb-doped PZT films were deposited on $Pt/Ti/SiO_2/Si/Si_3N_4$ substrates with a lead titanate seeding layer by the multiple-spin-coating technique. The doping level of Nb ranged from 0 % to 2 %; and the film thickness was about 800 nm. Because of the seeding layer, the PZT films could crystallize well and completely into the perovskite phase at a low sintering temperature of 550°C for 2 hours. The films were dense and crack-free, and had good dielectric and piezoelectric properties.

Effective longitudinal and transverse piezoelectric coefficients (d_{33}' and $e_{31,f}$) of the films have been measured using a single beam laser interferometer and a newly established method based on the direct piezoelectric effect, respectively; and the effects of Nb dopant on d_{33}' and $e_{31,f}$ of the PZT films have been studied. Our results reveal that the Nb dopant has effects on the PZT films similar to the experimentally-known effects on bulk ceramics, i.e. enhancing both the longitudinal

and transverse piezoelectric properties; and the optimum doping level of Nb is about 1%. However, because of the substrate clamping effect, the observed enhancement in the d'_{33} was much smaller than that in $e_{31,f}$. At 1% Nb-doping level, the observed d'_{33} and $e_{31,f}$ values of the film are increased, by about 9% and 30%, to 74 pm/V and 12.8 C/m^2, respectively.

The 1 % Nb-doped PZT film has been fabricated into 3-mm and 4-mm square micromachined membranes, and their performance have been evaluated. The observed fundamental resonance frequencies for the membranes are 111.5 kHz and 65 kHz, respectively. At resonance, the vibrating displacements at the centre of the membranes have the maximum values of 200 nm/V and 900 nm/V, respectively. At off-resonance frequencies, the displacements are about 6.8 nm/V and 10.5 nm/V, respectively, and can be increased reversibly by about 40-50% under a dc bias field of 16 MV/m. These results indicate that the silicon-based membranes are suitable for micro-actuator applications.

Acknowledgments

I would like to express my deepest appreciation to my supervisors Dr. K. W. Kwok and Prof. H.L.W. Chan for their excellent guidance and encouragement throughout the whole period of the research work.

I would like to thank Dr. N. Chong and Dr. Y. Wang for their assistance in the process of the micro fabrication. Their helpful suggestions are also appreciated.

I would also like to give my thanks to colleagues and friends Mr. Rodney C. W. Tsang, Mr. S. F. Wong, Ms. Y. L. Cheng and Ms. M. K. Cheung for their assistant in experimental and technical supports.

I gratefully acknowledge the financial support from the Hong Kong Polytechnic University and the technical support provided by the Centre of Smart Materials of the Hong Kong Polytechnic University.

The last but not least, I would like to thank my parents for their understanding and constant support.

List of Symbols

I	Current
ρ	Density
$\tan\delta$	Dielectric loss
d'_{33}	Effective longitudinal piezoelectric coefficient
$e_{31,f}$	Effective transverse piezoelectric coefficient
s^{E}_{pq}	Elastic compliance at constant electric field
k_p	Electromechanical coupling factor
D	Electric displacement
E	Electric field
d_{33}	Longitudinal piezoelectric coefficient
ε_0	Permittivity of free space
υ_c	Poisson's ratio
P_r	Remanent polarization
ε_r	Relative permittivity
X	Stress
x	Strain
e_{31}	Transverse piezoelectric coefficient
Y	Young's Modulus

List of Figures

		Page
Figure 1.1	The perovskite structure ABO_3, showed a cubic structure in paraelectric phase (a) and a tetragonal structure in ferroelectric phase (b) [D. Damjanovic, 1998].	1-4
Figure 1.2	Phase diagram of $Pb(Zr_{1-x}Ti_x) O_3$ solid solution showing the morphotropic phase boundary in the middle of the diagram which separates the tetragonal and rhombohedral ferroelectric phases. [B. Jaffe and Cook, 1971, p.136].	1-7
Figure 1.3	Variations of the piezoelectric coefficient d_{ij} with composition of PZT near the morphotropic phase boundary [B. Jaffe and Cook, 1971, p.143].	1-8
Figure 1.4	Variation of the remanent polarization P_r with composition of PZT near the morphotropic phase boundary [B. Jaffe and Cook, 1971, p.147].	1-8
Figure 1.5	Variations of the dielectric constant $\varepsilon/\varepsilon_o$ and electromechanical coupling factor k_p with composition of PZT at room temperature [B. Jaffe *et al.*, 1954].	1-9
Figure 1.6	The phase diagram of PZT ceramics [N.Setter, chapter 1, 2002].	1-11

Figure 1.7 Average grain size of seeded (continuous line) and unseeded (dotted line) sol-gel deposited PZT thin films [A. Seifert *et al.*, 1999]. 1-17

Figure 1.8 Dopant effect on the field-induced strain. Maximum strain and hysteresis in $(Pb_{0.73}Ba_{0.27})(Zr_{0.75}Ti_{0.25})O_3$-based ceramics. (a) Definition of the maximum strain and the degree of hysteresis, and (b) dopant effect on actuator parameter. [K. Uchino, chapter 3, p.62, 2000]. 1-20

Figure 1.9 Typical arc soured and surrounding optics. 1-25

Figure 1.10 Output spectrum of a high pressure mercury arc source, high-lighting and high-intensity lines used in photolithography [El-Kareh, 1995]. 1-26

Figure 1.11 Reticle polarity. (a) Clear-field, or correct positive. (b) Dark field, or correct negative. 1-27

Figure 1.12 Mask projection and lithography illustrating the difference between positive and negative photoresist. 1-28

Figure 1.13 Schematic of three optical lithographic techniques. (a) Contact, (b) Proximity and (c) Projection. 1-29

Figure 1.14 Definition of a patterned film by subtractive and additive processes. 1-31

Figure 1.15 Definition of two lateral etch dimensions, illustrated for isotropic etching. a is referred to etch bias and b as undercutting. 1-32

Figure 1.16	V-shaped groove formation in <100> silicon with anisotropic etching.	1-33
Figure 2.1	Flow chart for the preparation of PT precursor solution.	2-5
Figure 2.2	Schematic diagram of the magnetron sputtering chamber.	2-8
Figure 2.3	Diffraction of x-rays by planes of atoms (X-X' and Y-Y').	2-9
Figure 2.4	XRD pattern of the PZT (53/47) sample with 10% excess lead. The thickness of the film is 800 nm and the film is annealed at 550°C for 2 hours.	2-10
Figure 2.5	XRD pattern of the 1% Nb-doped PZT (1/53/47) sample with 10% excess lead. The thickness of the film is 800 nm and the film is annealed at 550°C for 2 hours.	2-11
Figure 2.6	XRD pattern of the 2% Nb-doped PZT (2/53/47) sample with 10% excess lead. The thickness of the film is 800 nm and the film is annealed at 550°C for 2 hours.	2-12
Figure 2.7	SEM micrograph of the cross section of the 1% Nb-doped PZT film. The thickness of the film is 800 nm.	2-13
Figure 3.1	Schematic diagram of the experimental setup for the $d_{33}^{'}$ measurement.	3-2:
Figure 3.2	Frequency spectrum of the signal current I recorded by a spectrum analyzer.	3-5
Figure 3.3	Bending of the substrate in the $d_{33}^{'}$ measurement.	3-7
Figure 3.4	Sample fixture for the $d_{33}^{'}$ measurement.	3-7

Figure 3.5 Experimental set-up for the $e_{31,f}$ measurement. 3-9

Figure 3.6 Schematic diagram showing the bending of the cantilever. *F* is the force applied by the actuator, *R* is the radius of curvature of the cantilever, *l* is the length of the cantilever, *b* is the width of the cantilever and *h* is the thickness of the cantilever. 3-12

Figure 3.7 Schematic diagram showing the position of a top circular electrode. 3-13

Figure 3.8 The sample fixture for the $e_{31,f}$ measurement. 3-15

Figure 3.9 Schematic diagram showing an as-prepared polycrystalline sample with random orientation of grains before poling, and an poled sample with the grains aligned to the field direction. 3-16

Figure 3.10 A schematic diagram of the experimental setup for sample poling. 3-17

Figure 3.11 Variation of the surface displacement with applied voltage for thee PZT film (with 0% Nb). The thickness of the film is 800 nm. 3-18

Figure 3.12 The arrangement of the electrodes for the d_{33}' measurement. 3-19

Figure 3.13 Distribution of the surface displacement across the PZT film sample. The driving electrode (indicated by the dot lines) is located at centre. 3-20

Figure 3.14 Effective piezoelectric coefficient d'_{33} as a function of Nb-dopant content for the PZT films. The thickness of the films is 800 nm. 3-22

Figure 3.15 Induced current as a function of the deflection at the free end of the cantilever for the 0% Nb doped PZT film. 3-23

Figure 3.16 Effective piezoelectric coefficient $e_{31,f}$ as a function of Nb-dopant content for the PZT films. The thickness of the films is 800 nm. 3-24

Figure 4.1 The main process flow for the fabrication of silicon-based membrane. 4-5

Figure 4.2 (a) The pattern of backside window
(b) the pattern of electrode on the photomask. 4-6

Figure 4.3 The mechanical chuck used in the KOH wet etching. 4-7

Figure 4.4 (a) The top view of the silicon-based membrane.
(b) The backside window of the silicon-based membrane. 4-8

Figure 5.1 Impedance spectra for the 3 mm × 3 mm × 80 μm silicon-based membrane. 5-3

Figure 5.2 Impedance spectra for the 4 mm × 4 mm × 80 μm silicon-based membrane. 5-4

Figure 5.3 Sample fixture for measuring the surface displacement of the silicon-based membrane. 5-6

Figure 5.4 Figure 5.4 Variation of the surface displacement with applied voltage for the 3-mm membrane and 4-mm silicon-based membranes. 5-7

Figure 5.5 Surface displacement at the center of the membrane as a funtion of dc bias voltage for the 3-mm square membranes. The dc bias voltage increases from 0 V to 15 V (solid square symbol), then decreases from 15 V to -15V (open square symbol), and finally increases from -15 V to 15 V (solid circle symbol). 5-9

Figure 5.6 Surface displacement at the center of the membrane as a funtion of dc bias voltage for the 4-mm square membranes. The dc bias voltage increases from 0 V to 15 V (solid square symbol), then decreases from 15 V to -15V (open square symbol), and finally increases from -15 V to 15 V (solid circle symbol). 5-10

Figure 5.7 Surface displacement at the center of the 3 mm × 3 mm × 80 μm silicon-based membrane as a function of frequency. The amplitude of the driving voltage is 0.1 V. 5-12

Figure 5.8 Surface displacement at the center of the 4 mm × 4 mm × 80 μm silicon-based membrane as a function of frequency. The amplitude of the driving voltage is 0.1 V. 5-13

Figure 5.9 The experimental setup for the measurement of the output voltage of the membranes. 5-10

Figure 5.10 The output voltage signal by the 3-mm membrane. 5-11

Figure 5.11 The output voltage signal by the 4-mm membrane. 5-11

List of Tables

Page

Table 1.1 The dielectric constant, dissipation factor DF, radial coupling coefficient k_r and transverse piezoelectric coefficient d_{31} of ceramic with different batch compositions [B.Jaffe *et al.*, 1955] 1-10

Table 1.2 Material properties of candidate piezoelectric materials for FBAR applications [S. V. Kirshnawary *et al,* 1990]. 1-12

Table 1.3 Comparison of material properties of ZnO, AlN and PZT thin films [F. Xu *et al.*, 2002]. 1-12

Table 1.4 Typical electrical properties of the resultant $Pb(Zr_{53}Ti_{47})O_3$ films on the different substrates [H. Suzuki *et al.*, 1999]. 1-16

Table 1.5 Properties of a Selected List of Materials [N. Maluf, chapter 1, 2000]. 1-22

Table 2.1 The capacitance, relative permittivity ε_r and tan δ of the PZT thin films (800 nm) with different Nb dopant contents. 2-14

Table 3.1 Material parameters of PZT and Nb-doped PZT bulk ceramics [B. Jaffe et al., 1971]. 3-26

Table 3.2 Calculated effective piezoelectric coefficients d_{33}' and $e_{31,f}$ of PZT and Nb-doped PZT bulk ceramics (in the form of thin film). 3-27

Table 4.1 The operating condition for etching silicon nitride Si_3N_4 using an ICP etcher. 4-6

Table 4.2 The conditions for the deposition of STO and Au/Cr. 4-7

Table 4.3 Etchants for removing Si, Au and Cr layers. 4-7

Table 5.1 The variables of the silicon (100) oriented [N. Setter, chapter 13, 2002]. 5-5

Chapter One
Introduction

1.1 General background

The direct piezoelectric effect was discovered by Piere Curie and Jacques Curie in 1880. When a mechanical stress is applied on certain materials, electric charges are induced on their surface. Those materials also show the converse phenomenon, i.e. a strain is induced when an applied electric field is applied on the materials. This is called the converse piezoelectric effect. A number of materials, including single crystal (quartz, lithium niobate $LiNbO_3$ and lithium tantalate $LiTaO_3$), ceramics (barium titanate $BaTiO_3$ and lead zirconate titanate $Pb(Ti,Zr)O_3$) and polymers (polyvinylidene fluoride PVDF) were found to exhibit piezoelectric effect. The piezoelectric materials have been extensively utilized in various applications such as transducers, actuators, surface acoustic wave devices, frequency control, etc.

For the direct piezoelectric effect, the ratio of the induced electric displacement D_i to the stress X_n applied to a piezoelectric material under isothermal environment is defined as piezoelectric coefficient d_{in}^{E} [Damjanovic, D. 1998]:

$$d_{in}^{E} = \left.\frac{D_i}{X_n}\right|_E \qquad (1.1)$$

where i = 1, 2, 3 and n = 1, 2, ..., 6. On another hand, the ratio of the induced

strain x_n to the applied electric field E_i under isothermal environment for the converse piezoelectric effect is also defined as piezoelectric coefficient d_{ni}^X [Damjanovic, D. 1998]:

$$d_{ni}^X = \left.\frac{x_n}{E_i}\right|_X \tag{1.2}$$

where $i = 1, 2, 3$ and $n = 1, 2, \ldots, 6$. The piezoelectric coefficients for the direct and converse piezoelectric effects are thermodynamically identical [Ikeda, T., 1990; Damjanovic, D., 1998] i.e.

$$d_{in}^E = d_{ni}^X \tag{1.3}$$

Hence, d_{in} is generally used to denote the piezoelectric coefficients for both direct and converse piezoelectric effects. Practically, the piezoelectric samples are polarized along their thickness direction which is denoted as $\hat{3}$. The longitudinal piezoelectric coefficient d_{33} is then a measure of the electric displacement induced along $\hat{3}$ direction by the application of an external stress along the same direction (direct effect), or is a measure of the strain induced along $\hat{3}$ direction by the application of an electric field along the same direction (converse effect). Similarly, the transverse piezoelectric coefficient d_{31} is a measure of the electric displacement induced along $\hat{3}$ direction by the application of an external stress along $\hat{1}$ direction, or is a measure of the strain induced along $\hat{1}$ direction by the application of an electric field along $\hat{3}$ direction. For the sensor applications, transverse piezoelectric (charge) coefficient, e_{31}, which is defined as the ratio of the electric displacement induced along $\hat{3}$ direction by the application of an external

strain along $\hat{1}$ direction, becomes more practically useful.

Barium titanate $BaTiO_3$ and lead zirconate titanate $Pb(Ti,Zr)O_3$ are the most widely used piezoelectric ceramics. They can be categorized into the perovskite family. The perovskite structure, expressed in ABO_3, has a large cation (A) located at the corners, a small cation (B) in the body centre, and oxygen in the centre of the faces (Figure 1.1) [Damjanovic, D. 1998]. A structural phase transition of these materials occurs at a transition temperature called Curie point, T_C [Lines, M. E. *et al.*, 1979]. During the transition, the material changes from a high-temperature paraelectric (non-polar) phase to a low-temperature ferroelectric phase, which exhibits spontaneous polarization under influence of electric field. These materials have cubic structure in paraelectric phase and tetragonal structure in ferroelectric phase (Figure 1.1). However, not all the ceramics with the perovskite structure are ferroelectric, for example, lead hafnate ($PbHfO_3$) and lead zirconate ($PbZrO_3$) are anti-ferroelectric.

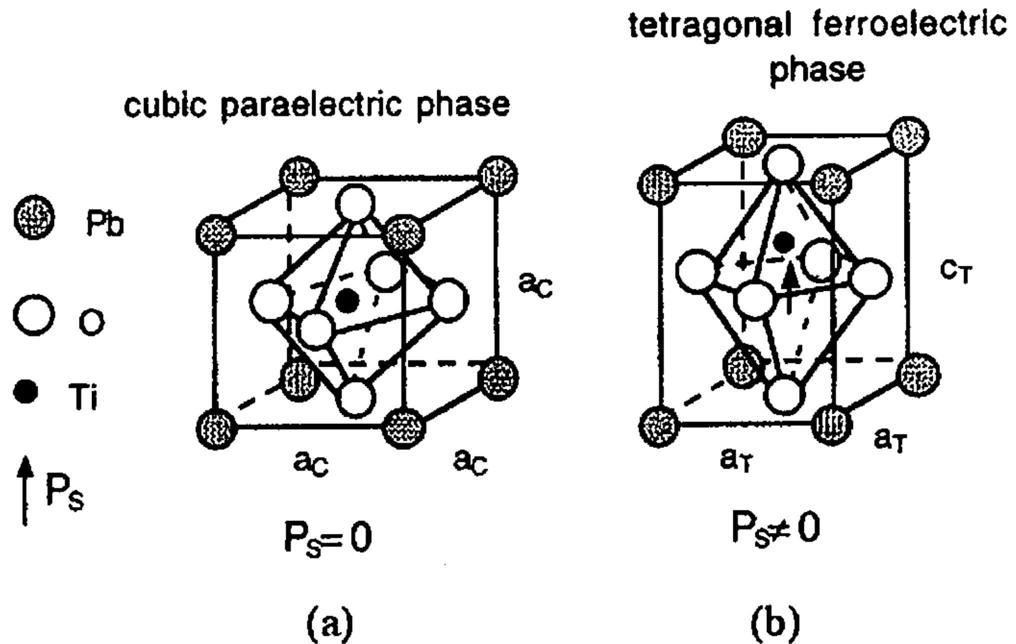

Figure 1.1 The perovskite structure ABO_3, showed a cubic structure in paraelectric phase (a) and a tetragonal structure in ferroelectric phase (b) [Damjanovic, D. 1998].

1.2 Piezoelectric ceramics

The first devices made of barium titanate ceramics are ultrasonic transducers for fish-finders manufactured in Japan [Tanaka, T. 1982]. Nowadays, the piezoelectric ceramics have been widely used in a number of applications such as ultrasonic transducers, accelerometer, vibration sensors and filters [Fukumoto, A.,1982; Tanaka, T. 1982]. Two important piezoelectric ceramics, barium titanium and lead zirconate titanate, are briefly introduced in this section.

1.2.1 Barium titanate $BaTiO_3$

Roberts discovered that the $BaTiO_3$ ceramics are piezoelectric under a high dc field and performed remanent polarization [Roberts, S. 1947]. There is no spontaneous polarization in the high-temperature paraelectric phase of the ceramics. Below the Curie point (~130°C), spontaneous polarization occurs and the crystal structure becomes slightly elongated, that is, tetragonal. The ceramics exhibit the piezoelectric effect in the ferroelectric phase. They are non-piezoelectric and exhibit the electrostrictive effect in the paraelectric phase.

1.2.2 Lead zirconate titanate $Pb(Zr,Ti)O_3$

Piezoelectricity in ceramics of the perovskite family has been extensively studied recently. Peculiar properties in $Pb(Zr,Ti)O_3$ solid solution received much attention in Japan [Sawaguchi, E. 1953]. In 1954, excellent piezoelectric performance was found in a $Pb(Zr,Ti)O_3$ ceramic with a Zr/Ti mole ratio of about 53/47 [Jaffe, B. *et al.*, 1954]. This discovery marked a turning point in the history of ceramics.

$Pb(Zr_x,Ti_{1-x})O_3$ is a solid solution of ferroelectric lead titanate ($PbTiO_3$) and antiferroelectric lead zirconate ($PbZrO_3$), as shown in Figure 1.2. $Pb(Zr,Ti)O_3$ is a member of the perovskite family with Pb located at A-site and Zr and Ti randomly distributed over the B site of the perovskite structure ABO_3 (Figure 1.1). At high temperatures (~ 500°C), $Pb(Zr_x,Ti_{1-x})O_3$ (for all x) has a cubic structure and is in

paraelectric phase. As temperature decreases, the crystallite structure of the solid solution changes, and the resulting crystalline symmetric is dependent on its Zr content (i.e. x value). Lead titanate (i.e. x=0) has a tetragonal structure. With increasing the Zr content, i.e. x increases, the tetragonal distortion decreases. At x > 0.52, the crystallite structure changes from tetragonal to rhombohedral. The boundary separating the tetragonal and rhombohedral phases is called the morphotropic phase boundary which is near the Zr/Ti ratio of 52/48 at room temperature. The solid solution at the phase boundary is considered to have the tetragonal and rhombohedral phases coexisting together (Figure 1.2). C, T, R and O denote the cubic, tetragonal, rhombohedral and orthorhombic phases, respectively, while the subscripts A and F denote the antiferroelectric and ferroelectric phases, respectively

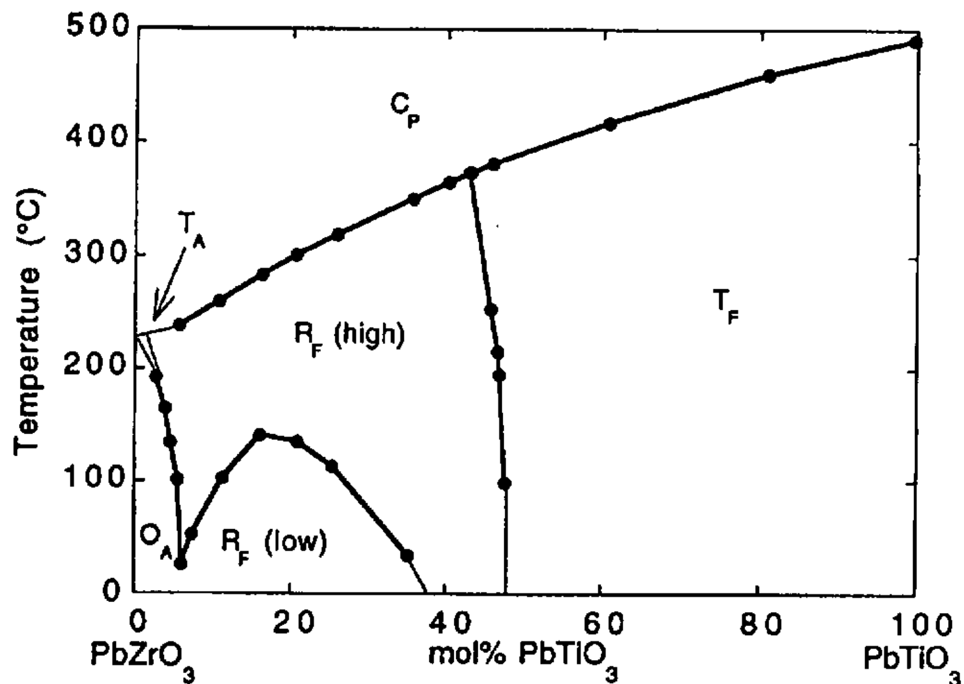

Figure 1.2 Phase diagram of $Pb(Zr_{1-x}Ti_x)O_3$ solid solution showing the morphotropic phase boundary in the middle of the diagram which separates the tetragonal and rhombohedral ferroelectric phases. [Jaffe, B. and Cook, 1971, p.136].

It has been shown that PZT ceramics with compositions near the morphotropic phase boundary have outstanding properties, such as the piezoelectric coefficients, remanent polarization, electromechanical coupling factor and dielectric constant (Figures 1.3-1.5 and Table 1.1).

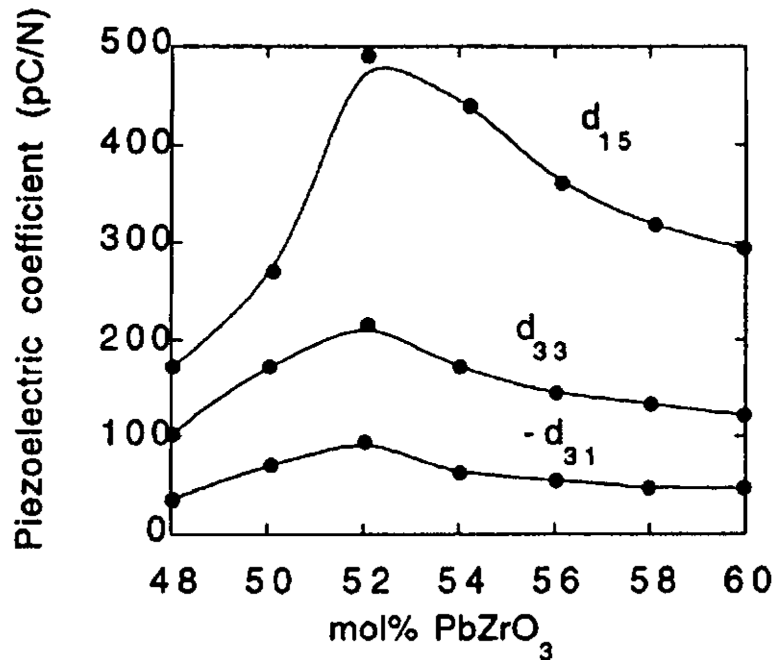

Figure 1.3 Variations of the piezoelectric coefficient d_{ij} with composition of PZT near the morphotropic phase boundary [Jaffe, B. and Cook, 1971, p.143].

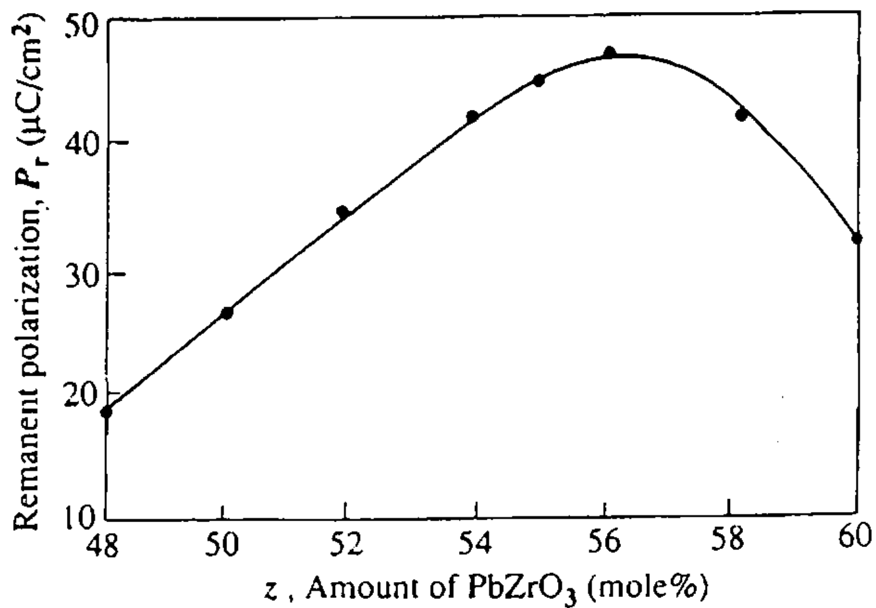

Figure 1.4 Variation of the remanent polarization P_r with composition of PZT near the morphotropic phase boundary [Jaffe, B. and Cook, 1971, p.147].

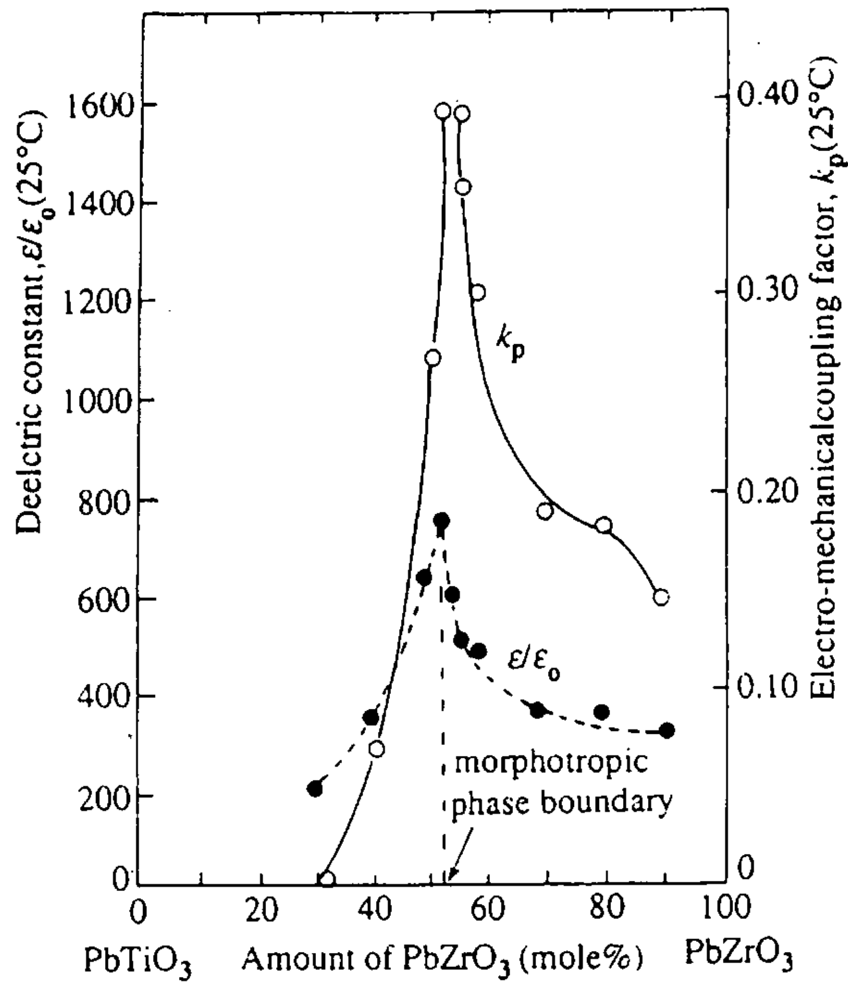

Figure 1.5 Variations of the dielectric constant $\varepsilon/\varepsilon_o$ and electromechanical coupling factor k_p with composition of PZT at room temperature [Jaffe, B. *et al.*, 1954].

Table 1.1 The dielectric constant, dissipation factor DF, radial coupling coefficient k_r and transverse piezoelectric coefficient d_{31} of ceramic with different batch compositions [Jaffe, B. *et al.*, 1955].

Batch composition					
$PbZrO_3$	$PbTiO_3$	@ 1 kHz at 25°C			
mole %	*mole %*	Dielectric constant	DF (%)	k_r	d_{31}
30	70	221	5.5		
40	60	338	1.4		
50	50	641	1.40		
52.5	47.5	782	0.36	0.38	67
55	45	606	0.64	0.36	56
57.5	42.5	533	0.74		
60	40	524	1.6		
70	30	388	2.3		
80	20	375	2.0		
90	10	322	2.0		

Recently, a ferroelectric monoclinic phase in the $Pb(Zr_{1-x}Ti_x)O_3$ ceramic system has been discovered near the morphotropic phase boundary (Figure 1.6) [Noheda, B. *et al.*, 1999]. It has been shown that the monoclinic distortion is the origin of the unusually high piezoelectric response of PZT [Guo, R. *et al.*, 2000].

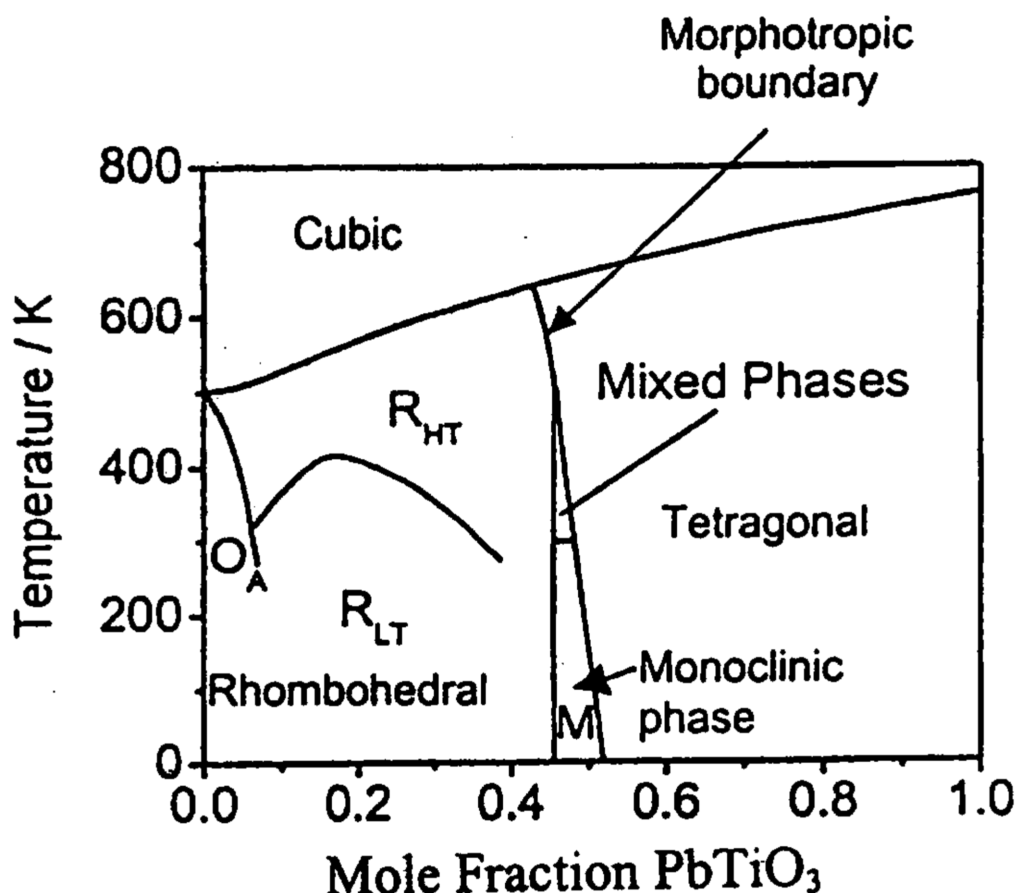

Figure 1.6 The phase diagram of PZT ceramics [Setter, N. chapter 1, 2002].

1.3 Piezoelectric thin films

The trend in miniaturization of electronic components and devices has led to the rapid development of piezoelectric thin films devices. Zinc oxide (ZnO), aluminum nitride (AlN) and PZT are the essential materials for piezoelectric thin film devices. Table 1.2 compares their material properties. Owing to their high acoustic velocity, ZnO and AlN, in particular, have been widely explored for the thin film bulk acoustic resonator (FBAR) applications [Dubois, M. A. *et al.*, 1999; Su, Q. X. *et al.*, 2001]. On the other hand, since PZT has large longitudinal and

transverse piezoelectric coefficients (Table 1.3), it is very suitable for the fabrication of MEMS devices which are functioning by the vibration of a membrane structure [Muralt, P. *et al.*, 2001].

Table 1.2 Material properties of candidate piezoelectric materials for FBAR applications [Kirshnawary, S. V. *et al.*, 1990].

Materials	AlN	ZnO	PZT
Acoustic velocity (m/s)	10400	6340	4500
Electro-mechanical coupling coefficient	2.89%	7.84%	20.25%
Dielectric constant	8.5	8.8	350

Table 1.3 Comparison of material properties of ZnO, AlN and PZT thin films [Xu, F. *et al.*, 2002].

	ε_{33}	$e_{31,f}$ (C/m^2)	d_{33} (pm/V)
(001) ZnO	8 to12	-0.4 to -0.8	10 to 12
(001) AlN	10.4	-0.9 to -1.0	3.4 to 3.9
Random PZT 52/48	900 to 1300	-6 to -7	~100 to 150

1.3.1 Techniques for deposition of thin films

In order to prepare thin films, a number of deposition techniques have been developed, such as evaporation, magnetron sputtering, sol-gel process, etc.

Evaporation is one of the oldest techniques used for depositing thin films [Maissel, L. I. *et al.*, chapter 1, 1970]. It involves the local heating of a target material to a sufficiently high temperature in order to generate a vapor. This vapor is transported from the target to the substrate and condensed on the substrate surface to form a solid film. Nearly any materials (e.g. Al, Au, Cr, Pt, etc) can be evaporated provided it has a vapor pressure at 0.1-1 Pa. A filament of tungsten is used to heat up the target material in the process.

Evaporation is a directional deposition process where the material vapor is transported to the substrate at a specific angle. It may form poor step coverage. It is generally an undesirable effect if continuity of thin film is desired.

In sputter deposition, a target made of a material to be deposited is physically bombarded by a flux of inert ions (e.g. argon) in a vacuum chamber. Material particles from the target are ejected and deposited on the substrate. Sputtering process can be divided into dc- and rf-sputtering processes. In dc-sputtering, the inert ions are accelerated by a dc field between the target and the substrate [Chapman, B. chapter 4, 1980]. However, it cannot work for insulating materials because the positive ions will immediately build-up on the front side of the insulator.

This then prevents any further ion bombardment. In contrast, insulating materials can also be used in rf-sputtering [Chapman, B. chapter 5, 1980]. If an external magnetic field is applied in the sputtering process, it is called magnetron sputtering [Smith, D. L. chapter 9, 1995]. More ions are accelerated by the magnetic field to bombard the target surface. Thus the resulting deposition rate increases.

The directional randomness of sputtering process results in good uniformity of thin film over a geometrical step. In addition, rotation of the substrates can be used to even out the thickness of the coating. The disadvantages of sputtering system are the high equipment cost, long processing time for pumping down the sputtering environment, etc.

Sol-gel process is the name given to any one of a number of processes involving a solution or sol that undergoes a sol-gel transition [Klein, L. C. 1985]. Sol is a stable suspension of colloidal solid particles in a liquid. A gel contains a continuous solid skeleton enclosing a continuous liquid phase. A sol can be transformed into a polymeric gel when it passes through a certain condition which is called a gel point [Seyferth, D. *et al.*, 1984]. This needs a homogenous dispersion present in the initial sol rigidifies. Practically, the sol changes abruptly from a viscous liquid state to a solid state called the gel at this point.

Sol-gel process is now well accepted as a technology for forming thin films and coatings. A solution containing the desired oxide or non-oxide precursors is first prepared. The solution is then applied on a substrate by spinning and dipping.

For research purpose, the spin coating technique is more preferable than the others because it can produce films of larger area with uniform thickness. A film of certain thickness can be obtained by repeating the spinning and heating process a number of times. The advantage of the sol-gel process for preparation of films is that it offers better stoichiometry control of material composition and chemical homogeneity. It does not require any expensive and sophisticated equipment.

1.3.2 Seeding layer

For the sol-gel process, the growth of film is nucleation controlled, i.e., heterogeneous nucleation is preferred over homogenous nucleation [Chen, K. C. *et al.*, 1990]. Sol-gel process allows obtaining a columnar film microstructure nucleated at the bottom electrode of substrate. Nucleation controlled growth also permits choosing the texture of the film by using suitable electrodes [Aoki, K. *et al.*, 1995; Muralt, P. *et al.*, 1998] with seeding layer to reduce the deposition temperature [Kwok, C. K. *et al.*, 1993]. With a lead titanate (PT) seeding layer, PZT films can be prepared at a lower temperature on certain substrates and still exhibits good enough dielectric and ferroelectric properties for industrial use (Table 1.4) [Suzuki, H. *et al.*, 1999].

The microstructure of the PZT thin film is composed of homogenous submicron grains and can be controlled by the introduction of a thin seeding layer $PbTiO_3$ with lower crystallization temperature [Ishikawa, K. *et al.*, 1998]. The dielectric properties of ferroelectric materials could be controlled by the grain size.

Sol-gel derived PZT films with grain size of 1 μm can be formed on a seeding layer (Figure 1.7) [Seifert, A. *et al.*, 1999]. The first ones were grown on Pt (111) layers with TiO_2 or $PbTiO_3$ seeding layers, the latter ones on sapphire. It was shown that the PZT films with different compositions spun on a seeding layer could form a good quality film with average grain size.

Table 1.4 Typical electrical properties of the resultant $Pb(Zr_{53}Ti_{47})O_3$ films on the different substrates

Electrode	Annealing Temperature (°C)	Coercive field (kVcm^{-1})	Remanent polarization (μC/cm^{-1})	Relative permittivity	Dissipation factor (tan δ)
Pt	500	91	43	480	0.069
Pt	550	115	41	700	0.051
SnO_2	500	125	29	410	0.049
SnO_2	550	145	39	600	0.066
ITO	500	142	21	300	0.073
ITO	550	144	33	350	0.095

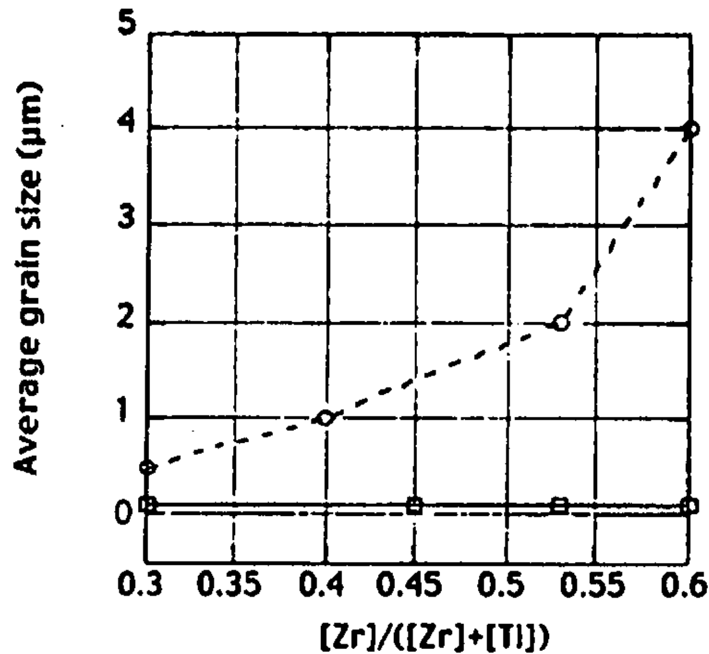

Figure. 1.7 Average grain size of seeded (continuous line) and unseeded (dotted line) sol-gel deposited PZT thin films [Seifert, A. *et al.*, 1999].

1.3.3 Doping effect

Small amount of dopants can modify the dielectric and electro-mechanical properties of ceramics drastically.

Acceptor dopant is a dopant with a lower valence than the substituted cations, e.g. Fe^{3+} and Na^{+1}, they will replace Ti^{4+}/Zr^{4+} and $Pb^{2+}$of a PZT ceramics respectively. Since acceptor dopant has a lower valance, oxygen deficiency will be formed in the doped ceramics. Oxygen deficiency can move in the oxygen sublattice, hence they form reorientable dipoles with the dopant cations. These dipoles align in the same direction of the polarization vector in the domain, and

create an internal field that stabilizes the domain configuration and reduces the mobility of domain walls. The PZT becomes more stable and less responsive when an external signal (electric field or stress) is applied. The piezoelectric constants, dielectric constant and loss become smaller since the domain wall mobility is reduced. Conversely, the coercive field increases and the mechanical quality factor becomes larger. The acceptor doped PZT ceramics are hence called 'hard' PZTs, and are particularly suitable for ultrasonic motor applications.

Donor dopant is a dopant with a higher valence than the substituted cations, e.g. Nb^{5+} for Ti^{4+}/Zr^{4+} or La^{3+} for Pb^{2+}. The excess valences are compensated by lead vacancies, which enhances the mobility of domain walls. Due to the close surroundings of oxygen, the Pb^{2+} ion cannot move to an A-site vacancy. Thus, movable dipoles cannot be generated effectively. This results in an opposite effect of the acceptor doping, that is the piezoelectric coefficients, dielectric constant and loss increase while the elastic stiffness, coercive field, and mechanical quality factor decreased. After the donor doping, the ceramics became electrically and mechanically 'softer'. They are hence called 'soft' PZTs, and can be used in actuator and positioner applications.

Hagimura and Uchino studied the effect of impurity doping on field-induced strains of $(Pb_{0.73}Ba_{0.27})(Zr_{0.75}Ti_{0.25})O_3$ (soft piezoelectric). Figure 1.8 (a)shows the definitions of the maximum strain x_{max}, and the degree of hysteresis $\Delta x/x_{max}$ (%). The degree of hysteresis is calculated from the strain deviation between the rise and fall of the field Δx at half of the maximum electric field (1 kV/mm) divided by the

maximum strain x_{max} at 1 kV/mm. Figure 1.8 (b) shows the dopant effect on the strain, in which the doping concentration is fixed at 2 at.%. As shown in Figure 1.8 (b), the materials incorporating donor-type ions on the B site with a higher valence (e.g. Ta^{5+}, Nb^{5+}, W^{6+}) exhibit excellent performance as positioning actuators, namely, enhancement or maintenance of the strain magnitude and reduction of the hysteresis.

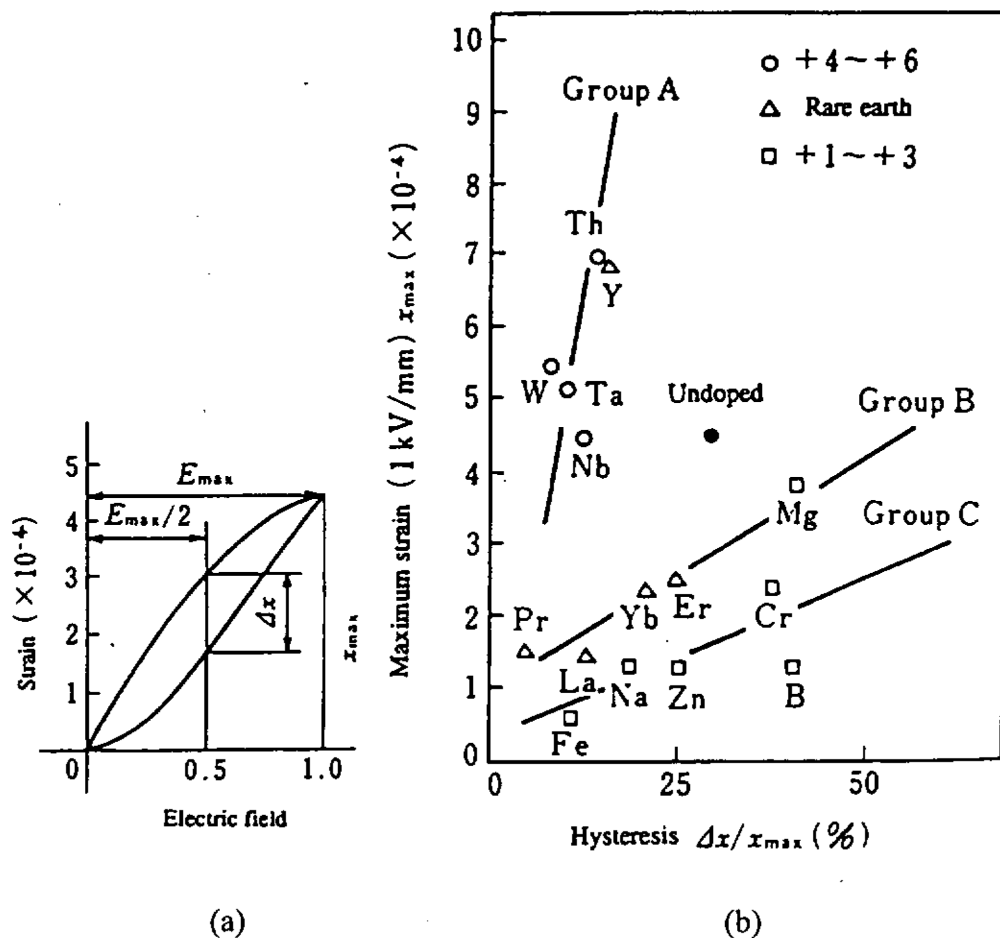

(a) (b)

Figure 1.8 Dopant effect on the field-induced strain. Maximum strain and hysteresis in $(Pb_{0.73}Ba_{0.27})(Zr_{0.75}Ti_{0.25})O_3$-based ceramics. (a) Definition of the maximum strain and the degree of hysteresis, and (b) dopant effect on actuator parameter [Uchino, K., chapter 3, p.62, 2000].

1.4 Microelectromechanical systems

The field of microelectromechanical systems (MEMS) was originated by Richard P. Feynman in 1959, when he made the observation of *There's Plenty of Room at the Bottom* [Feynman, R. P. 1959]. The notion of MEMS emphasized that mechanical elements are added to the microelectronics. He began exploring the miniaturization of information storage, computers, atomic-level manipulation, and machinery [Feynman, R. P. 1959; Feynman, R. P. 1983; Senturia, S. D. 1994]. The actual field of MEMS has the much broader content today such as optical, thermal, magnetic, and fluidic (chemical and biological) interactions and phenomena [Senturia, S. D. 2001].

In the mainstream of MEMS technology, silicon is commonly used as supporting and structural materials for the devices. It can be economically manufactured the electronic integration circuits in industry. Using the impurity doping, the electrical conductivity of silicon can be modified precisely. Mechanically, silicon is an elastic material. It becomes evident that silicon is a suitable material platform to integrate the electronics, mechanical and thermal products (Table 1.5) [Maluf, N. chapter 1, 2000].

Silicon as an element exists in any of three forms: crystalline, polycrystalline or amorphous. Polycrystalline and amorphous silicon are usually deposited as films with typical thickness below 5 μm. Crystalline silicon substrate are available as circular wafer with either 100 mm (4 inch) or 150 mm (6 inch) in diameter for

fabricating devices. Standard 100 mm and 150 mm wafers are nominally 525 μm thick and 650 μm thick respectively. Double-side polished wafers used in micromachining are approximately 100 μm thinner than standard substrates.

Table 1.5 Properties of a Selected List of Materials.

Property	Si	SiO_2	Si_3N_4	Quartz	SiC	AlN	92% Al_2O_3
Relative permittivity (ε_0)	11.8	3.8	4	3.75	9.7	8.5	9
Dielectric strength (V/cm $\times 10^6$)	3	5–10	5–10	25–40	4	13	11.6
Electron mobility ($cm^2/V \cdot s$)	1500	—	—	—	1000	—	—
Hole mobility ($cm^2/V \cdot s$)	400	—	—	—	40	—	—
Young's modulus (GPa)	160	73	323	107	450	340	275
Yield strength (GPa)	7	8.4	14	9	21	16	15.4
Poisson's ratio	0.22	0.17	0.25	0.16	0.14	0.31	0.31
Density (g/cm^3)	2.4	2.3	3.1	2.65	3.2	3.26	3.62
Coefficient of thermal expansion ($10^{-6}/°C$)	2.6	0.55	2.8	0.55	4.2	4.0	6.57
Thermal conductivity at 300K ($W/cm \cdot K$)	1.57	0.014	0.19	0.0138	5	1.60	0.36
Specific heat ($J/g \cdot K$)	0.7	1.0	0.7	0.787	0.8	0.71	0.8
Melting temperature (°C)	1415	1700	1800	1610	2830	2470	1800

The materials deposited on silicon substrate play an important role in MEMS technology. Piezoelectric materials are an important family of functional materials in MEMS technology. In fact, they provide the electro-mechanical coupling directly in the purpose of MEMS. The piezoelectric ceramics and films of PZT have been used as functional materials in numerous sensor, actuator and transducer

applications [Uchino, K. chapter 7, 2000].

Micromachining is a method for fabricating MEMS [Maluf, N. chapter 3, 2000]. From a simplistic perspective, it is similar to conventional machining that the objective is to precisely define arbitrary features from a material. Micromachining is a parallel process in which various materials are fabricated simultaneously on the same wafer. The minimum feature dimension of it is in the order of one micrometer, about a factor of 25 times smaller than the product by conventional machining. The basic process flow in micromachining includes material deposition, patterning and etching.

The thin film deposition techniques are mentioned in section 1.3.1. Sol gel techniques appear to be the most suitable ones for the MEMS application. Investments are relatively low and good uniformities can be achieved on standard 150 mm wafers. After depositing the films on silicon substrates, the next step is patterning. Lithography plays a significant role in the fabrication of accurate and precise patterns. Optical lithography is a dominant technique to transform complex circuit diagrams into patterns which are defined on the wafer in MEMS fabrication. Wet and dry etching are essential process bases to selectively remove materials.

1.4.1 Lithography

Lithography comes from two Greek words, '*lithos*' which means atone and

'graphein' which means write. That means literally *'writing a pattern in stone'* [El-Karch, 1995]. In microelectronics, lithography is a process in which a pattern is delineated in a layer of material sensitive to photons, electrons or ions. Simply to speak, the principle is similar to that of a photocamera in which an object is imaged on a photo-sensitive emulsion film. After development, the exposed regions of the film are left as metallic silver, while the unexposed regions are removed, resulting in a printed image of the object. The 'final product' of a photo-camera is the printed image. In microelectronics, it is an intermediate pattern which defines regions where material is deposited or removed. Lithography transforms circuit diagrams into patterns which are defined on the wafer in a succession of exposure and processing steps to form a number of superimposed layers of insulator, conductor and semi-conductor. There are four major lithography technologies for producing submicron feature sizes: optical, electron-beam, X-ray, and ion-beam. Optical lithography has remained the dominant technology [McCoy, J. H. *et al.*, 1989]. An optical lithography tool consists of an ultraviolet (UV) light source, a photomask, photoresist and an optical system.

1.4.2 Light source

The ultraviolet light sources from high-pressure arc lamps are most commonly used for optical lithography. The emitted light spectrum can be distinguished to three regions: deep ultraviolet (DUV) in 100-300 nm range, mid-UV in the 300-360 nm range, and near-UV in the 360-450 nm range.

A typical arc source is shown schematically in Figure 1.9. The emitted light (dotted torroid shapes) is reflected by parabolic mirrors into a lens assembly. Then the parallel beam is formed and projected on the mask. The arc source is filled with mercury or a mercury-xenon mixture at a typical pressure of 30-35 atm. For a high-pressure Hg lamp, the dominant emitted wavelengths of significant intensity are 436 nm (G-line), 405nm (H-line) and 365 nm (I-line) (Figure 1.10). Only the 436-nm and shorter wavelengths are considered for optical lithography. The full emitted spectrum can be used to expose the photoresist for fabricating the minimum features sizes larger than about 2 μm.

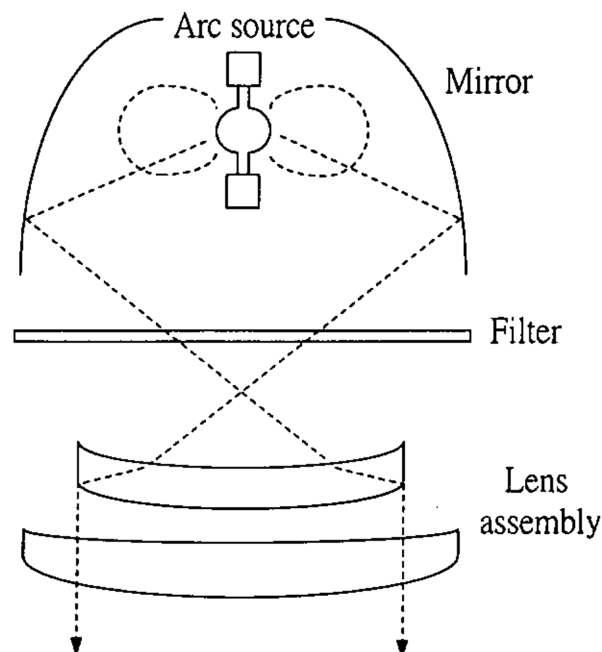

Figure 1.9 Typical arc soured and surrounding optics.

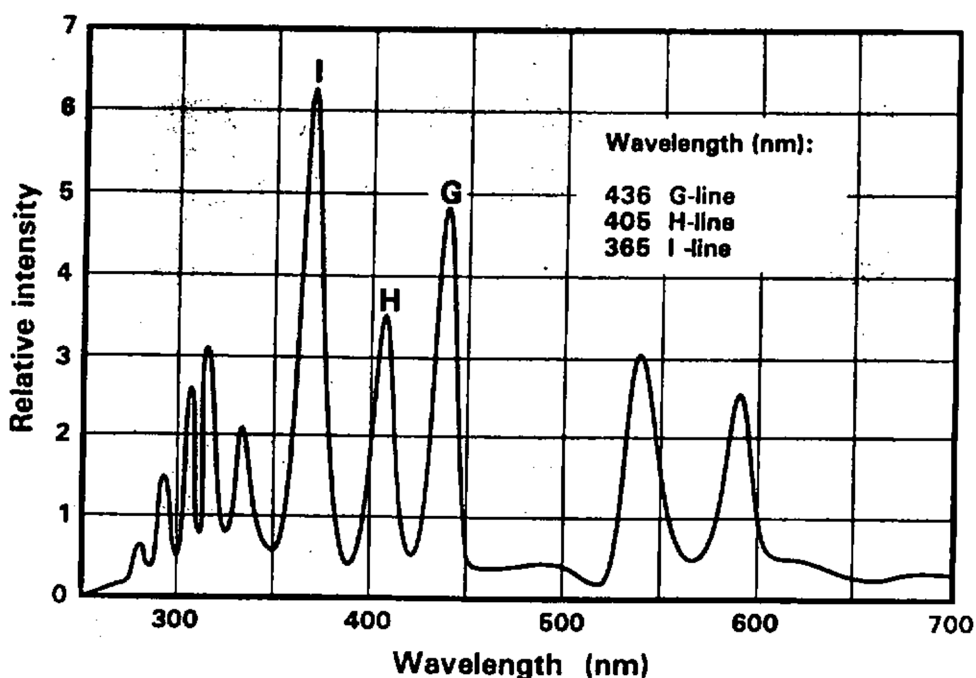

Figure 1.10 Output spectrum of a high pressure mercury arc source, high-lighting and high-intensity lines used in photolithography [El-Kareh, 1995].

1.4.3 Photomask

A mask for optical lithography consists of a transparent plate called blank, covered with a patterned film of opaque material. This blank usually is made of soda lime, borosilicate glass, or fused quartz. A thin (< 100 nm) film of chrome is a typically choice of the opaque material. An anti-reflective coating (ARC), such as chrome oxide, is covered at the mask surface to suppress interferences.

There are two kinds of masks can be used in lithography. The first one is clear-field (correct positive), which means that the image is defined as opaque on the mask. Then the image polarity can be reversed during processing. Dark-field

(negative positive) is converse of the clear-field (Figure 1.11). Normally, the dark-field mask is preferred over the clear-field mask because it reduces light scattering effects. Moreover, the probability that particles will fall on an opaque area where it is not imaged is higher.

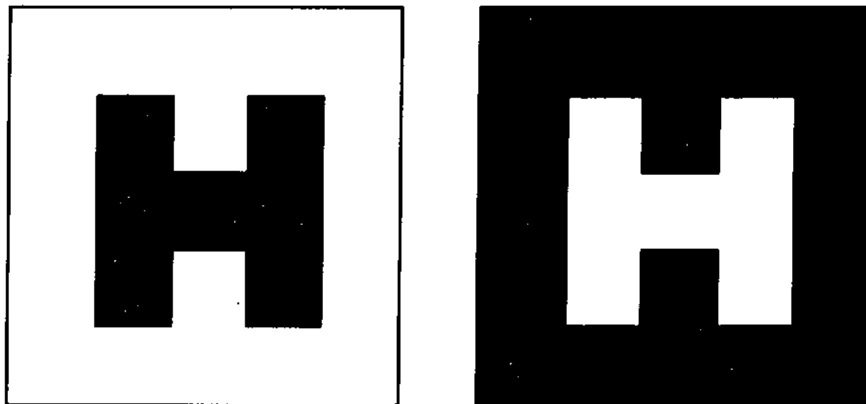

Figure 1.11 Reticle polarity. (a) Clear-field, or correct positive.
(b) Dark field, or correct negative.

1.4.4 Photoresist

Photoresist is a mixture of organic compounds whose solubility changes when exposed to the ultraviolet light. After the exposure to ultraviolet light, the regions in the photoresist become either more soluble or less soluble in a solvent called developer. There are also two different photoresists, positive photoresist and negative photoresist, which have different characteristics. When the exposed region becomes more soluble, a positive image of the mask is defined in photoresist, it is the positive photoresist. The material is a negative photoresist that the irradiated region becomes less soluble in the developer, while the non-irradiated

region is soluble, the negative image of the mask is formed in the photoresist (Figure 1.12).

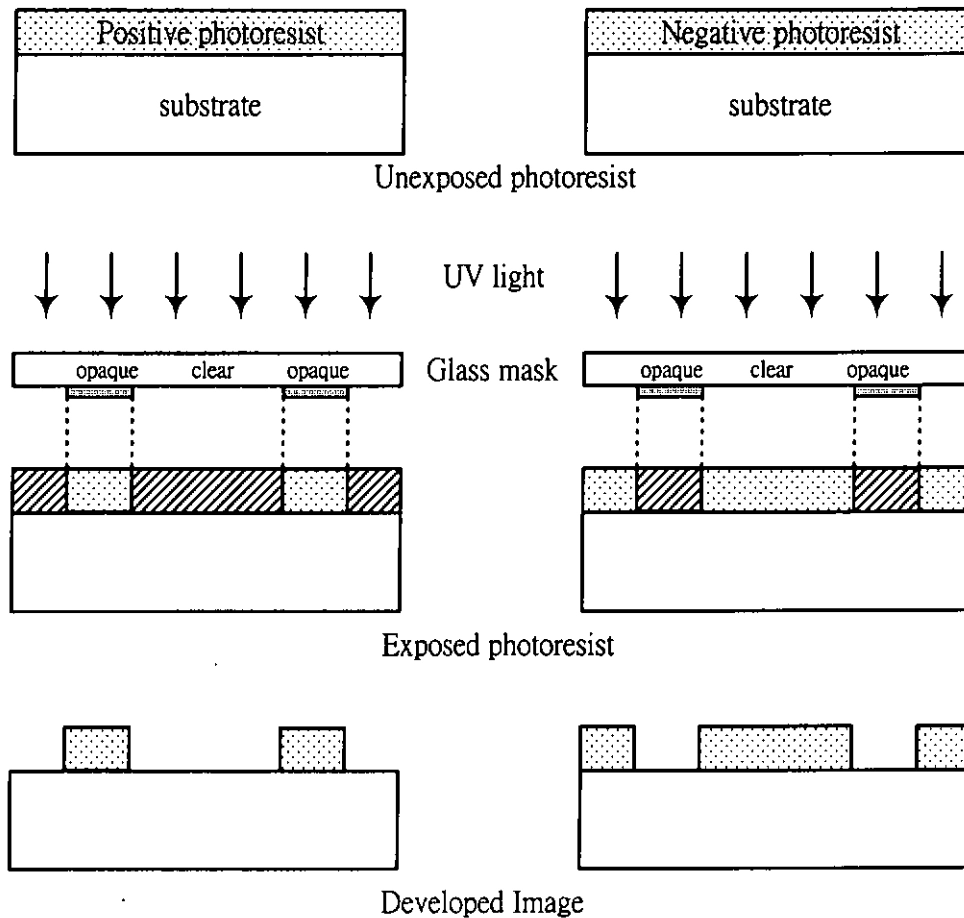

Figure 1.12 Mask projection and lithography illustrating the difference between positive and negative photoresist.

1.4.5 Exposure systems

There are three types of photolithographic exposure techniques: contact, proximity and projection printing (Figure 1.13).

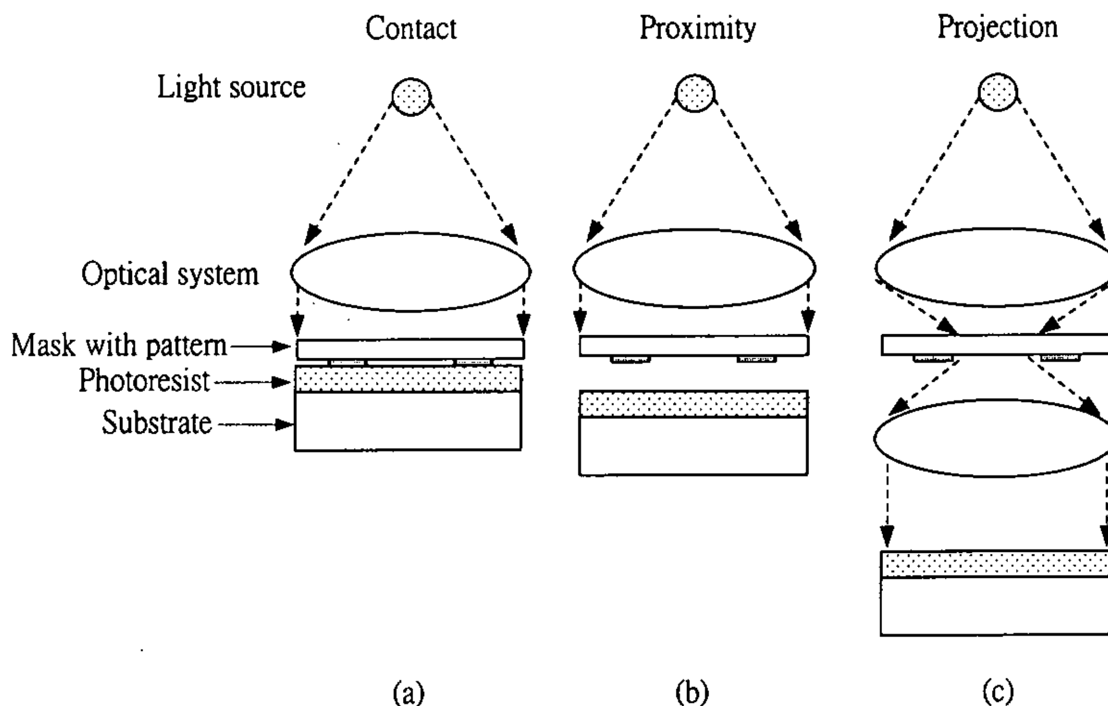

Figure 1.13 Schematic of three optical lithographic techniques.

(a) Contact, (b) Proximity and (c) Projection

Contact and proximity printing are the simplest and inexpensive imaging methods. For both techniques, the mask covers the entire wafer. The mask is aligned to the pattern side facing the photoresist-coated wafer. Then the pattern on the mask must contain the mirror image of the pattern on the photoresist. In the proximity printing, a small gap is formed between the mask and photoresist, which can eliminate the defects caused by direct contact between the surface of sample.

Projection printing is an imaging technique which uses lens assemblies to focus the mask pattern onto the wafer that is separated from the mask by several centimeters. This method can be used in fabricating the pattern which is smaller

than 1 μm. Normally the pattern will not be too small on the mask. If there are particles or dust on it, the exact pattern cannot be transferred on the sample. Therefore, a larger pattern will be generated on the mask first. The lens assembly can reduce the feature size of the pattern. The desired size of the pattern can be fabricated on the sample. The advantage of it is that the mask defects and imperfections are also reduced in size and hence become less severe.

1.4.6 Etching

Etching is the selective removal of materials. Solid surfaces can be etched either by reaction with a liquid – wet etching or gas – dry etching. During the etching process, the etched product has to be removed form the surface, i.e., it has to be either soluble in the liquid, or sufficiently volatile in dry etching. In fabricating MEMS devices, the main objective of etching is to reproduce the image of the mask with a high degree of fidelity. There are two etching processes: subtractive and additive (Figure 1.14).

The first step of the subtractive etching process is to deposit or coat the film on a substrate. Then the desired pattern is transferred on the film by photoresist. The photoresist is a protection layer for the etching process. After the etching process and removal of photoresist, the desired pattern of film is formed.

In the additive process, the photoresist is coated and patterned before the desired film is deposited. After that, the film is deposited on it. When the

photoresist is removed by a solvent, the unwanted film on the photoresist is removed at the same time. This process is also called lift-off process. For the process, the thickness of the deposited film must be thinner than the photoresist.

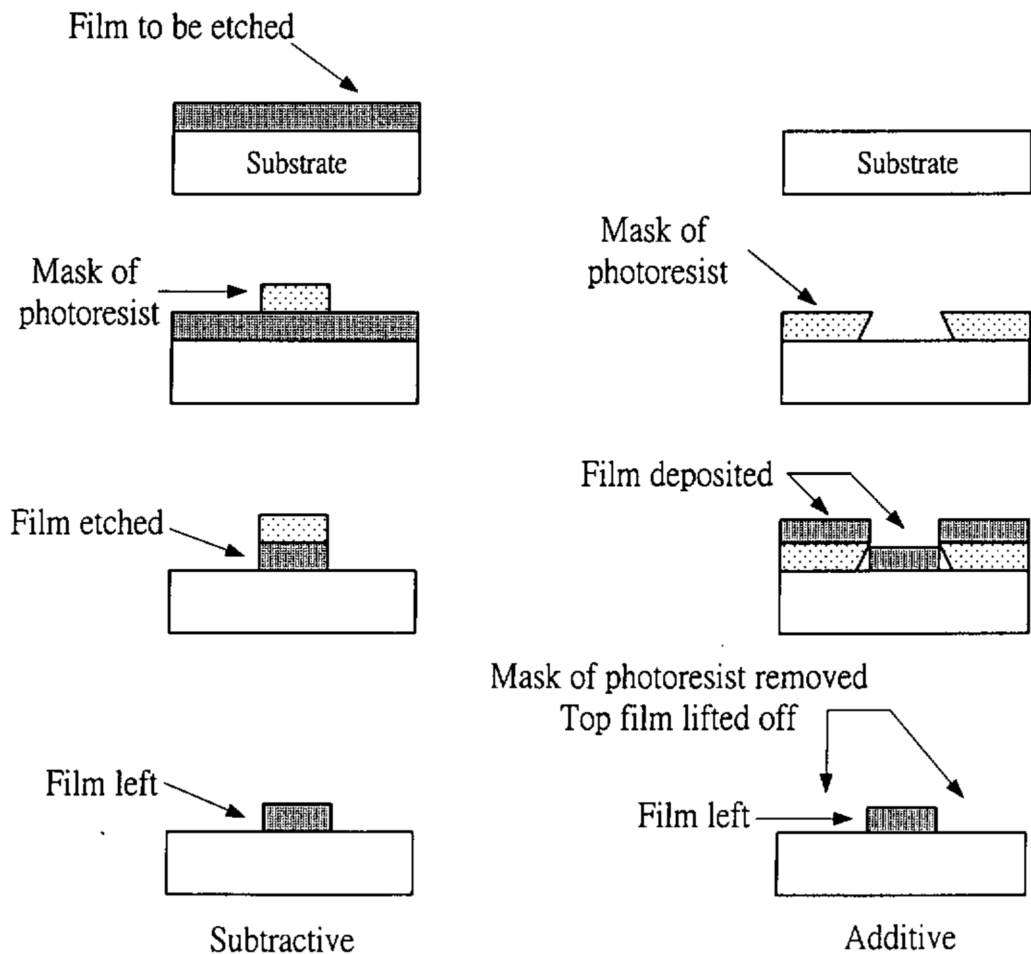

Figure 1.14 Definition of a patterned film by subtractive and additive processes

When the material is etched at the same rate in all directions, it is called isotropic etching. When the etch rate is considerably larger in one direction than another, it is called anisotropic etching.

1.4.6.1 Wet etching

Wet etching is the removal of material by immersing the wafer in an appropriate solution or by spraying the wafer with the chemical etchant.

Isotropic etchants are available for oxide, nitride, aluminium, gold and chromium. The most often used masking materials for high resolution thin film patterning are photoresists [DeForest, W. S. 1975]. Since isotropic etchants attack the material at the same rate in all directions, they remove material horizontally under the etch mask (e.g. photoresist). This is called undercutting (Figure 1.15).

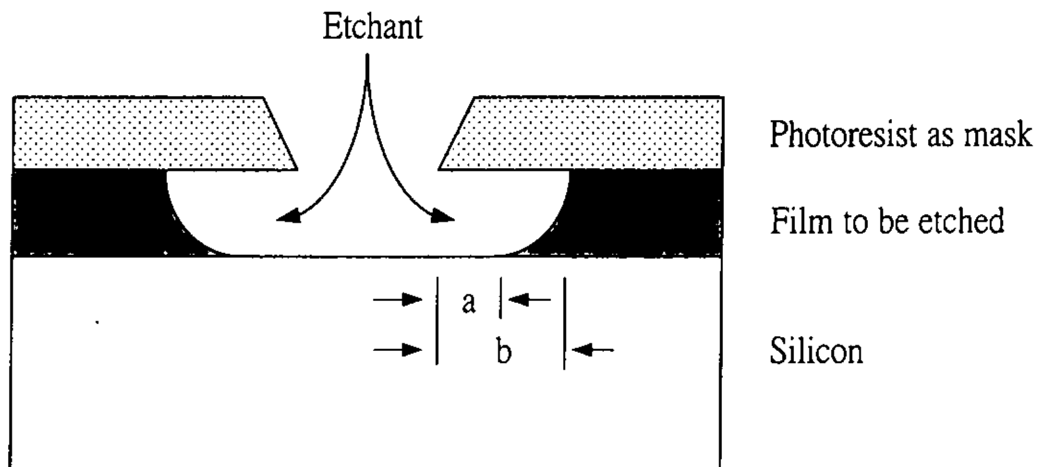

Figure 1.15 Definition of two lateral etch dimensions, illustrated for isotropic etching. a is referred to etch bias and b as undercutting.

Anisotropic etchants are available for etching different crystal planes in silicon at different rates. The most popular anisotropic etchant is a dilute solution of potassium hydroxide (KOH). The simplest structures of a silicon wafers with the

common crystal orientation (100) that are formed by etching with KOH are shown in Figure 1.16. The etching rate of {111} planes is the slowest while that of {100} planes is the fastest. Since (111) planes make an angle of 54.7° with (100) planes, the depth (d) of etching can be determined by the following equation :

$$d = \frac{W}{2}\tan 54.7° = 0.7W \tag{1.5}$$

where W is the width of the window at the silicon surface.

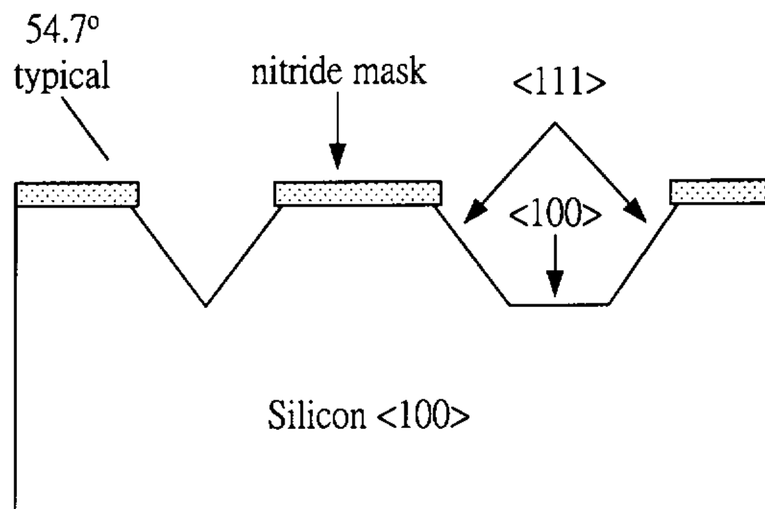

Figure 1.16 V-shaped groove formation in <100> silicon with anisotropic etching

1.4.6.2 Dry etching

In the middle of 1800s, it has been shown that a solid-state surface can be eroded by the interaction with species from a glow discharge [Grove, W. R. 1852]. The application of dry etching in Si-device technology was descried by Irving in

1968 [Irving, S. M. 1968; Irving, S. M. 1971]. Irving introduced a novel method for stripping of photoresist in oxygen plasma. Abe used CF_4 in a barrel reactor to perform the etching of single crystalline Si and films of SiO_2 and Si_3N_4 in 1973 [Abe, H. 1973]. The emerging of plasma techniques for applications in Si technology was quickly realized in the semiconductor companies.

The typical wet etch techniques exhibit a good performance in etching selectivity and allow processing in large batches. If the pattern size is smaller than 1 μm, wet etching process cannot promise the degree of fidelity and control required for the manufacture of MEMS devices. Moreover, dry etching reduces chemical hazard and waste treatment problems, and is the ease of process automation and tool clustering. Since many dry etch processes use a low pressure gas in the form as plasma to the etchants, it has become synonymous with plasma etching. The most common example of plasma-assisted etching is the removal of photoresist by oxygen plasma.

1.5 Scope of work

Ferroelectric films of lead zirconium titanate (PZT) with high piezoelectric constants have attracted considerable attention for MEMS applications, such as micro actuators. This thesis focuses on the fabrication and characterization of niobium (Nb)-doped PZT films, as well as the study of using these PZT films for MEMS devices.

The procedures for preparing Nb-doped PZT films on a $Pt/Ti/SiO_2/Si/Si_3N_4$ substrate by the sol-gel method are described in Chapter 2. In order to lower the annealing temperature and hence to eliminate diffusion at the interface between the PZT film and Pt bottom electrode, a lead titanate (PT) seeding layer is introduced. In the same chapter, characterization of the sol-gel derived films, including crystallite structure, microstructure and dielectric properties are presented.

Longitudinal and transverse piezoelectric coefficients (d_{33} and e_{31}) of the PZT films (both before and after poling) have been measured using a single beam laser interferometer and a newly established method based on the direct piezoelectric effect, respectively. The details of the measurement are described in Chapter 3. The effects of Nb-dopant on the observed d_{33} and e_{31} of values of PZT films have been investigated and the results are reported in Chapter 3.

The fabrication of micromachined membrane using the PZT films is described in Chapter 4. The performance of the silicon-based membranes have evaluated and the results are discussed in Chapter 5.

Chapter Two
Preparation and Characterization of PZT Films

In this chapter, the fabrication of sol-gel derived PZT films on a $Pt/Ti/SiO_2/Si/Si_3N_4$ substrate and the characterizations of the crystallite structure and microstructure of the films are presented. The $Pt/Ti/SiO_2/Si/Si_3N_4$ substrate is fabricated by Hong Kong University of Science and Technology and the layer of low-stress silicon nitrate (Si_3N_4) on the bottom is deliberately added as a protective layer for opening a backside window of a membrane structure, which will be discussed in Chapter 4. However, our preliminary studies showed that diffusion (probably of Pt) at the interface occurred when the film was annealed at a high annealing temperature, e.g. 650°C and 600°C which are normally used to fabricate sol-gel derived PZT films. The problems could not be solved even after the substrate has been annealed at a high temperature (e.g. 600°C) before the deposition of the films. In fact, high processing temperature for lead base materials is also a key concern for contamination in micromachining industry. Therefore, in this project, in order to lower the sintering temperature, a thin lead titanate (PT) seeding layer was introduced between the PZT film and the Pt electrode. In doing this, the diffusion and film-cracking problems have also been solved. The function of the seeding layer is to give a stable platform for growing a thicker film on the substrate at a lower temperature. The PT seeding layer is a good candidate because it provides a nucleation site for PZT crystallization [Ishikawa, K. *et al.*, 1998].

Both the PT seeding layer and PZT film were prepared by the sol-gel method. The PT precursor solution was prepared in our laboratory, while the PZT precursor solution with 10% excess lead was supplied from Mitsubishi Materials Co. Japan. The PZT composition near the morphotropic phase boundary (i.e. Zr/Ti = 53/47) was chosen because of their good piezoelectric properties. It has been experimentally shown that the piezoelectric properties of the PZT ceramics can be improved by the niobium (Nb) dopant [B., Jaffe *et al.,* 1971]. Therefore, in this work, PZT films with 0%, 1% and 2% Nb were prepared. The sol-gel method was used since it is an easy method and the fabrication cost is relatively low. It allows the production of any oxide compositions and new hybrid organic-inorganic composition, and has good control of the stoichiometric system of the film composition and chemical homogeneity.

Before the study of the piezoelectric properties, the quality of the PZT films was first examined. The crystalline structure of the PZT films was studied using an x-ray diffractometer with nickel-filtered CuKα radiation (D8 Discover, Bruker), the microstructure was examined using a scanning electron microscope (Lecia 440), and the dielectric properties were measured using an impedance analyzer (HP 4194A, Hewlett Packard).

2.1 Preparation of lead titanate precursor solution

In preparation of a PT precursor solution, the solvent is an important factor to be considered. There are some requirements of the solvent. Firstly, the boiling

point of the solvent should be above the room temperature and below the boiling temperature of the stock chemicals for preparing the precursor solution, such that the chemicals will not evaporate when removing the solvent from the precursor solution at the last step. Secondly, the solvent should be chemically stable. Thirdly, the solvent should be non-toxic such that no extra precaution is needed to be considered during the high-temperature process.

In this work, lead (II) acetate trihydrate $Pb(CH_3COO)_2 \cdot 3H_2O$ and titanium (IV) n-butoxide $Ti(O(CH_2)_3CH_3)_4$ were chosen for the stock chemicals and 2-methoxyethanol $CH_3OCH_2CH_2OH$ was used as the solvent to form the PT precursor solution. The boiling temperature of the solvent is 124°C which is lower than the boiling temperatures of lead (II) acetate trihydrate and titanium (IV) n-butoxide, which are 280°C, and 310°C respectively. The titanium (IV) n-butoxide can react with water to form precipitates of TiO. Therefore, the PT precursor solution should be prepared in a dry environment.

A PT precursor solution with 10% excess lead was prepared. The procedure for the preparation of the precursor solution is depicted in the flow chart shown in Figure 2.1. At first, certain amount of lead (II) acetate trihydrate was kept in an oven at 135°C for 8 hours for dehydration. The dried lead (II) acetate was then dissolved into 2-methoxyethanol (MOE) under continuous heating and stirring. After all the lead acetate was dissolved, the resulting solution was cooled down to room temperature. Suitable amount of titanium (IV) n-butoxide was added into the solution. Then the solution was heated at a temperature slightly above the

boiling temperature of MOE and was stirred continuously for chemical reaction and evaporation of excess MOE. After the chemical reaction was completed and suitable concentration of the precursor solution was obtained, the precursor solution was cooled down to room temperature and filtered with cotton to remove any impurities and foreign substances in the precursor solution. The concentration of the precursor solution was set to 0.5 M. The resulting precursor solution was then kept in an argon environment in order to prevent reaction with water. To obtain better quality of the film, the precursor solution was kept at least 1 day for stabilization before use.

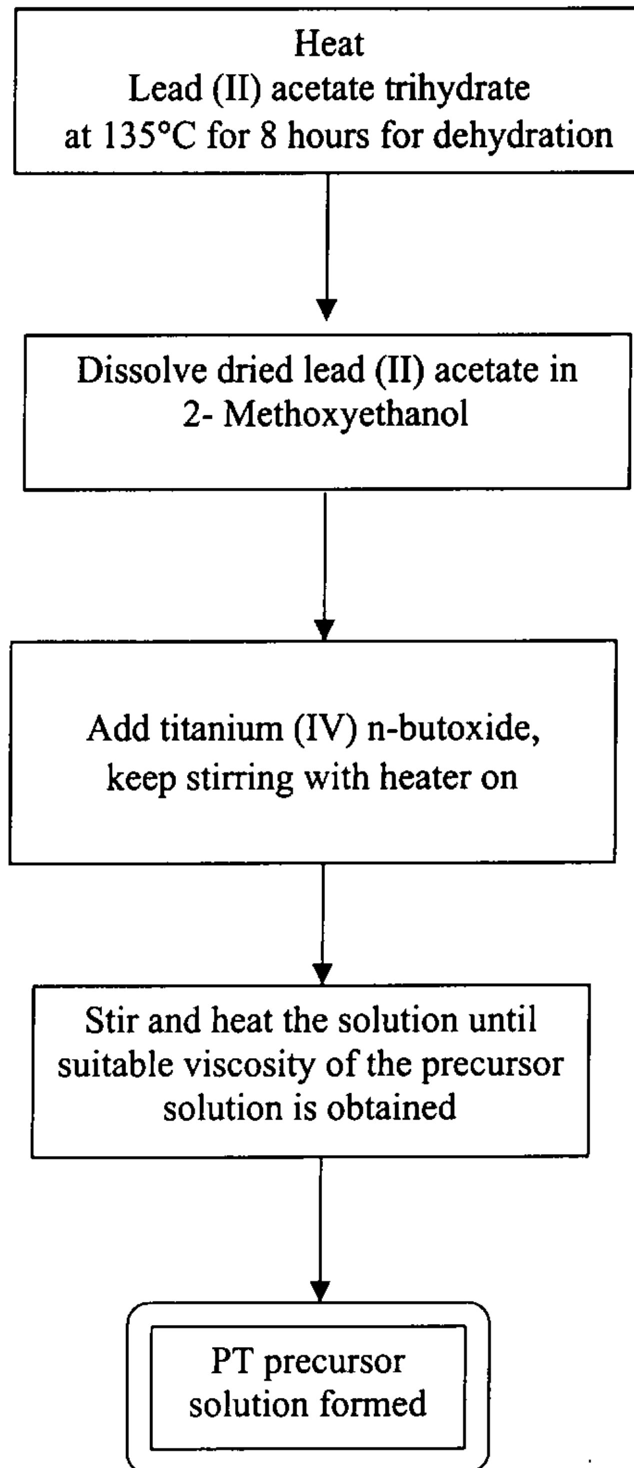

Figure 2.1 Flow chart for the preparation of PT precursor solution.

2.2 Deposition of sol-gel films

Spin-coating technique was used to prepare a PT seeding layer on a $Pt/Ti/SiO_2/Si/Si_3N_4$ substrate from the precursor solution. A dropper was used to drop the PT precursor solution onto the surface of the substrate. The substrate was then spun using a spinner (KW-4A, Chemat Technology) at two different rotation speeds for different periods. First, the spinner was set at a low rotation speed of 800 rpm for 6 seconds to spread the solution over the whole surface of the substrate. Then a high rotation speed of 4500 rpm was used for 50 seconds to obtain a thin layer of film with uniform thickness. The thickness of the film is about 100 nm. After that, the sample ($PT/Pt/Ti/SiO_2/Si/Si_3N_4$) was dried on a hot plate at about 350°C. The sample was covered in order to protect form any dirt in air falling onto it. The dried sample was then crystallized in a rapid thermal processor (RTP 500) at 550°C for 30 min.

Multiple-spin-coating technique was used to deposit PZT thin films on the resulting sample ($PT/Pt/Ti/SiO_2/Si/Si_3N_4$). A dropper was used to drop the PZT precursor solution onto the sample. The spinning conditions were the same as those used for spinning the PT seeding layer. Since the concentration of the PZT solution is lower, about 0.5 M, the thickness of a single layer of the PZT film is about 60 nm. After that, the sample ($PZT/PT/Pt/Ti/SiO_2/Si/Si_3N_4$) was dried on a hot plate at about 300°C. After the deposition of three layers, the sample was pyrolyzed in the rapid thermal processor at 150°C for 3 min, then at 450°C for 10 min and finally at 550°C for 3 min. At 150°C, the solvent in the film was removed

completely. At 450°C, the film decomposed and the organic materials were removed. Finally the film was partially crystallized at 550°C. By repeating the whole process a number of times, a PZT film of thickness 800 nm was obtained. The sample was then annealed at 550°C for 2 hours in a furnace (Lindberg/Blue M) for further crystallization.

2.3 Deposition of top electrodes

A series of platinum top electrodes of diameter 0.8 mm were deposited on the films by dc magnetron sputtering in a pure argon atmosphere. Figure 2.2 shows the schematic diagram of the magnetron sputtering system. A metal platinum (Pt) disc (Kurt J. Lesker, purity 99.99%) of diameter 50.8 mm and thickness 3 mm thick was used as the sputtering target. The dc magnetron gun (Kurt J. Lesker, TORUS 2C) was mounted such that its axis makes an angle of 10° with the normal of the substrate holder, on which the PZT sample was placed. The distance between the sample and the target was 16 cm. During the deposition process, the sample was rotated slowly to ensure that the deposited electrode has a uniform thickness.

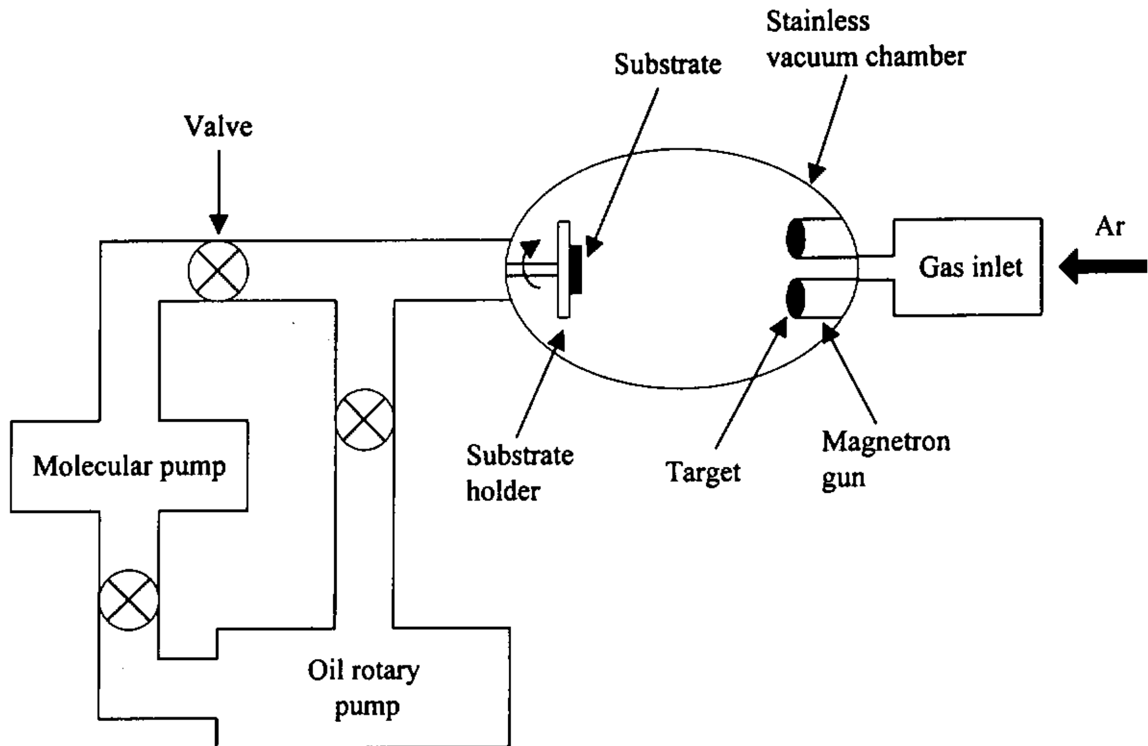

Figure 2.2 Schematic diagram of the magnetron sputtering chamber.

2.4 Crystallite structure of PZT films

An x-ray diffractometer with nickel-filtered CuKα radiation (D8 Discover, Bruker) was used to investigate the crystallite structure of the PZT films (Figure 2.3). A parallel beam of x-ray is directed to incident on the film surface. The diffracted beam was received by a detector which was driven to scan from $2\theta = 20°$ to 60°. When the Bragg's law is satisfied, constructive interference occurs in the diffracted beam and a high-intensity signal is resulted. The Bragg's law is given as:

$$\lambda = 2d \sin \theta \tag{2.1}$$

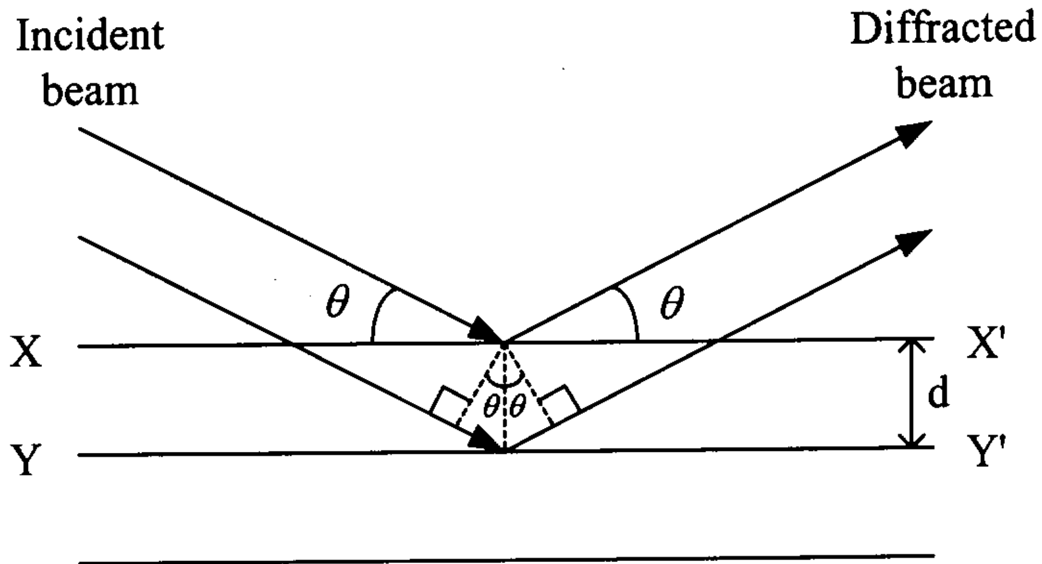

Figure 2.3 Diffraction of x-rays by planes of atoms (X-X' and Y-Y').

The x-ray diffraction (XRD) patterns of the PZT films with 0%, 1% and 2% Nb dopant are shown in Figures 2.4-2.6. It is seen that all the samples exhibit a well-crystallized phase of PZT [Barrow, D. A. *et al.*, 1997; Zhou, Q. F. *et al.*, 1997]. No pyrochlore or PbO_x phases have been observed in all the films. These indicate that, with the presence of a PT seeding layer, the PZT film can completely crystallize at a low temperature such as 550°C.

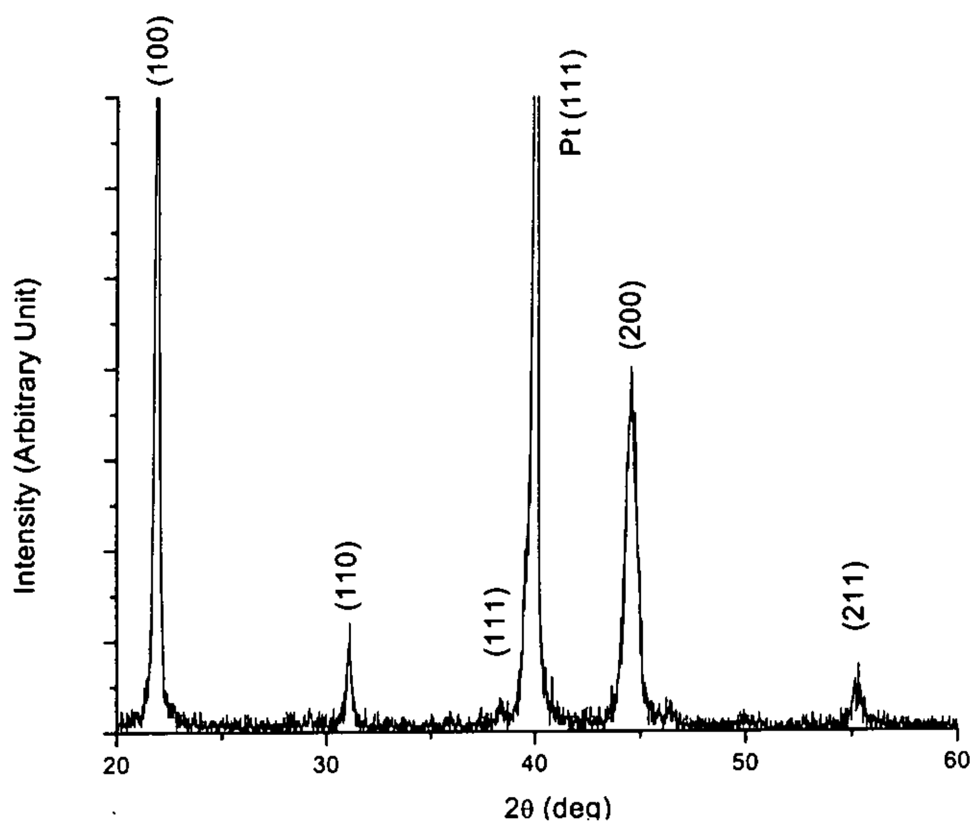

Figure 2.4 XRD pattern of the PZT (53/47) sample with 10% excess lead. The thickness of the film is 800 nm and the film is annealed at 550°C for 2 hours.

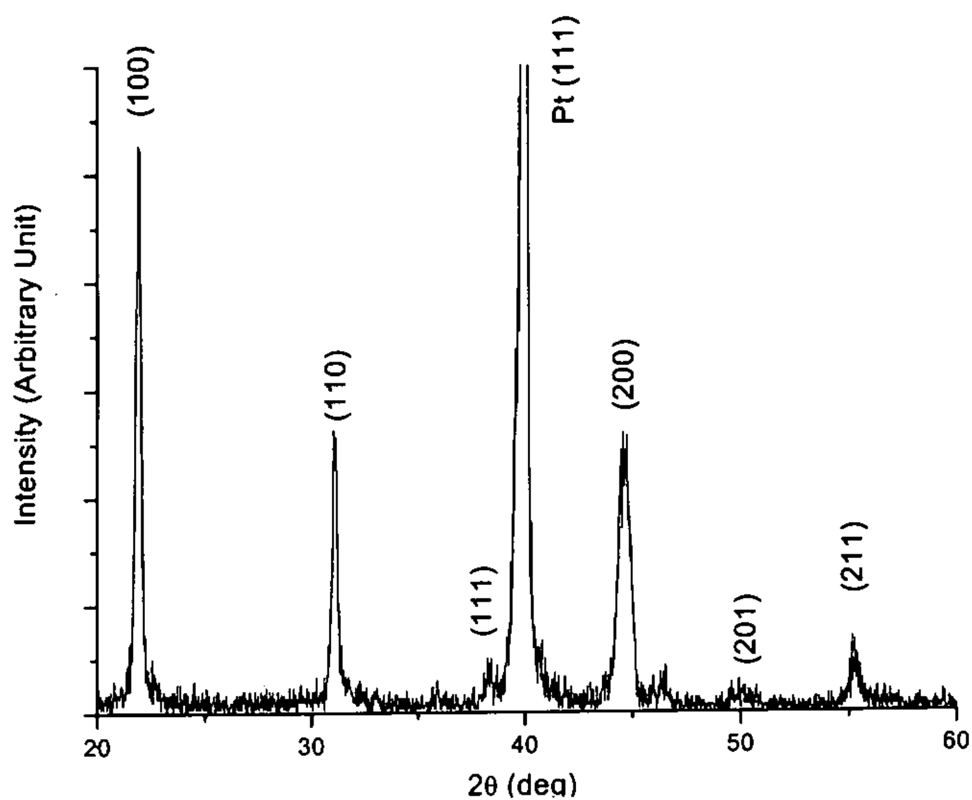

Figure 2.5 XRD pattern of the 1% Nb-doped PZT (1/53/47) sample with 10% excess lead. The thickness of the film is 800 nm and the film is annealed at 550°C for 2 hours.

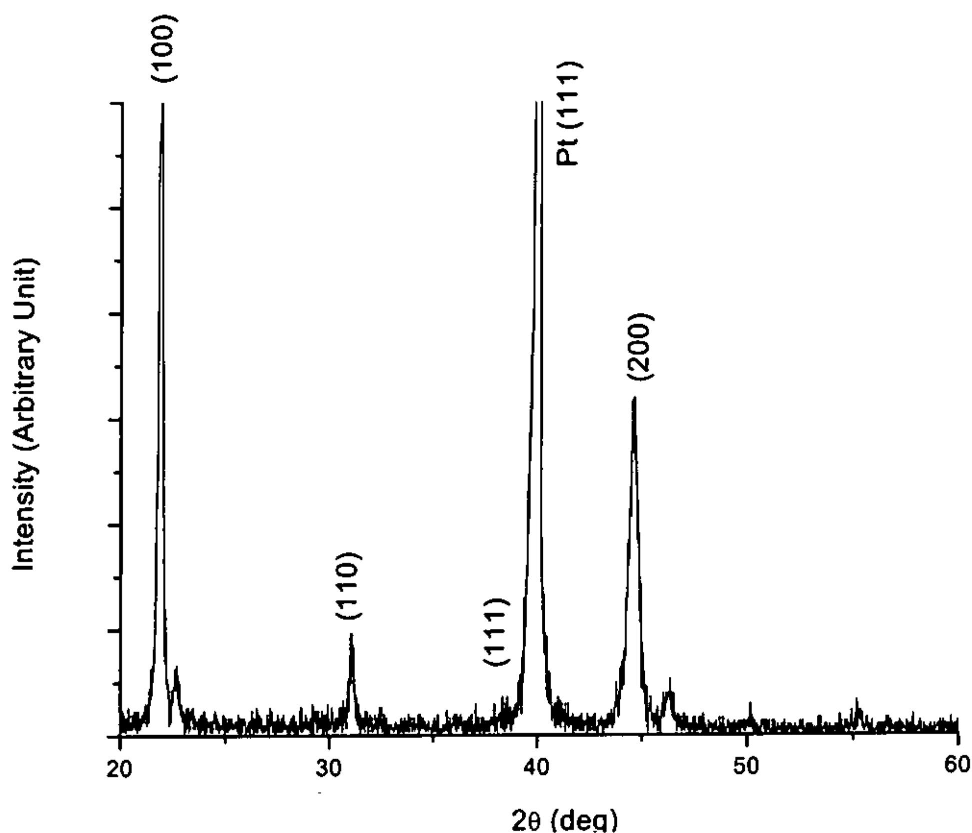

Figure 2.6 XRD pattern of the 2% Nb-doped PZT (2/53/47) sample with 10% excess lead. The thickness of the film is 800 nm and the film is annealed at 550°C for 2 hours.

2.5 Microstructure of PZT films

Scanning electron microscope (SEM) is an instrument that can be used to examine the microstructure of a wide range of materials. The cross section of the PZT films with 0%, 1% and 2% Nb dopant was examined using a scanning electron

microscope (Leica, Steoreo 440). Figure 2.7 shows the micrograph of the cross section of the 1% Nb-doped PZT film. It is seen that the film is quite dense and has uniform thickness. Similar microstructures have also been observed for the other PZT films with 0% and 2% Nb dopant.

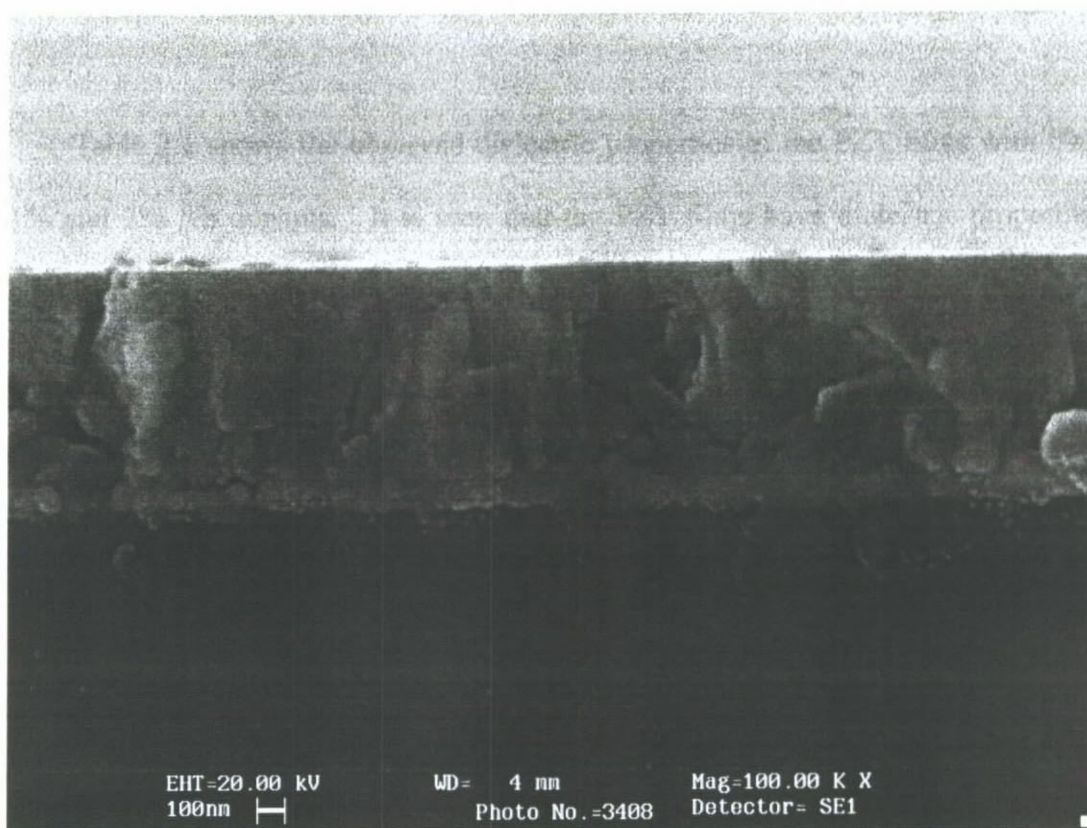

Figure 2.7 SEM micrograph of the cross section of the 1% Nb-doped PZT film. The thickness of the film is 800 nm.

2.6 Dielectric properties of PZT films

In this project, the capacitance and dielectric loss (tan δ) of the samples were measured using an impedance analyzer (HP 4194A, Hewlett Packard), and the relative permittivity ε_r was calculated from the following equation:

$$C = \frac{\varepsilon_o \cdot \varepsilon_r \cdot A}{d} \qquad (2.2)$$

where C is the capacitance, A is the area of the sample (with electrode), d is the thickness of the sample, and ε_o is the permittivity of free space (= 8.85×10^{-12} F/m). All the measurements were done at room temperature.

Table 2.1 shows the observed dielectric properties of the PZT films with 0%, 1% and 2% Nb dopants. It is seen that the PZT films have dielectric properties comparable to the other sol-gel derived PZT films. As the Nb content increases from 0 to 2 %, the observed ε_r value decreases from 1276 to 935, while the dielectric loss decreases slightly, remains at about 0.05. These indicate that the PZT films should have reasonably good properties.

Table 2.1 The capacitance, relative permittivity ε_r and tan δ of the PZT thin films (800 nm) with different Nb dopant contents.

	0% Nb	1% Nb	2% Nb
Capacitance (nF)	7.1	6.2	5.2
Relative permittivity ε_r	1276	1115	935
Dielectric loss tanδ	0.048	0.041	0.036

Chapter Three

Effects of Nb Dopant on Piezoelectric Properties of PZT Films

3.1 Measurement of longitudinal piezoelectric coefficient

The piezoelectric coefficients for the direct and converse piezoelectric effects have been defined in Chapter 1. In the present study, the longitudinal piezoelectric coefficient d_{33} for the converse piezoelectric effect was determined. As mentioned before, all the film samples were deposited on silicon substrates. Since the film is laterally clamped by the substrate, it cannot deform freely in the lateral directions. The suppression of the lateral deformation of the film (or clamping) by the substrate will cause the observed piezoelectric coefficient different from the true value. The observed piezoelectric coefficient (or effective piezoelectric coefficient) d_{33}' for a film completely clamped on a substrate is related to the true piezoelectric coefficient d_{33} by [Royer, D. and Kmetik, V. 1992]:

$$d_{33}' = d_{33} - \frac{2s_{13}^E}{s_{11}^E + s_{12}^E} d_{31} \qquad (3.1)$$

For PZT, s_{11}^E is positive, s_{12}^E, s_{13}^E and d_{31} are negative [Auld, B. A. 1990, pp.373-375]. Therefore, the observed d_{33}' value for a PZT film is smaller than the observed d_{33} value for a bulk sample.

The schematic diagram of the experiment setup for the measurement of d_{33}' is shown in Figure 3.1. An electric field is applied to the sample and the induced strain along the thickness direction is measured. Due to the small thickness of the PZT films, the surface displacement lies in the Angstrom range (i.e. 10^{-10} m). A Mach-Zehnder type heterodyne (single beam) laser interferometer (SH-120, B.M. Industries, France) was then used to measure the surface displacement of the films.

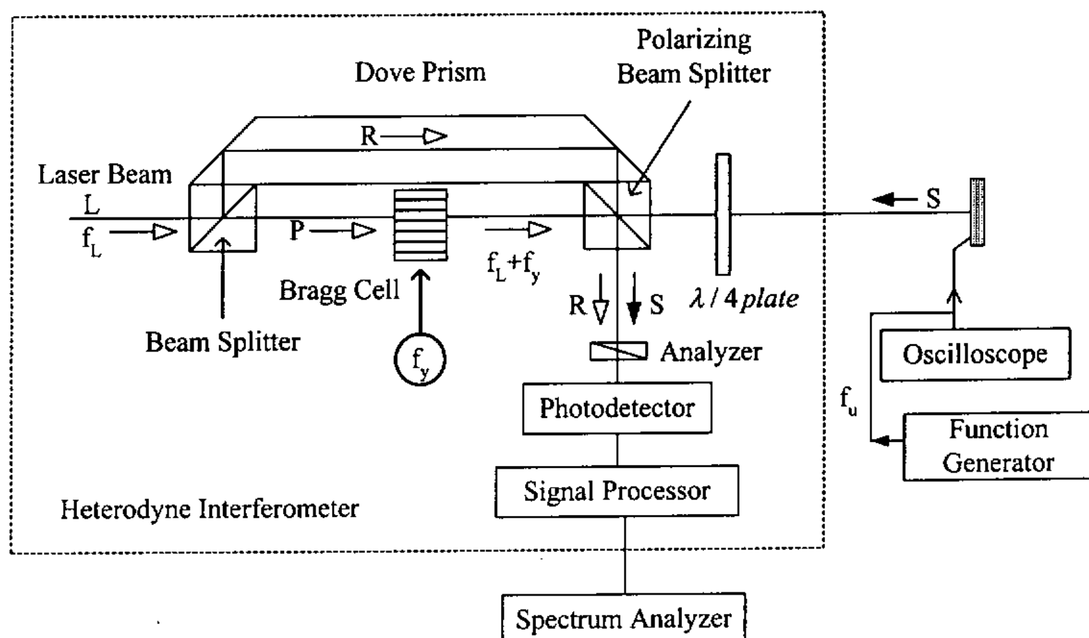

Figure 3.1 Schematic diagram of the experimental setup for the d_{33}' measurement.

A function generator (HP 8116A, Hewlett Packard) was used to apply an ac field across the film sample. The actual voltage applied to the sample was measured using a digital storage oscilloscope (HP 54345A, Hewlett Packard). The induced surface displacement of the sample was measured using by the single beam laser interferometer. The current signal from the interferometer was measured using a spectrum analyzer (HP 3589A, Hewlett Packard).

The He-Ne laser in the interferometer generates a linearly polarized laser beam L (frequency f_L and wavelength λ_L = 632.8 nm). The complex amplitude of the laser beam can be written as:

$$L = le^{i2\pi f_L t} \tag{3.2}$$

where l is the amplitude of the laser beam L and t is time. The laser beam L is split into a reference beam R and a probe beam P by a beam splitter. The reference beam R passes through a Dove prism and a polarizing beam splitter and impinges upon a photodetector directly. The complex amplitude of the reference beam R can be written as:

$$R = re^{i2\pi f_L t} \tag{3.3}$$

where r is the amplitude of the reference beam R. The probe beam P passes through a Bragg cell located between two beam splitters, in which its frequency is shifted by f_y (70 MHz). The frequency-shifted probe beam then impinges upon the sample surface and is phase modulated by the surface displacement of the sample. The complex amplitude of the probe beam (now labeled as S) is then given as:

$$S = se^{i(2\pi f_L + 2\pi f_y)t + \phi(t)} \tag{3.4}$$

where s is the amplitude of the phase modulated beam S and

$$\phi(t) = 2k_L X \sin(2\pi f_x t) \tag{3.5}$$

where $k_L = \frac{2\pi}{\lambda_L}$ (i.e. wave number), f_x and X are the vibrating frequency and displacement amplitude of the sample, respectively.

Both the beams R and S are directed into a photodetector. The interference of the beams R and S on the photodetector delivers a current I at frequency f_Y, phase modulated by the surface displacement of the sample:

$$I \propto \cos\left[2\pi f_y t + 2k_L X \sin(2\pi f_x t)\right] \tag{3.6}$$

The current I can be expanded into a Bessel development:

$$I \propto \mathrm{Re}\left\{e^{i2\pi f_y t}\left[J_o\left(\frac{4\pi X}{\lambda_L}\right) + 2iJ_1\left(\frac{4\pi X}{\lambda_L}\right)\sin(2\pi f_x t) + 2iJ_2\left(\frac{4\pi X}{\lambda_L}\right)\sin(4\pi f_x t) + \ldots\right]\right\} \tag{3.7}$$

For small displacement amplitude, the ratio of the amplitudes of the current components at f_y and $f_y \pm f_x$ can be approximated as:

$$\frac{J_o\left(\frac{4\pi X}{\lambda_L}\right)}{J_1\left(\frac{4\pi X}{\lambda_L}\right)} \cong \frac{\lambda_L}{2\pi X} \tag{3.8}$$

where J_o and J_1 are the Bessel functions of the zeroth and the first order, respectively. Therefore, by the measurement of the amplitudes of the current components (in dBm) at f_y (A_o) and $f_y \pm f_x$ (A_1) (Figure 3.2), the displacement amplitude can be calculated as:

$$X = \frac{\lambda_L}{2\pi 10^{\left(\frac{A_o - A_1}{20}\right)}} \tag{3.9}$$

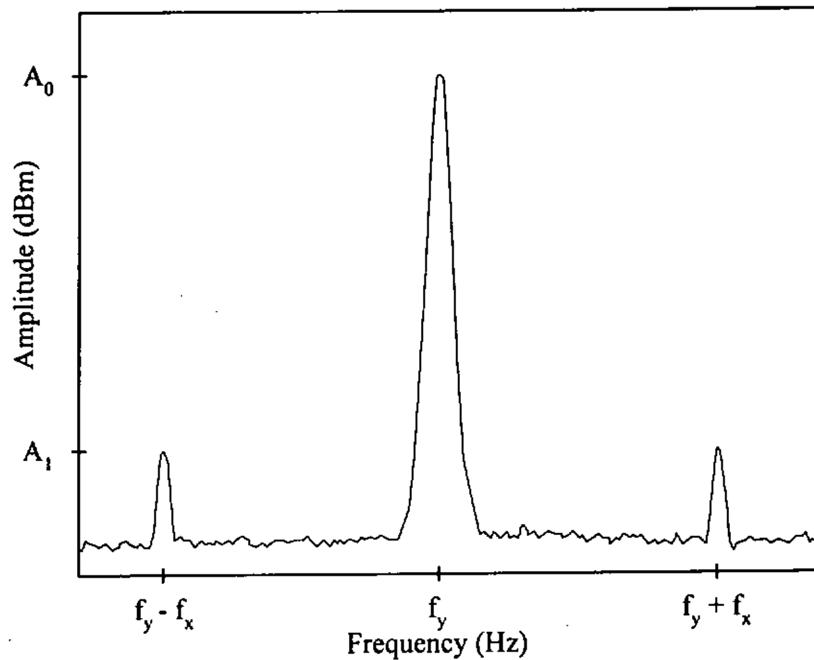

Figure 3.2 Frequency spectrum of the signal current I recorded by a spectrum analyzer.

The effective piezoelectric coefficient d'_{33} of the film can be calculated as:

$$d'_{33} = \frac{S_3}{E_3} = \frac{X/d}{V/d} = \frac{X}{V} \tag{3.10}$$

where d is the thickness of the film and V is the voltage applied across the film.

3.1.1 Sample preparation for the d_{33} measurement

After the film samples have been fabricated, they cannot be placed on a sample holder for the measurement directly. Since the film sample is tightly adhered on a substrate, its lateral deformation is restricted by the substrate. However, lateral stresses are also imposed on the substrate by the film. If the substrate is not tightly fixed to a large rigid platform, these lateral stresses will bend the substrate as shown

in Figure 3.3. Both the displacement of this bending (ΔX) and the thickness change (S_3) will be measured by the single beam laser interferometer at the same time, making the observed d_{33}' value becomes larger than the actual value. To eliminate this error, the sample (film/substrate) was glued tightly on a large rigid printed circuit board (PCB) using a mounting wax (Mounting wax, Gatan) in the present work. Figure 3.4 shows the sample fixture for the d_{33} measurement. Since the PCB is much larger and thicker than the sample, it can provide a stiff and stable platform in order to suppress the bending of the substrate and hence to eliminate the error.

Since the diameter of the top electrode is 0.8 mm only, it is quite difficult to apply the electrical and optical signals (the diameter of the laser beam is 0.4 mm) to the electrode at the same time for the measurement. Hence, the top electrode was electrically connected to a large electrode pad on the PCB through a thin wire (diameter = 40 μm) using a wire-bonder (AB510, ASM). The electric field was then applied on the electrode pads.

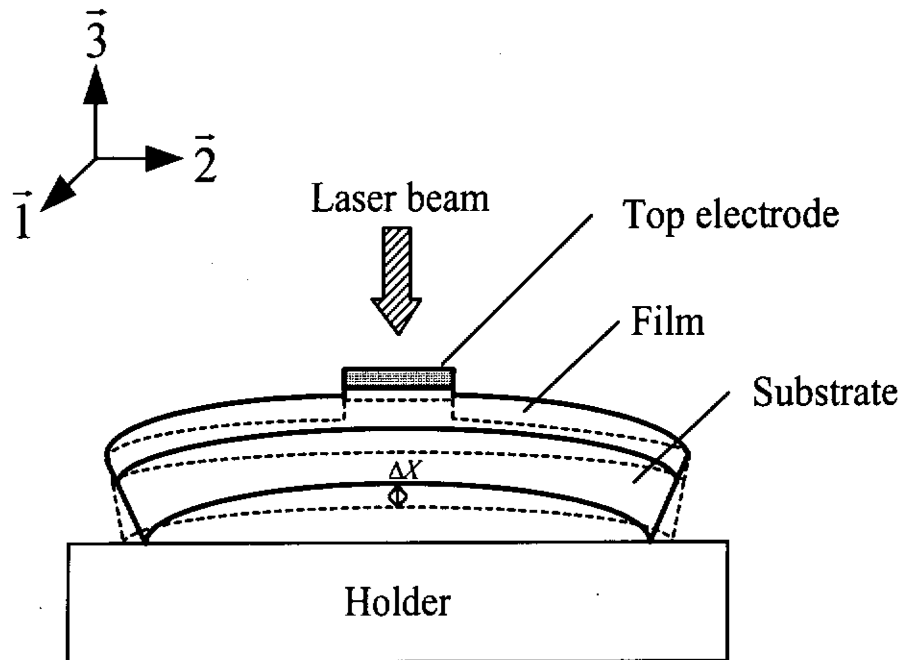

Figure 3.3 Bending of the substrate in the $d_{33}^{'}$ measurement.

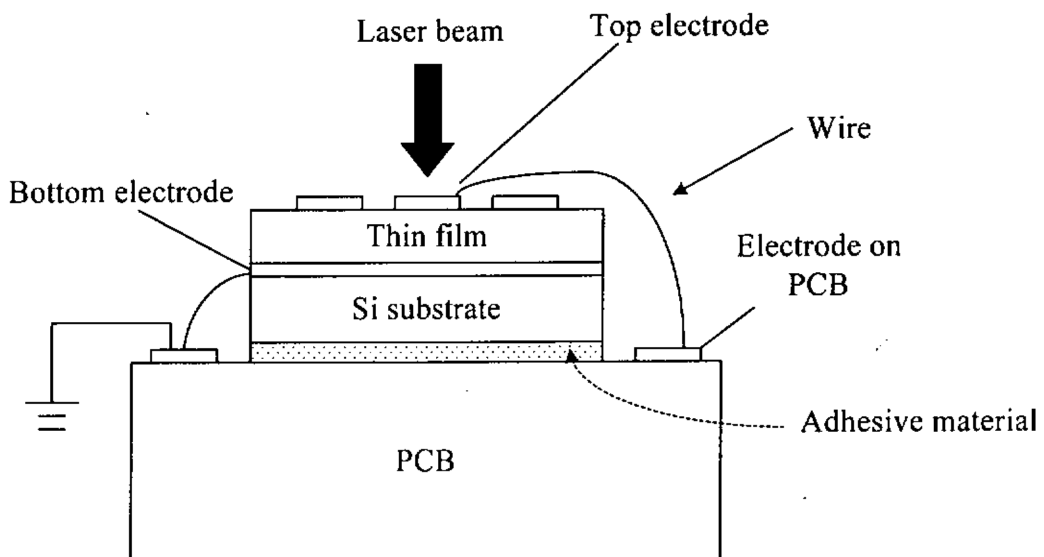

Figure 3.4 Sample fixture for the $d_{33}^{'}$ measurement.

3.2 Measurement of effective transverse piezoelectric coefficient

The transverse piezoelectric coefficient e_{31} is another important parameter for MEMS actuators. The experimental setup for the e_{31} measurement is schematically shown in Figure 3.5. In the measurement, a rectangular sample (film/substrate) is clamped at one end while the other end is left free. A piezoelectric actuator is used to apply a dynamic force to the free end for bending the sample. A longitudinal strain is generated along the length of the sample ($\bar{1}$) and charge is hence induced on the film surface due to the direct piezoelectric effect. The film is only laterally clamped by the substrate; it can deform freely along the thickness direction ($\bar{3}$). Because of the Poisson contraction of the substrate, the substrate and hence the film deform along the width direction ($\bar{2}$). Therefore, the observed transverse piezoelectric coefficient (or effective transverse piezoelectric coefficient) $e_{31,f}$ is different from the normal transverse piezoelectric coefficient e_{31}, for which only a dimensional change in direction $\bar{1}$ is allowed.

Figure 3.5 Experimental set-up for the $e_{31,f}$ measurement.

As mentioned, the rectangular sample is bent in order to generate a longitudinal strain or stress along the length of the sample ($\bar{1}$) (Figure 3.5). The constitutive equations for the system are:

$$D_i = d_{ip}T_p + \varepsilon_{ij}E_j \quad (3.11)$$

$$S_p = s_{pq}^E T_q + d_{pi}E_i \quad (3.12)$$

where D_i is the electric displacement, E_i is the electric field, T_p is the stress, S_p is the elastic strain, d_{ip} is the piezoelectric coefficient, ε_{ij} is the relative permittivity, s^E_{pq} is the elastic compliance at constant electric field, $i, j = 1, 2, 3$ and $p, q = 1, 2, 3, 4, 5, 6$. Since the film is clamped by the substrate and can deform freely along the $\bar{3}$ direction, $T_3 = T_4 = T_5 = T_6 = 0$. There is no external field applied to the sample, so $E_1 = E_2 = E_3 = 0$. The constitutive equations can then be simplified as:

$$D_3 = d_{31}T_1 + d_{31}T_2 \quad (3.13)$$

$$S_1 = s^E_{11}T_1 + s^E_{12}T_2 \quad (3.14a)$$

$$S_2 = s^E_{12}T_1 + s^E_{11}T_2 \quad (3.14b)$$

$$S_3 = s^E_{13}T_1 + s^E_{13}T_2 \quad (3.14c)$$

By summing Equations 3.14a and 3.14b, it gives:

$$T_1 + T_2 = \frac{S_1 + S_2}{s^E_{11} + s^E_{12}} \quad (3.15)$$

Substitute Equation 3.15 into 3.13,

$$D_3 = \frac{S_1 + S_2}{s^E_{11} + s^E_{12}} d_{31} \quad (3.16)$$

Hence the effective transverse piezoelectric coefficient $e_{31,f}$ can be determined as:

$$e_{31,f} = \frac{D_3}{(S_1 + S_2)} = \frac{d_{31}}{s^E_{11} + s^E_{12}} \quad (3.17)$$

As the film is much thinner than the substrate, it can be assumed that the strains S_1 and S_2 are the same throughout the thickness of the film, and their values are the same as those of the substrate. Therefore, S_2 can be linked to S_1 by the Poisson's ratio υ_c of the substrate material, i.e.

$$S_2 = -\upsilon_c S_1 \quad (3.18)$$

Equation 3.17 then becomes

$$e_{31,f} = \frac{D_3}{(1-\upsilon_c)S_1} \quad (3.19)$$

For a rectangular sample with the end clamped (or named cantilever, Figure 3.4), the deflection in the $\bar{3}$ direction, z, as a function of x (the position along the $\bar{1}$ direction) is described by [Timoshenko, S. P. *et al.*, 1970]:

$$z = \frac{F}{6YI}\left(3\ell x^2 - x^3\right) \quad (3.20)$$

$$I = \frac{bh^3}{12} \quad (3.21)$$

where F is the force applied at the free end by the actuator to bend the cantilever, ℓ, b and h are the length, width and thickness of the cantilever, respectively, and Y is the Young's modulus of the substrate. At the free end of the cantilever, i.e. $x = \ell$, the deflection has the maximum value, z_m, as:

$$z_m = \frac{F\ell^3}{3YI} \quad (3.22)$$

The radius of curvature R of the cantilever can be approximated as:

$$\frac{1}{R} = \frac{d^2 z}{dx^2} \quad (3.23)$$

By using the second derivative of Equation 3.20, Equation 3.23 becomes

$$\frac{1}{R} = \frac{F}{YI}(\ell - x) \quad (3.24)$$

Then by substituting Equation 3.22 into Equation 3.24, a general expression for the curvature is obtained as:

$$\frac{1}{R} = \frac{3z_m(\ell - x)}{\ell^3} \quad (3.25)$$

The strain S_1 at the surface of the cantilever is, therefore:

$$S_1 = \frac{h}{2R} = \frac{3hz_m(\ell - x)}{2\ell^3} \tag{3.26}$$

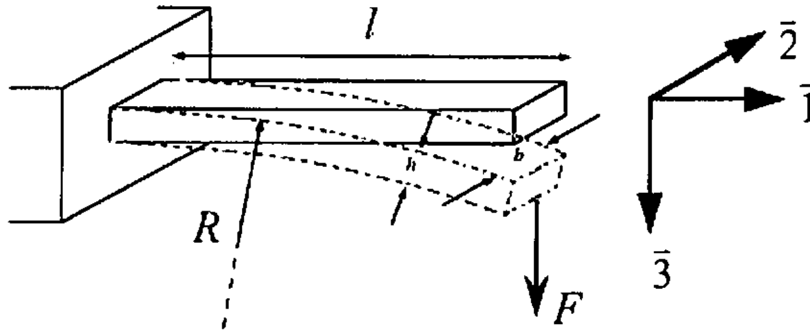

Figure 3.6 Schematic diagram showing the bending of the cantilever. F is the force applied by the actuator, R is the radius of curvature of the cantilever, ℓ is the length of the cantilever, b is the width of the cantilever and h is the thickness of the cantilever.

Due to the direct piezoelectric effect, charge Q is induced on the surface of the electrode of area A:

$$\begin{aligned} dQ &= D_3 \cdot dA \\ &= e_{31,f}(1-\upsilon_c)S_1 \cdot dA \\ &= \frac{3hz_m e_{31,f}(1-\upsilon_c)}{2\ell^3}(\ell - x)\cdot dA \end{aligned} \tag{3.27}$$

For a circular top electrode with its extremities located at x_a and x_b (Figure 3.7),

$$dA = 2\sqrt{r^2 - \kappa^2} \cdot dx \tag{3.28}$$

where $r = (x_b - x_a)/2$ is the radius of the top electrode, and

$$\kappa = x - \frac{x_a + x_b}{2} \tag{3.29}$$

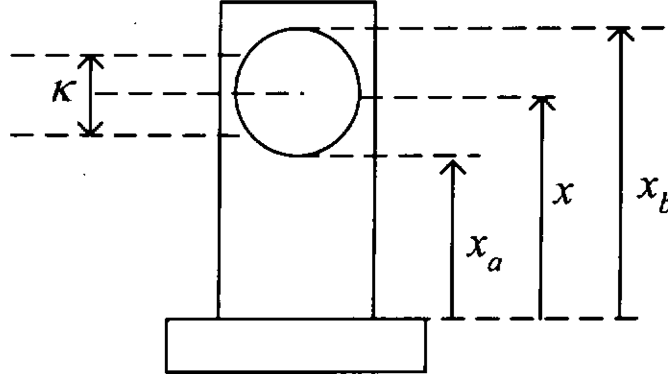

Figure 3.7 Schematic diagram showing the position of a top circular electrode.

Therefore, the induced charge on the circular top electrode is given by:

$$dQ = \frac{3hz_m e_{31,f}(1-\upsilon_c)}{\ell^3}(\ell - x)\sqrt{r^2 - \kappa^2} \cdot dx \tag{3.30}$$

$$Q = \frac{3hz_m e_{31,f}(1-\upsilon_c)}{\ell^3}\int_{x_a}^{x_b}(\ell - x)\sqrt{r^2 - \kappa^2} \cdot dx$$

$$= \frac{3hz_m e_{31,f}(1-\upsilon_c)}{\ell^3}\frac{\pi r^2}{2}\left[\ell - \frac{x_a + x_b}{2}\right] \tag{3.31}$$

Since a dynamic force at frequency f (=$\omega/2\pi$) is applied to bend the sample, the deflection at the free end z_m and hence the induced charge Q are time varying at the same frequency, i.e.

$$Q(t) = \frac{3\pi r^2 hz_m e_{31,f}(1-\upsilon_c)}{2\ell^3}\left[\ell - \frac{x_a + x_b}{2}\right] \cdot e^{i\omega t} \tag{3.32}$$

Therefore, a current signal I_c (magnitude) is resulted:

$$I_c = \frac{dQ}{dt} = \frac{3\pi r^2 \omega hz_m e_{31,f}(1-\upsilon_c)}{2\ell^3}\left[\ell - \frac{x_a + x_b}{2}\right] \tag{3.33}$$

In this work, a piezoelectric actuator (ASB003A, Tokin Inc.) was used to apply a dynamic force to bend the sample. A function generator (HP8116A, Hewlett-Packard) and a power amplifier (BOP1000, KEPCO) were used to drive the actuator at a frequency f of 10 Hz. The deflection at the end of the sample was measured using a photonic sensor (MTI-2000, Mechanical Technology Inc.). The current I induced on the circular top electrode was measured using a lock-in amplifier (SR830 DSP, Stand Research Systems). Then the effective transverse piezoelectric coefficient $e_{31,f}$ was calculated from Equation 3.33.

Similar to the d_{33} measurement, the sample (film/substrate) was glued on a PCB (Figure 3.8), and the top electrode was electrically connected to a large electrode pad on the PCB through a thin wire (diameter = 40 μm) using a wire-bonder (AB510, ASM) for the ease of the measurement of the induced current. The top electrode is wire bonded to the electrode pad on the PCB for the ease of collection of the charge from the sample. The thin wire is long enough that it will not affect the bending of the cantilever.

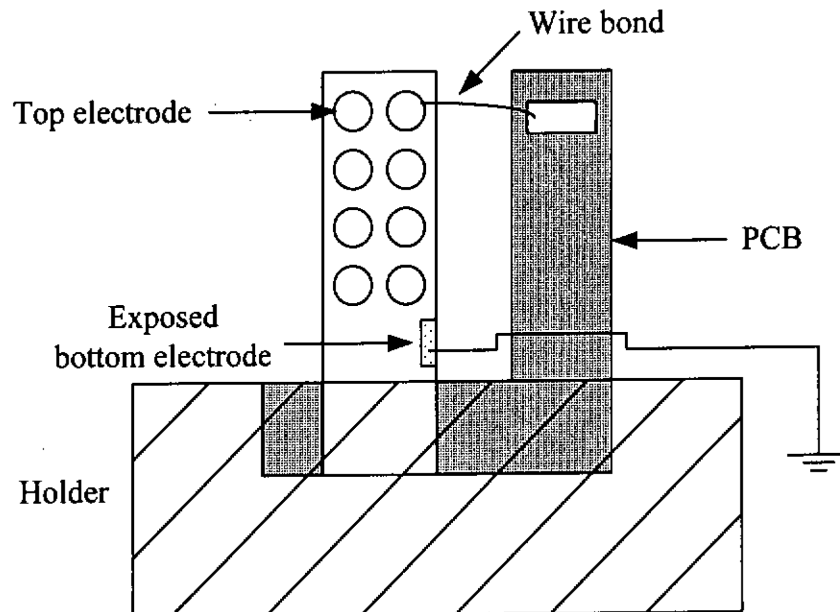

Figure 3.8 The sample fixture for the $e_{31,f}$ measurement.

3.3 Result and discussion

After the piezoelectric films have just been fabricated, they do not exhibit any piezoelectric effect because of the random orientation of the ferroelectric domains in the ceramics. A strong external electric field is needed to align the domains to the field direction so as to induce the piezoelectricity of the sample (Figure 3.9). This process is called poling. In present work, the film samples are poled by an external dc field at room temperature.

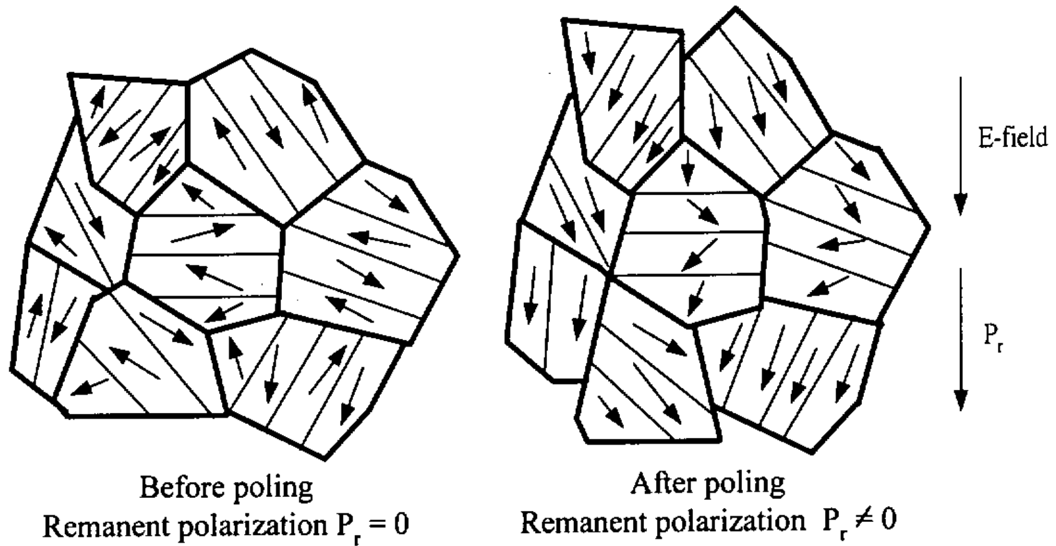

Figure 3.9 Schematic diagram showing an as-prepared polycrystalline sample with random orientation of grains before poling, and an poled sample with the grains aligned to the field direction.

The experimental setup for poling the PZT film samples is shown in Figure 3.10. The positive terminal of a dc source is connected to the top electrode of the film sample. The bottom electrode is grounded. The poling field is increased from 5 MV/m to 25 MV/m, in steps of 5 MV/m. At each field, the sample is poled for 5 min. Our results reveal that the piezoelectric coefficients of the films are saturated at a poling field of 25 MV/m, indicating that the films are fully poled.

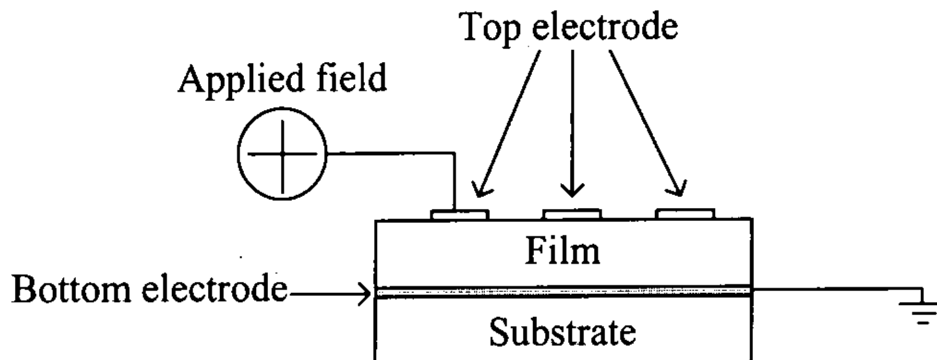

Figure 3.10 A schematic diagram of the experimental setup for poling.

Before studying the effects of Nb dopant on the piezoelectric properties of the PZT films, the d'_{33} and $e_{31,f}$ measurements were first evaluated using a fully poled PZT film sample (with 0% Nb). For the d'_{33} measurement, the frequency of the applied voltage was 15 kHz and the amplitude ranged from 0.1 V to 0.7 V (or 0.125 MV/m to 0.875 MV/m). Figure 3.13 shows the surface displacement as a function of applied voltage. It can be seen that the relation between the displacement and the applied voltage is quite linear and passes through zero, indicating that the applied voltage is not so large to exceed the linear region of the piezoelectric effect. Furthermore, this also indicates that the d_{33} measurement is in principle correct and free from any significant systematic error.

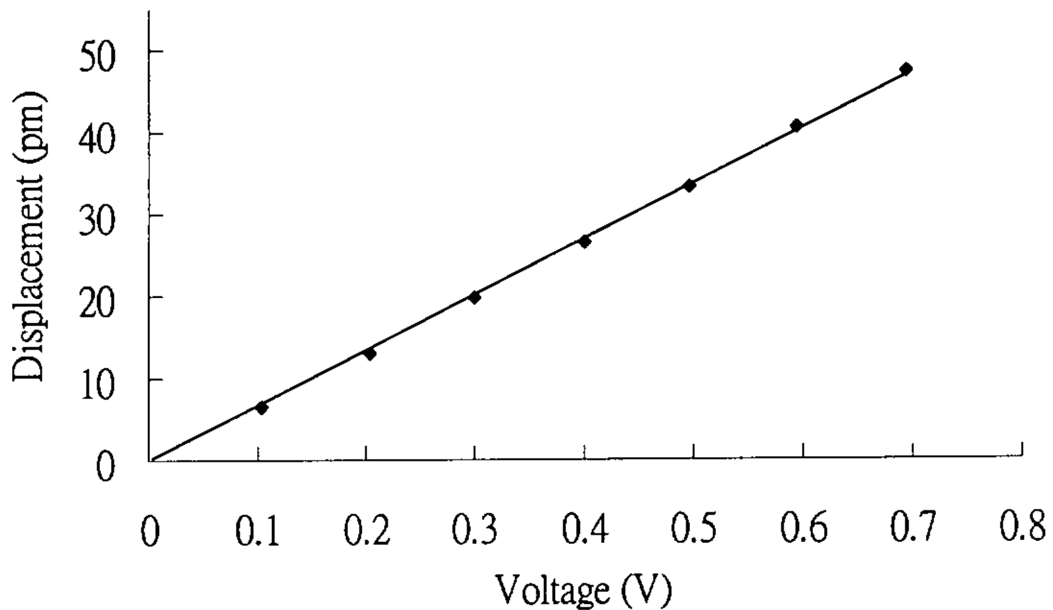

Figure 3.11 Variation of the surface displacement with applied voltage for the PZT film (with 0% Nb). The thickness of the film is 800 nm.

As mentioned, if the substrate is bent by the lateral clamping stresses in the d_{33} measurement, enormous error will be resulted. In order to suppress the bending, the substrate was glued tightly on to a large PCB by using a mounting wax in this work. In order to check the effectiveness of the gluing method, the distribution of the surface displacements across the sample has been measured. In doing this, a small electric field of magnitude 0.5 MV/m and frequency 15 kHz was applied at the driving electrode (Figure 3.11), and the surface displacement at this electrode as well as at the electrodes adjacent to it (nearest electrodes) was measured using the single beam laser interferometer. The center to center distance between the electrodes is 2 mm. Figure 3.12 shows the surface displacements at the driving and the nearest electrodes of the PZT film sample. It can be seen that the surface displacement at the driving electrode is quite large, about 47 pm. Beyond the

driving electrode, the surface displacement decreases drastically. The average surface displacement of the nearest electrodes is 5 pm. This indicates that the substrate is tightly clamped and the bending is successfully suppressed. It should be noted that the experimental error of d'_{33} measurement is about ± 10%.

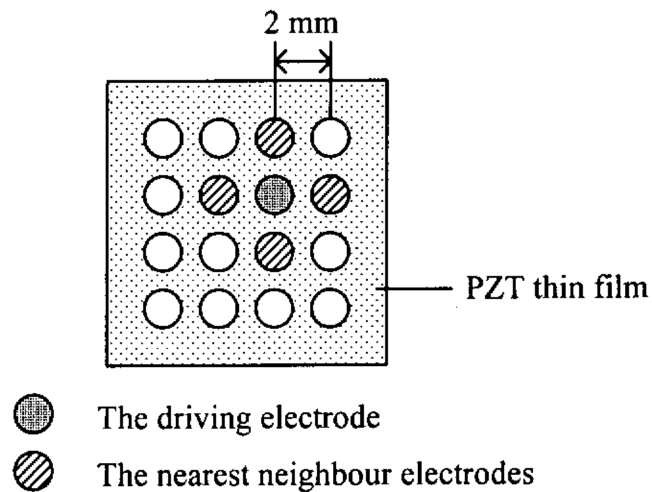

Figure 3.12 The arrangement of the electrodes for the d'_{33} measurement.

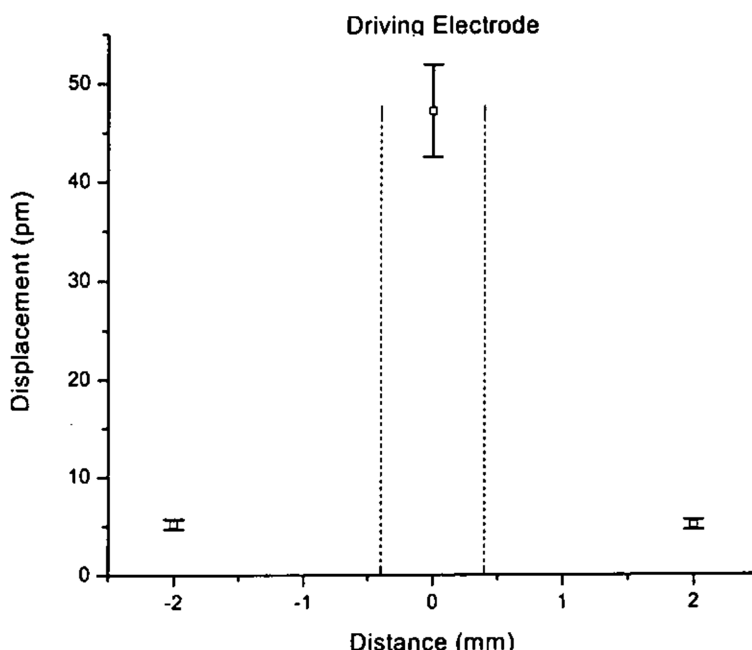

Figure 3.13 Distribution of the surface displacement across the PZT film sample. The driving electrode (indicated by the dot lines) is located at centre.

After the accuracy of the d_{33} measurement had been confirmed, the effective piezoelectric coefficients of the PZT films with various amounts of Nb dopant were determined. The films were fully poled under a dc field of 25 MV/m at room temperature. A small ac electric field of frequency 15 kHz and magnitude ranging from 0.125 - 0.875 MV/m was applied to the sample; and the induced surface displacement was measured. The observed $d_{33}^{'}$ value was then calculated from the slope of the linear relationship between the displacement and the applied voltage. The variation of the observed $d_{33}^{'}$ value with Nb-dopant content is shown in Figure 3.14. The observed $d_{33}^{'}$ value of the PZT film sample (with 0% Nb) is about 68 pm/V, which is lower than the value of a PZT film of similar composition

but without a PT seeding layer and annealed at 650°C (85 pm/V) [R. C. W. Tsang *et al.*, 2002. This is probably due to the lower sintering temperature (550°C), and hence the smaller grain size of the film [Tsang, R. C. W. *et al.*, 2002; Ishikawa, K. *et al.*, 1998]. Nevertheless, the observed $d_{33}^{'}$ value is quite large, indicating that, with the presence of a PT seeding layer, the PZT film can crystallize well at a low temperature of 550°C and has good piezoelectric properties.

As shown in Figure 3.14, the observed $d_{33}^{'}$ value of the 1% Nb-doped PZT film is slightly higher (about 9%) than that of the un-doped PZT film, while that of the 2% Nb-doped PZT film is lower. The optimum doping level of Nb for PZT films is then about 1%. This is similar to the PZT ceramics that the piezoelectric properties of the PZT film can be improved by an optimized doping level of Nb.

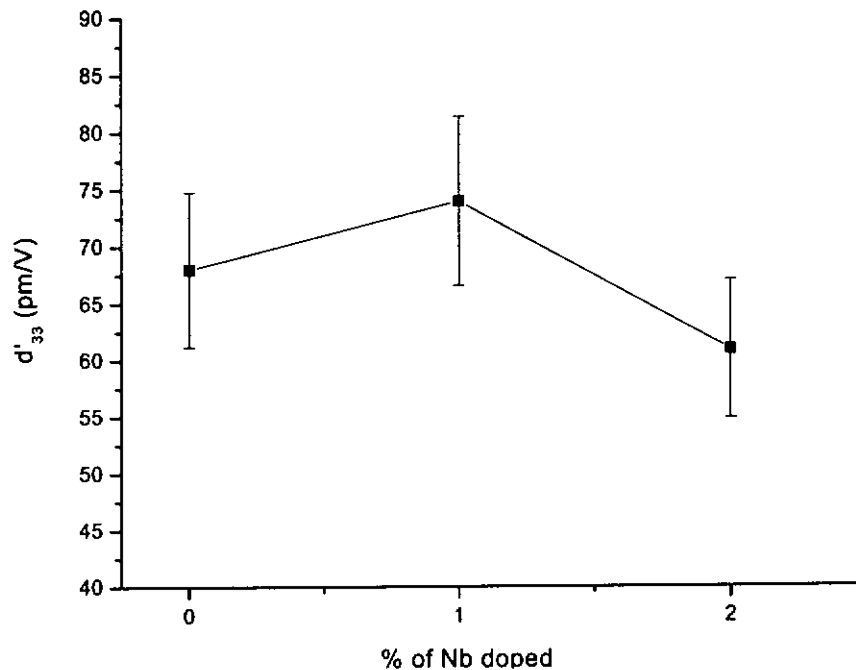

Figure 3.14 Effective piezoelectric coefficient $d_{33}^{'}$ as a function of Nb-dopant content for the PZT films. The thickness of the films is 800 nm.

Similarly, the $e_{31,f}$ measurement was first evaluated using a fully poled PZT film sample (with 0% Nb). Figure 3.15 shows the induced current (I_c) as a function of the deflection at the free end (z_m) for the PZT film with the top electrode located at x = 7.8 mm (refer to Figure 3.7). A linear relation between I_c and z_m is obtained, and the straight line passes through the origin. This suggests that, according to Equation 3.33, the measurement is in principle correct and no significant systematic error exists. In this work, a Poisson ratio of silicon substrate v_c = 0.172 [Brantley, W. A. 1973] was used to calculate the $e_{31,f}$ value from the slope of the straight line. It should be noted that since a number of observed values was used for the calculation (Equation 3.33), the resulting experimental error

for the observed $e_{31,f}$ value is about ±10%.

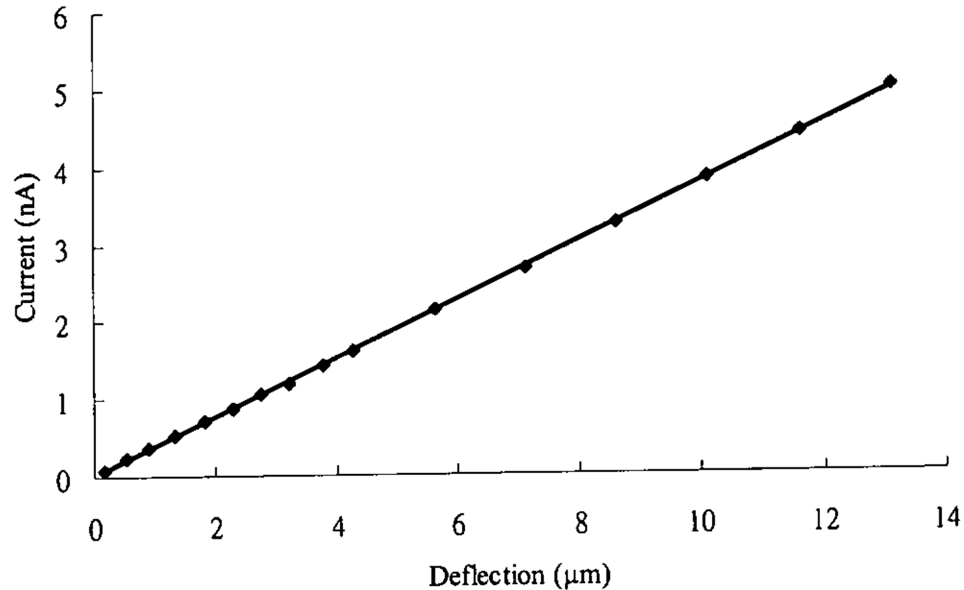

Figure 3.15 Induced current as a function of the deflection at the free end of the cantilever for the 0% Nb doped PZT film.

The variation of the observed $e_{31,f}$ value with Nb-dopant content is shown in Figure 3.16. Similar to the case for d'_{33}, the observed $e_{31,f}$ value reaches a maximum value (12.8 C/m^2) at 1% Nb-dopant content, indicating that the optimum doping level of Nb for PZT films is about 1%. However, unlike d'_{33}, the increment in $e_{31,f}$ for the 1% Nb-doped PZT film is much larger, about 30%, as compared to that in d'_{33} (9%). This seems to be different from the effects experimentally found on PZT ceramics. It has been shown that for PZT bulk ceramics of similar compositions (Zr/Ti = 52/48) with 2 mol% Nb dopant, both d_{33} and d_{31} are increased by almost the same large amount: about 60% and 80%, respectively [Jaffe, B. *et al.*, 1971]. The difference in the optimum doping level

between the PZT films and bulk ceramics (1% vs 2%) is probably partly due to the experimental error in preparing the samples.

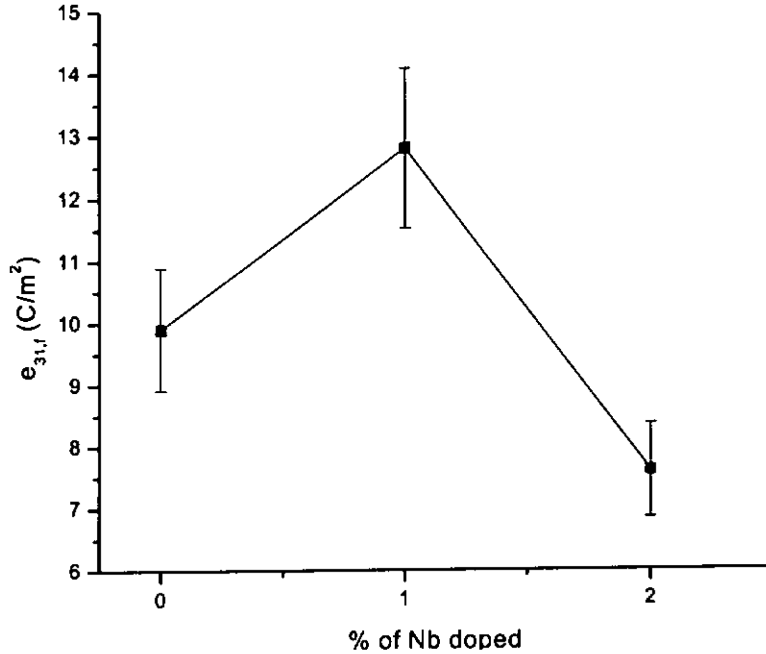

Figure 3.16 Effective piezoelectric coefficient $e_{31,f}$ as a function of Nb-dopant content for the PZT films. The thickness of the films is 800 nm.

However, the apparent difference in the change of the observed $d_{33}^{'}$ and $e_{31,f}$ is mostly caused by the substrate clamping effect. As mentioned in Sections 3.1 and 3.2, due to the tight clamping of the PZT film by rigid substrates, only the effective piezoelectric coefficients are measured, and they are related to the (true) piezoelectric coefficients of ceramics by Equations 3.1 and 3.17. From Equation 3.1 and 3.17, we have, after taking differentiation:

$$\Delta d_{33}^{'} = \Delta d_{33} - \frac{2(s_{13}^{E}\Delta d_{31} + d_{31}\Delta s_{13}^{E})}{s_{11}^{E} + s_{12}^{E}} - \frac{2s_{13}^{E}d_{31}(\Delta s_{11}^{E} + \Delta s_{12}^{E})}{(s_{11}^{E} + s_{12}^{E})^{2}} \qquad (3.34)$$

$$\Delta e_{31,f} = \frac{\Delta d_{31}}{s_{11}^E + s_{12}^E} - \frac{d_{31}(\Delta s_{11}^E + \Delta s_{12}^E)}{(s_{11}^E + s_{12}^E)^2} \quad (3.35)$$

It is clearly seen that the actual changes in $d_{33}^{'}$ and $e_{31,f}$ ($\Delta d_{33}^{'}$ and $\Delta e_{31,f}$) of the PZT films after the doping of Nb are dependent not only on the changes in d_{33} and d_{31} (Δd_{33} and Δd_{31}), but also on the changes in s_{11}^E, s_{12}^E and s_{13}^E (Δs_{11}^E, Δs_{12}^E and Δs_{13}^E). The calculation has shown that if all the material parameters are set to increase by the same amount (in percentage), $d_{33}^{'}$ increases also by the same percentage but $e_{31,f}$ remains unchanged (i.e. $\Delta e_{31,f} = 0$). However, if only d_{33}, d_{31} and s_{13}^E are set to increase by, for example, 50% while Δs_{11}^E and Δs_{12}^E are set to zero, then $d_{33}^{'}$ decreases by 25% but $e_{31,f}$ increases by 50%.

It has been shown that the donor-type dopant can increase not only the piezoelectric properties, but also the elastic compliances of PZT bulk ceramics. Table 3.1 shows the material parameters of $Pb(Zr_{0.52}Ti_{0.48})O_3$ and $Pb_{0.988}(Zr_{0.52}Ti_{0.48})_{0.976}Nb_{0.024}O_3$ bulk ceramics [Jaffe, B. *et al.*, 1971]. It is seen that the material parameters have different increments (in percentage) after the doping of Nb. Using Equation 3.1 and 3.17 and the material parameters listed in Table 3.1, $d_{33}^{'}$ and $e_{31,f}$ of the ceramics in thin-film form (deposited on rigid substrates) are calculated, giving the results listed in Table 3.2. It can be seen that the increment in $d_{33}^{'}$ after the doping of Nb is greatly suppressed to 25% as

compared to that in d_{33} (60%), while the change in $e_{31,f}$ still remains large (67%). This implies that d'_{33} is not very sensitive to the Nb-dopant effect, and is consistent with our experimental results showing that the change in the observed $e_{31,f}$ is much larger than that in d'_{33}.

Table 3.1 Material parameters of PZT and Nb-doped PZT bulk ceramics [Jaffe, B. *et al.*, 1971].

	$Pb(Zr_{0.52}Ti_{0.48})O_3$	$Pb_{0.988}(Zr_{0.52}Ti_{0.48})_{0.976}Nb_{0.024}O_3$
d_{33} (pm/V)	223	374
$-d_{31}$ (pm/V)	93.5	171
s_{11}^E (10^{-12} m²/N)	13.8	16.4
s_{12}^E (10^{-12} m²/N)	-4.07	-5.74
s_{13}^E (10^{-12} m²/N)	-5.80	-7.22

Table 3.2 Calculated effective piezoelectric coefficients d'_{33} and $e_{31,f}$ of PZT and Nb-doped PZT bulk ceramics (in the form of thin film).

	d'_{33} (pm/V)	$e_{31,f}$ (pC/N)
$Pb(Zr_{0.52}Ti_{0.48})O_3$ ceramic	112	9.6
$Pb_{0.988}(Zr_{0.52}Ti_{0.48})_{0.976}Nb_{0.024}O_3$ ceramic	142	16

Chapter Four

Fabrication of Silicon-based Membranes

As mentioned in Chapter 1, micromachined silicon-based membranes with PZT films as active elements are of significant interest for actuator applications. It has been shown in Chapter 3 that the 1% Nb-doped PZT film has better piezoelectric properties than the others. Hence, it has been used to fabricate micromachined membranes in this project. The micro-fabrication process for the membranes is described in this chapter.

4.1 Fabrication of silicon-based membranes

A double-side polished substrate $Pt/Ti/SiO_2/Si/Si_3N_4$ of thickness = 425 μm was used in the fabrication of the silicon-based membranes. Figure 4.1 shows the main processing steps.

(a) A layer of positive photoresist (AZ 3100, Clariant) was spun on the surface of Si_3N_4 (labeled as the backside) by a spinner (KW-4A, Chemat Technology). Two different rotation speeds were used for different periods in the process. First, a low speed of 800 rpm was used for 6 seconds to spread the photoresist over the whole surface of the substrate. Then a high speed of 4500 rpm was used for 50 seconds to obtain a thin layer of film with uniform thickness. The photoresist was then dried in an oven (Memmert) at 80°C for 10 min. The thickness of the

photoresist is about 1.2 μm. After that, a square pattern (Figure 4.2 (a)) was transferred to the surface of the photoresist using an optical aligner. The sample (with the photoresist faced upwards) was covered tightly by a dark-field photomask and then exposed to UV light for 20 s. After that, a developer (AZ 300 MIF, Clariant) was used to develop the pattern (the exposed photoresist). The sample was shaken for about 40 s in the developer and rinsed with deionized water for about 30 s. Then a square opening was formed in the photoresist, which was used as a window for the removal of the silicon substrate.

(b) The photoresist was used as the mask for etching the silicon nitride Si_3N_4. An inductively coupled plasma etcher (ICP, Microelectronics R&D Center, Chinese Academy of Sciences) was used to etch the thin layer of Si_3N_4. The dry etching condition is shown in Table 4.1.

(c) After the etching of Si_3N_4, the remaining photoresist was removed by using acetone and ethanol. A PZT/PT film was then deposited on the surface of the platinum electrode by the sol-gel technique, following the fabrication processes and conditions described in Chapter 2.

(d) Two thin layers of strontium titanate $SrTiO_3$ (STO) were deposited on the surface of the PZT film by rf-magnetron sputtering. They were located on opposite sides of the backside window. A $SrTiO_3$ ceramics disc (Superconductive Components, Inc., purity 99.9%) of diameter 50.8 mm and thickness 3 mm was used as the sputtering target. The condition for the deposition is shown in Table

4.2. After the deposition, the sample was annealed in a rapid thermal processor at 550°C for 30 min in an oxygen atmosphere. The function of the STO films is to reduce the piezoelectric responses arising from the PZT film region under the electrode pad and connecting wire (to be deposited in the next step). Since the relative permittivity of STO is lower than that of the PZT film (about 300), this region of the film will not be effectively poled during the poling of the film region on the membrane. As a result, they will not response well to the external signals, and hence the influence to the performance of the membrane is minimized.

After that, a thin layer of gold (Ag)/chromium (Cr) was deposited by dc sputtering. Metal gold and chromium discs (Kurt J. Lesker, purity 99.99%) of diameter 50.8 mm and thickness 3 mm were used as the sputtering targets. The condition for the deposition is also shown in Table 4.2.

(e) A thin layer of photoresist was applied on the top surface of the sample, and then a pattern of the top electrode for the membrane structure (Figure 4.2 (b)) was transferred to it, following the procedures described in step (a). The resulting pattern of photoresist was used as a mask to etch away the gold and chromium layers for forming the pattern of the electrode. Gold and chromium were etched using the etching solutions of which the compositions are shown in Table 4.3. Firstly, the gold was etched in the gold etchant for 12 s and then rinsed with deionized water for about 30 s. Then, the chromium was etched in the chromium etchant for 15 s. The pattern of the gold/chromium electrode was formed. The remaining photoresist was removed by oxygen plasma which can remove organic

contamination easily.

(f) The silicon unprotected by Si_3N_4 was removed from the backside using the potassium hydroxide (KOH) etching solution (of which the composition is shown in Table 4.3). To protect the other region of the sample from etching, the sample was placed inside of a chuck (Figure 4.3). Before the backside etching, a 1.2-μm thick photoresist layer was spun on the top surface of the sample and dried at 80 °C for 10 min. in an oven. This layer of photoresist acts as a cushion between the sample and the inner surface of the chunk, such that the electrode pattern will not be damaged. After the chuck has been sealed, it was immersed in the KOH etching solution at 70°C for 8 hours. After that, the chuck was taken out and rinsed with water for 5 min. The etching rate of silicon using a 43 wt.% KOH solution at 70 °C is about 0.71 μm/min. So the thickness of the remaining silicon is about 80 μm. The photograph of the silicon-based membrane is shown in Figure 4.4 (a) and (b).

Side View | Top View

Pt/Ti (120 nm)
SiO_2
Si (425μm)
Si_3N_4 (400 nm)
Photoresist (~1.2 μm)
Step (a)
(Backside) Si_3N_4 Photoresist

Pt/Ti
SiO_2
Si
Si_3N_4
Photoresist
Step (b)
Pt/Ti

PT seeding layer (~ 100 nm)
PZT (~ 800 nm)
Pt/Ti
SiO_2
Si
Si_3N_4
Step (c)
PZT

Au/Cr (~140 nm)
STO (~50 nm)
PT seeding layer
PZT
Pt/Ti
SiO_2
Si
Si_3N_4
Step (d)
Au/Cr

Au/Cr
STO
PT seeding layer
PZT
Pt/Ti
SiO_2
Si
Si_3N_4
Step (e)
Au/Cr PZT STO

Au/Cr
STO
PT seeding layer
PZT
Pt/Ti
SiO_2
Si
Si_3N_4
thickness of Si ~ 80 μm
Step (f)
Au/Cr PZT STO

Figure 4.1 The main process flow for the fabrication of silicon-based membranes.

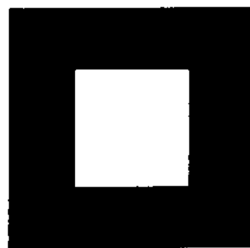

Backisde window (a)

Pattern of electrode (b)

Figure 4.2 (a) The pattern of backside window
(b) the pattern of electrode on the photomask.

Table 4.1 The operating condition for etching silicon nitride Si_3N_4 using an ICP etcher.

Material	Si_3N_4
Main feed gas (sccm)	SF_6/Ar (25/5)
Base pressure (Pa)	2 x 10^{-2}
Operation pressure (Pa)	4
RF Power (Watt)	80
Etch time (min)	3
Etch rate (nm/min)	133

Table 4.2 The conditions for the deposition of STO and Au/Cr.

Target	STO	Au/Cr
Main feed gas (sccm)	Ar/O_2 (5/5)	Ar (10)
Base vacuum (Torr)	8×10^{-5}	8×10^{-5}
Operation vacuum (Torr)	7×10^{-3}	7×10^{-3}
Power (Watt)	80	70/70
Deposition time (min)	30	5 / 3
Thickness (nm)	50	140

Table 4.3 Etchants for removing Si, Au and Cr layers.

Etchant	Chemical Formula	Materials	Temperature
43 wt.% KOH	75.4g KOH + 100ml H_2O	Si	70°C
Au etch	4g KI + 1g I_2 + 80ml H_2O	Au	Room temp
Cr etch	200g $Ce(NH_4)_2(NO_3)_6$ + 35ml CH_3COOH 98% + 1000ml H_2O	Cr	Room temp

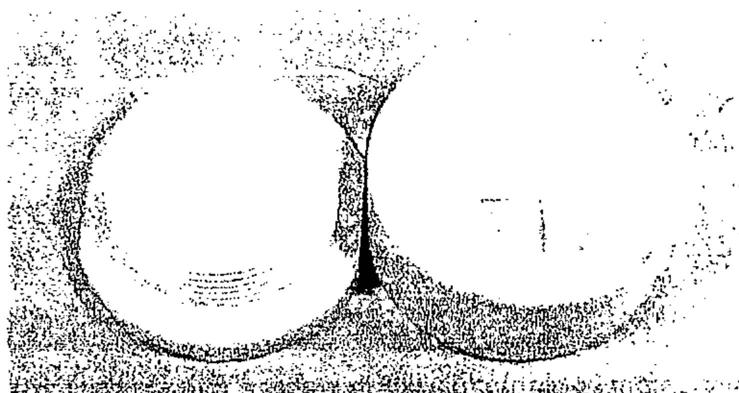

Figure 4.3 The mechanical chuck used in the KOH wet etching.

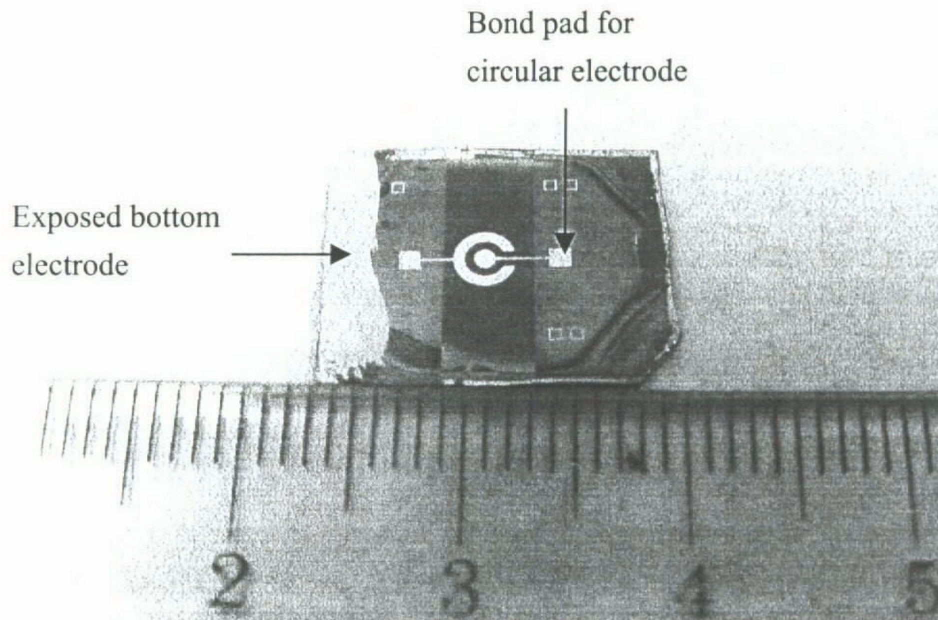

Figure 4.4 (a) The top view of the silicon-based membrane.

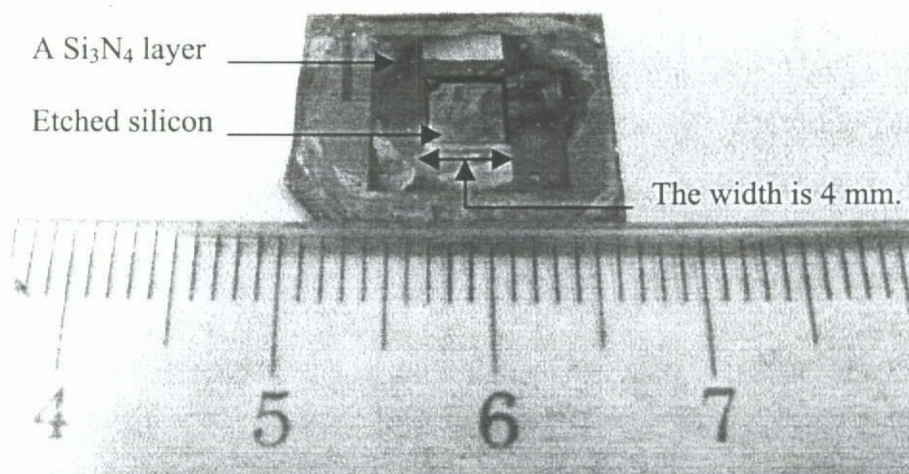

Figure 4.4 (b) The backside window of the silicon-based membrane.

Chapter Five

Evaluation of Silicon-based Membranes

The 1% Nb-doped PZT films have been fabricated into micromachined membranes, and their performance are evaluated in this chapter. Membranes of two dimensions are fabricated: 3 mm × 3 mm × 80 μm and 4 mm × 4 mm × 80 μm. For each membrane, the thickness of the Nb-doped PZT film is 800 nm. At last, the performance of the membrane as an acoustic sensor has been roughly and qualitatively evaluated.

Before the characterization, the membranes (the film regions under the circular electrode, refer to Figure 4.4 (a)) was fully poled under a dc field of 20 MV/m for 5 min. For the poling, the positive terminal of the dc source was connected to the bond pad for the circular electrode on the PZT film (Figure 4.4 (a)). The exposed bottom electrode was grounded. After the poling, the membrane was short-circuited for 10 minutes.

5.1 Resonance frequency of the silicon-based membranes

In this section, the resonance frequency of the membranes are examined and compared with the theoretical prediction. An impedance analyzer (HP 4194A, Hewlett Packard) was used to measure the impedance and phase as functions of

Pao Yue-kong Library
PolyU • Hong Kong

frequency. Figures 5.1 and 5.2 show the impedance spectra of the membranes measured on the circular electrode. For each membrane, a weak resonance peak is observed. The observed resonance frequency for the 3-mm square membrane is about 111.5 kHz, while that of the 4-mm square membrane is 65 kHz. These resonance peaks should be associated with the fundamental resonance mode of the square membrane, arising from the vibrating up and down motion. For a poled PZT film (the region under the circular electrode) subjected to an applied ac field, it will expand and contract along the thickness direction, because of the piezoelectric effect. Due to the Poisson effect, lateral stresses are induced in the PZT film (which is clamped by the substrate) and then applied on the substrate. Since the membrane is of a free-standing structure, these lateral stresses will cause the membrane to vibrate sinusoidally, following the same frequency of the driving field. If the frequency of the ac field and the natural frequency of the square membrane are the same, resonance takes place and the vibrating amplitude of the membrane becomes the largest. At this moment, the dimensional change of the film (the region under the circular electrode) also becomes the largest, thus giving rise a change in the observed impedance. It is quite obvious that the natural frequency and hence the resonance frequency of a square membrane decrease with increasing the length (or decreasing the thickness) of the free-standing structure..

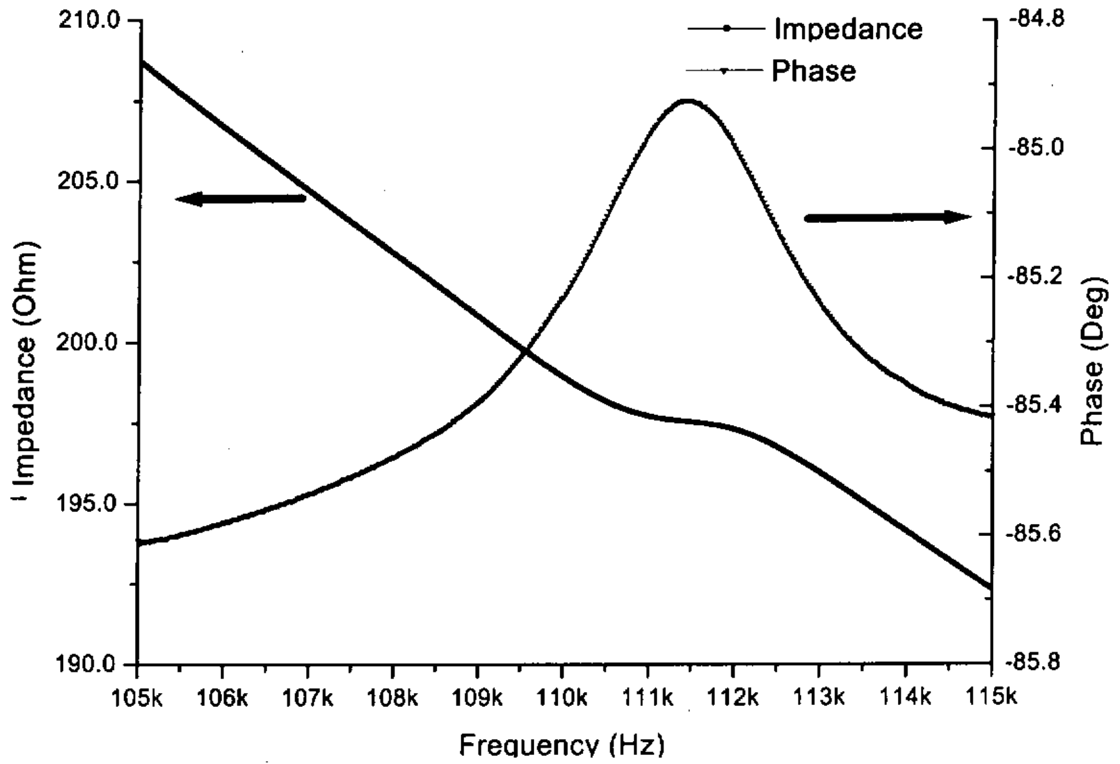

Figure 5.1 Impedance spectra for the 3 mm × 3 mm × 80 μm silicon-based membrane.

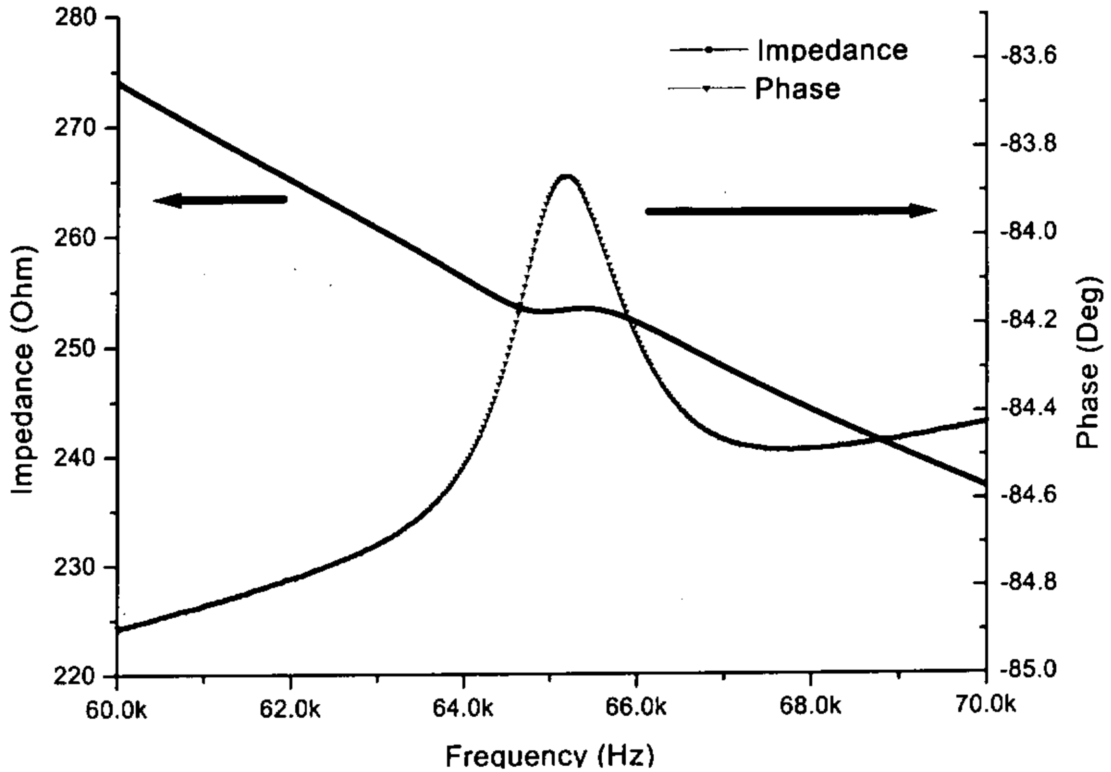

Figure 5.2 Impedance spectra for the 4 mm × 4 mm × 80 μm silicon-based membrane.

For a square membrane, the natural frequency for the fundamental mode is given as [Setter, N. chapter 13, 2002]:

$$f = 1.654\frac{t}{L^2}\sqrt{\frac{Y}{\rho(1-\nu^2)}} \tag{5.1}$$

where t and L are the thickness and length of the membrane, respectively; Y, ρ and ν are the Young's modulus, density and Poisson ratio of the substrate material, respectively. The parameters used for the calculation are listed in Table 5.1. The thickness of the membranes (or Si substrate) was 80 μm, determined from a control sample which has been wet-etched in the KOH etching solution together with the sample for the same period. The calculated resonance frequencies for the 3-mm

and 4-mm square membranes are 123 kHz and 69 kHz, respectively. This is consistent with the observation that the resonance frequency decreases as the length of the membrane increases. However, the calculated frequencies are about 10% higher as compared to the observed resonance frequencies from the impendence spectra. This may be partly due to the residual stresses in substrate [*Defaÿ* E. *et al.*, 2002] and partly due to the error in the substrate thickness.

Table 5.1 The variables of the silicon (100) oriented [Setter, N. chapter 13, 2002].

Young modulus Y	Density ρ	Poisson ratio ν
169×10^{9}	2.5×10^{3}	0.172

5.2 Surface displacement of the silicon-based membranes

A Mach-Zehnder type heterodyne (single beam) laser interferometer (SH-120, B.M. Industries, France) was used to measure the surface displacement of the membranes. The experimental setup is shown in Figure 3.1. A function generator (HP 8116A, Hewlett Packard) was used to apply an ac field across the membrane (the PZT film region under the circular electrode).

Similar to the procedures mentioned in Chapter 3, the whole wafer (on which the membrane is formed) was glued tightly on a large piece of PCB using a mounting wax (Figure 5.5). As discussed in Chapter 3, this is an effective method

for suppressing the bending of the whole wafer.

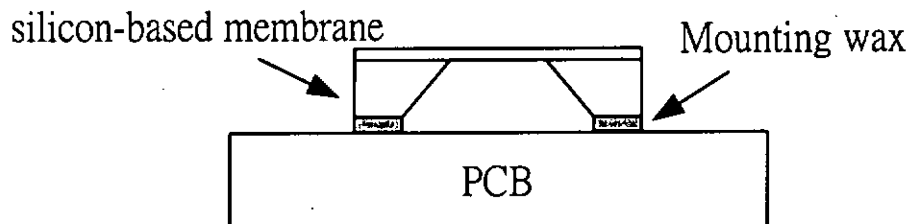

Figure 5.3 Sample fixture for measuring the surface displacement of the silicon-based membranes.

Figure 5.4 shows the surface displacement at the center of the membrane as a funtion of applied ac voltage for the 3-mm and 4-mm square membranes, respectively. The frequency of the ac voltage is 15 kHz, and the amplitude ranges from 0.1 V to 0.7 V (or 0.125 MV/m to 0.875 MV/m). It is seen that, for each membrane, the surface displacement increases quite linearly with increasing voltage. In agreement with the expectation, the surface displacement of the square membrane increases as the length of the membrane increases. The average displacements per unit voltage of the 3-mm and 4-mm membranes (of thickness ~ 80 μm) are about 6.8 nm/V and 10.5 nm/V, respectively, which are much larger than that of a 3 mm × 3 mm × 0.003 mm membrane with a 0.5-μm thick zine oxide piezoelectric active element (2.5 nm/V) [Ko *et al.*, 2003]. It is quite clear that the displacement of the silicon-based membrane can be effectively increased by decreasing the thickness of the membrane (i.e. silicon substrate).

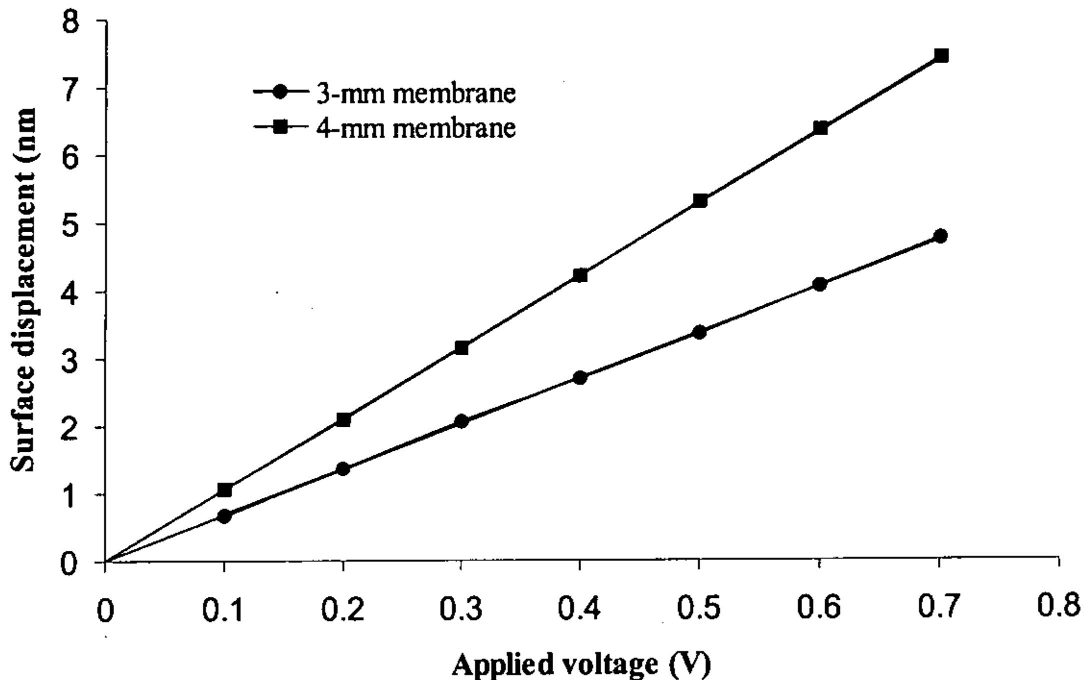

Figure 5.4 Variation of the surface displacement with applied voltage for the 3-mm and 4-mm silicon-based membranes.

Figures 5.5 and 5.6 show the surface displacement at the center of the membrane as a function of dc bias voltage for the 3-mm and 4-mm square membranes, respectively. The frequency of the driving ac voltage is 15 kHz and the amplitude is 0.1 V. The dc bias voltage increases from 0 V to 15 V (solid square symbol), then decreases from 15 V to -15V (open square symbol), and finally increases from -15 V to 15 V (solid circle symbol). Similar to the poling procedures, the positive terminal of the dc bias voltage was connected to the bond pad for the circular electrode on the PZT film (Figure 4.4 (a)). First of all, it can be seen that the surface displacement for both membranes increases as the bias voltage increases from 0 V to 15 V; and the change of the displacement is quite reversible, without any hysteresis, as the bias voltage decreases back to 0 V. At

the largest bias voltage (15 V), the surface displacement for the 3-mm and 4-mm membranes are increased by about 41% and 52 % to 0.89 nm and 1.38 nm, respectively.

Typical butterfly-shaped loops, but laterally shifted toward the negative side of the voltage axis, are observed for the displacement of both square membranes as the bias voltage decreases from 15 V to -15 V and then increases back to 15 V (Figures 5.5 and 5.6). The loops clearly show the switching of the resultant polarization in the films by the bias voltage, and are typical characteristic for ferroelectric materials. The observed polarization reveral voltages are around 1 V and -5 V for the 3-mm membrane, and 1 V and -3 V for the 4-mm membrane, indicating that there are internal bias voltages of about -2 V and -1 V in the 1% Nb-doped PZT films. The large discrepancy in the observed internal bias voltages is mostly likely due to the corase increment of the bias voltage in the measurement. In consistent with the previous work on the sol-gel derived films [Kwok, K. W. *et al.*, 2002; Wang, B. *et al.*, 2003], the internal bias voltage (or field) points towards the bottom electrode (since the bias voltage was applied on the top electrode). It was suggested that the internal bias voltage was induced by the high-energy ion bombardment on the film during the sputtering deposition of the top electrode. Because of the internal bias voltage, the actual bias voltage in the film becomes larger in the positive side of the voltage axis, and becomes smaller in the negative side of the voltage axis. For this reason, the observed surface displacement at negative bias voltages is smaller than that at positive bias voltages for both membranes.

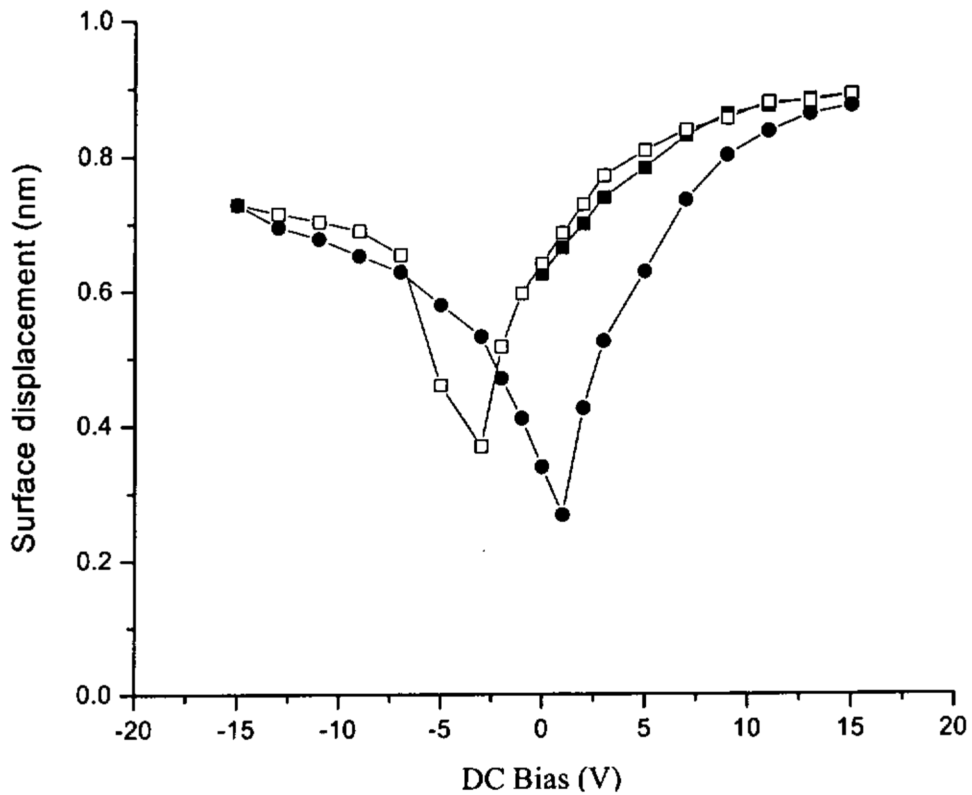

Figure 5.5 Surface displacement at the center of the membrane as a function of dc bias voltage for the 3-mm square membranes. The dc bias voltage increases from 0 V to 15 V (solid square symbol), then decreases from 15 V to -15V (open square symbol), and finally increases from -15 V to 15 V (solid circle symbol).

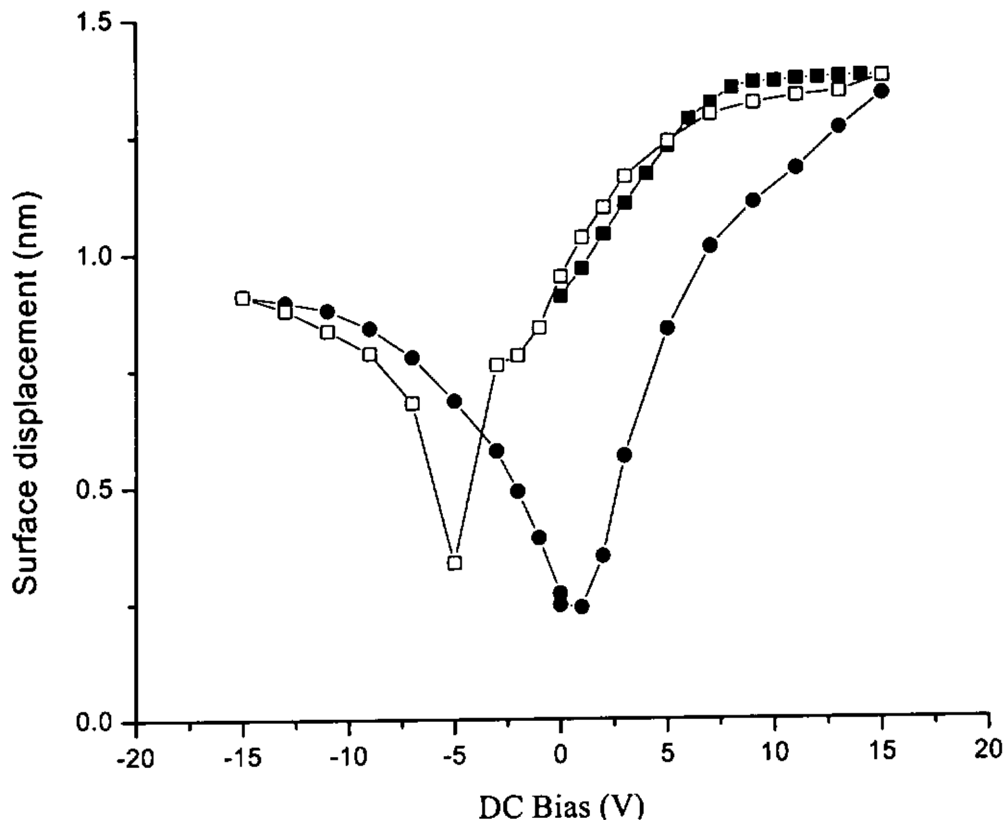

Figure 5.6 Surface displacement at the center of the membrane as a function of dc bias voltage for the 4-mm square membranes. The dc bias voltage increases from 0 V to 15 V (solid square symbol), then decreases from 15 V to -15V (open square symbol), and finally increases from -15 V to 15 V (solid circle symbol).

Figures 5.7 and 5.8 show the surface displacement at the center of the membrane as a function of frequency for the 3-mm and 4-mm square membranes, respectively. The amplitude of the driving ac voltage is 0.1 V. For each membrane, the surface displacement increases slightly with increasing frequency

first, and then increases sharply to reach a maximum value at a resonance frequency. The observed resonance frequencies for the 3-mm and 4-mm membranes are 109 kHz and 65 kHz, while the maximum surface displacements are about 20 nm and 90 nm, respectively. As expected, as the length of a square membrane increases, the resonance frequency decreases while the surface displacement increases. The observed resonance freuqencies are very close to those observed from the dielectric measurement (Figures 5.1 and 5.2). At resonance, the displacement per unit voltage of the 3-mm and 4-mm silicon-based membranes are about 200 nm/V and 900 nm/V, which are much higher than that of the zine oxide membrane mentioned above (70 nm/V) [Ko *et al.*, 2003].

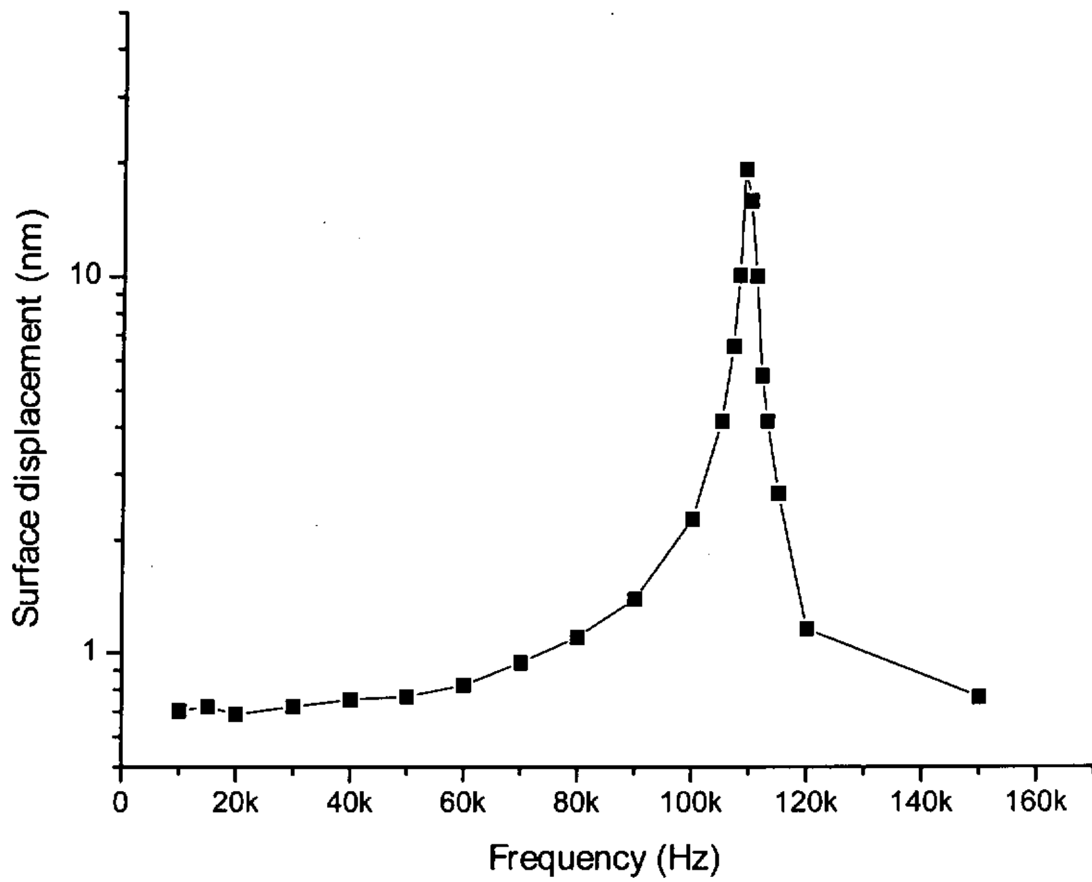

Figure 5.7 Surface displacement at the center of the 3 mm × 3 mm × 80 μm silicon-based membrane as a function of frequency. The amplitude of the driving voltage is 0.1 V.

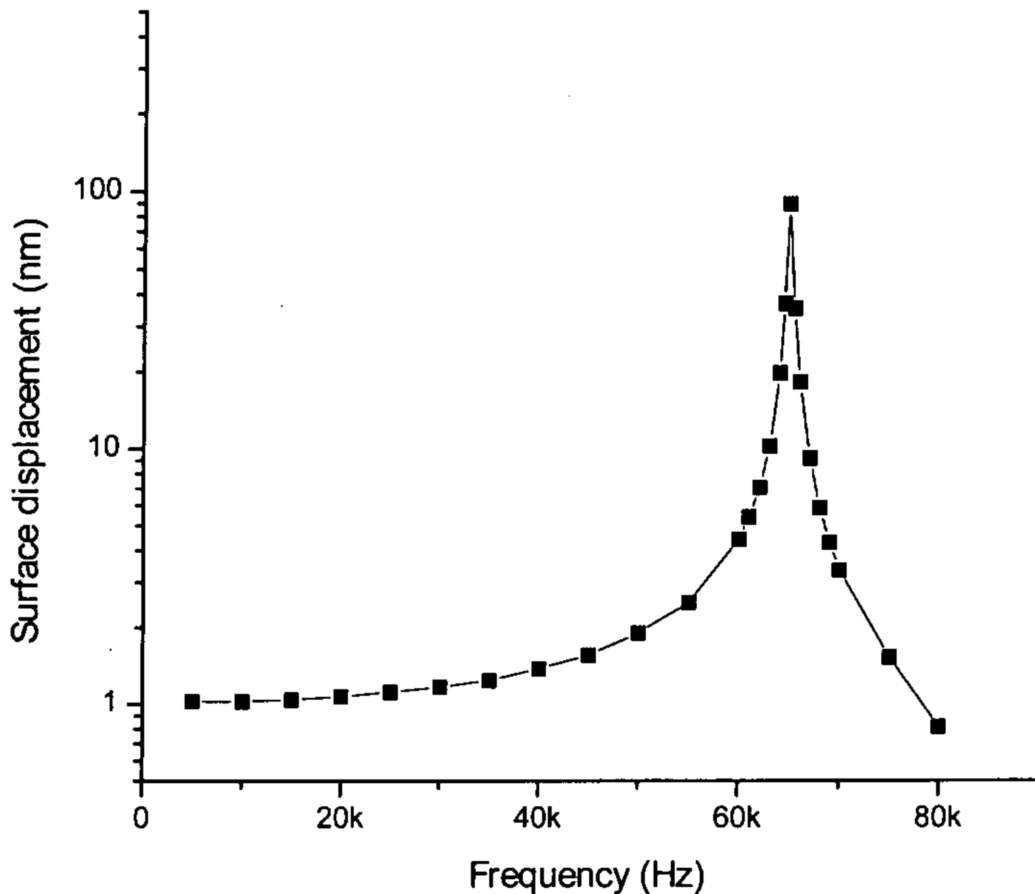

Figure 5.8 Surface displacement at the center of the 4 mm × 4 mm × 80 μm silicon-based membrane as a function of frequency. The amplitude of the driving voltage is 0.1 V.

5.3 Signal capture by the silicon-based membrane

Since the 1% Nb-doped PZT film has a very large $e_{31,f}$ value, about 12.8 C/m^2, it is also of interest in assessing the performance of the silicon-based membranes as an acoustic sensor. In this section, only a rough and qualitative evaluation was carried out. The experimental setup for the measurement is shown in Figure 5.9. A moderate sound was generated about 3 cm above the membrane. The signal generated by the membrane was recorded directly by a digital storage oscilloscope;

no filter and amplifier were used. Figures 5.10 and 5.11 show the signal captured by the 3-mm and 4-mm membranes, respectively. It can be seen that the signals for both membranes is considerably large. For the 4-mm membrane, the largest signal is about 180 mV. These indicate that the silicon-based membranes are also suitable for use in acoustic sensor applications.

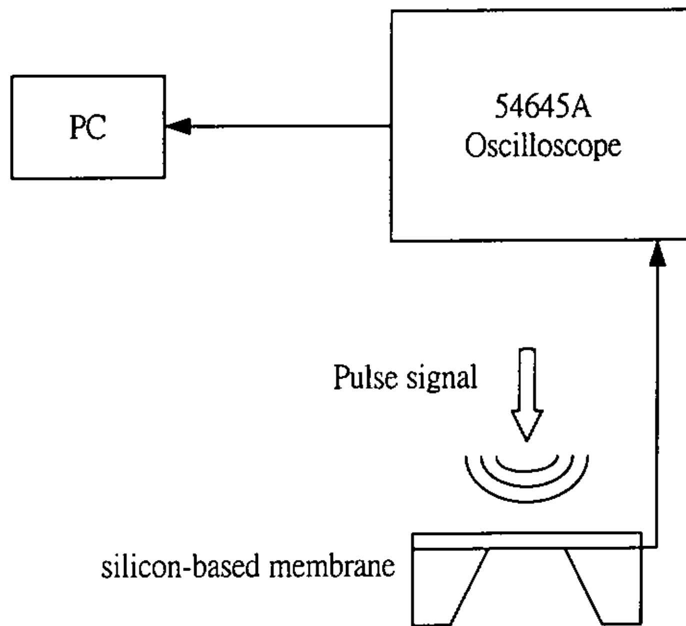

Figure 5.9 The experimental setup for the measurement of the output voltage of the membranes.

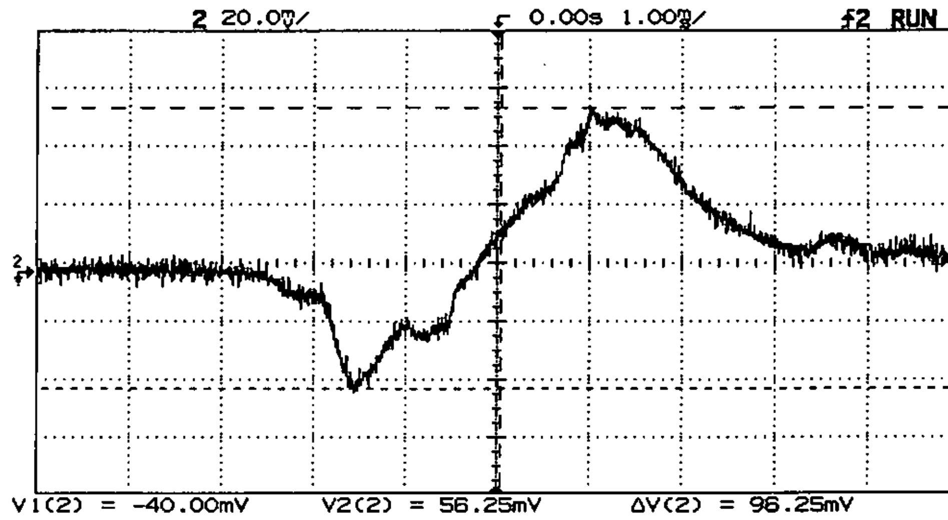

Figure 5.10 The output voltage signal by the 3-mm membrane.

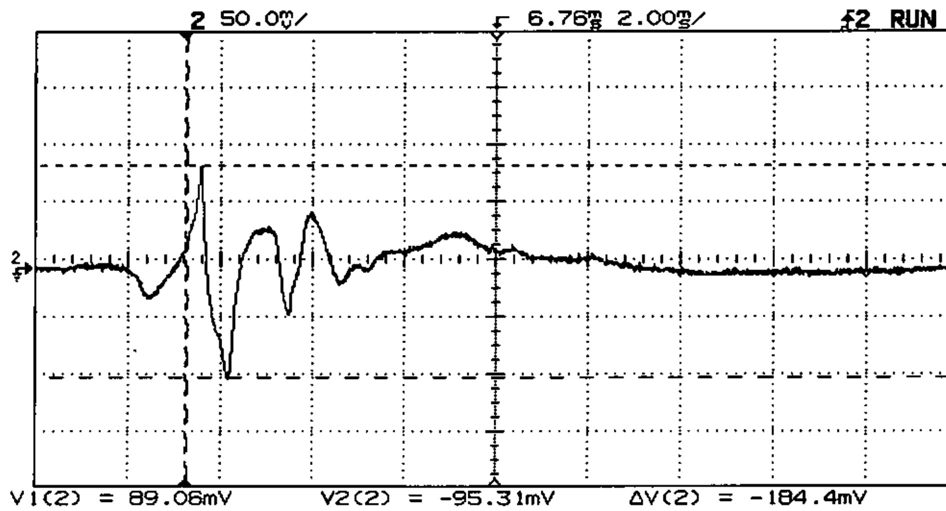

Figure 5.11 The output voltage signal by the 4-mm membrane.

Chapter Six
Conclusions

The main objectives of the present work are to prepare sol-gel derived Nb-doped PZT films, to study the effects of Nb dopant on the piezoelectric properties of the PZT films, and to evaluate the PZT films for micromachined membrane-actuator applications.

In order to lower the annealing temperature and hence to eliminate diffusion at the interface, a PT seeding layer of thickness 100 nm has been introduced between the Nb-doped PZT film and the Pt bottom electrode. The Zr/Ti ratio of the films was 53/47. Both the PT seeding layer and Nb-doped PZT films were prepared by the sol-gel method together with the multiple-spin-coating technique. PZT films with 0%, 1% and 2% Nb dopant and a thickness of 800 nm have been successfully deposited on silicon substrates at a low annealing temperature of 550°C. All the films are well-crystallized into the perovskite phase and contain no pyrochlore or PbO_x phases. They are dense and crack-free, and have good dielectric and piezoelectric properties.

Effective longitudinal and transverse piezoelectric coefficients ($d_{33}^{'}$ and $e_{31,f}$) of the films have been measured using a single beam laser interferometer and a newly established method based on the direct piezoelectric effect, respectively. For the $d_{33}^{'}$ measurement, the substrate bending, which usually induces an

enormous error in the measurement, has been effectively suppressed by gluing the sample (film/substrate) on a large and rigid platform with mounting wax. In the $e_{31,f}$ measurement, a rectangular sample (film/substrate) was bent dynamically to create a longitudinal stress along the length of the film sample. The current induced on the top electrode was measured using a lock-in amplifier. The $e_{31,f}$ value was then determined from the linear relation between the sample deflection and the induced current.

The effects of Nb dopant on the longitudinal and transverse piezoelectric coefficients of the PZT films have been studied. For the un-doped PZT film, the observed d_{33}' and $e_{31,f}$ values are about 68 pm/V and 9.9 C/m^2, respectively. Similar to the effects observed in the corresponding PZT bulk ceramics, the Nb dopant enhances the piezoelectric properties of the sol-gel derived PZT films, showing an optimum doping level of 1 %. At this optimum doping level, the observed d_{33}' and $e_{31,f}$ values of the film are increased, by about 9% and 30%, to 74 pm/V and 12.8 C/m^2, respectively. It is suggested that the apparent difference in the enhancement of d_{33}' and $e_{31,f}$ (9% and 30%) is mainly caused by the substrate clamping effect.

The 1 % Nb-doped PZT film has been fabricated into square micromachined membranes, and their performance have been evaluated. The lengths of the square membranes are 3 mm and 4 mm, respectively, while the thickness of the membranes (including the film and silicon substrate) is about 80 μm. The observed

fundamental resonance frequencies for the 3-mm and 4-mm membranes are 111.5 kHz and 65 kHz, respectively. The observed resonance frequencies as well as its dependence on the length of the membrane agree with the theoretical calculation. At resonance, the vibrating displacements at the center of the membranes have the maximum values of 200 nm/V and 900 nm/V for the 3-mm and 4-mm membranes, respectively. At frequencies below the resonance frequency, the displacements are about 6.8 nm/V and 10.5 nm/V, respectively, and can be increased reversibly by about 40-50% under a dc bias field of 16 MV/m. These indicate that the silicon-based membranes are suitable for actuator applications. At last, the performance of the silicon-based membranes as an acoustic sensor has also been evaluated qualitatively. Because of the large $e_{31,f}$ value, the signals induced by the membrane subjected to a moderate sound, without using any preamplifier, is considerably high, having a maximum value of about 200 mV for the 4-mm membrane. This indicates that the silicon-based membrane is also suitable for acoustic sensor applications.

References

Abe, H., Y. Sonobe, and T. Enomoto, "Etching characteristics of silicon and its compounds by gas plasma", *Japanese Journal of Applied Physics,* Vol. 12, pp. 154-155 (1973)

Aoki, K., Y. Fukuda, K. Numata and A. Nishimura, "Effects of titanmium buffer layer on PZT crystallization process in sol-gel deposition technique" *Japanese Journal of Applied Physics* Vol. 34, pp. 192-195 (1995)

Auld, B. A., *Acoustic Fields and Waves in Solids* 2nd edition, Vol. 1, Krieger Publishing Co. Malabar, Florida, U. S. A., (1990).

Barrow, D. A., T. E. Petroff, R. P. Tandon and M. Sayer, "Characterization of Thick Lead Zirconate Titanate Films Fabricated Using a New Sol Gel Based Process", *Journal of Applied Physics* Vol. 81 (2), pp. 876-881 (1997).

Brantley, W. A. "Calculated Elastic Constants for Stress Problems Associated with Semiconductor Devices", *Journal of Applied Physics*, Vol. 44, pp. 534-535 (1973).

Chapman, B., *Glow Discharge Processes*, John Wily & Sons, chapter 4, pp. 77-133 (1980)

Chapman, B., *Glow Discharge Processes*, John Wily & Sons, chapter 5, pp. 139-173 (1980)

Chen, K. C., and J. D. Mackenzie, *Mat. Res. Symp. Proc. 180*, pp. 663-668 (1990)

Damjanovic, D., "Ferroelectric, Dielectric and Piezoelectric Properties of Ferroelectric Thin Films and Ceramics", *Reports on Progress in Physics*, Vol. 61, pp. 1267–1324 (1998).

DeForest, W. S. "Photoresist Materials and Processes." *McGraw-Hill, New York*, (1975)

Defaÿ, E., C. Millon, C. Malhaire, D. Barbier, "PZT thin films integration for the realization of a high sensitivity pressure microsensor based on a vibrating membrane", Sensors and Actuators, Vol. 99, pp.64-67 (2002)

Dubois, M. A., and P. Muralt, "Measurement of the Effective Transverse Piezoelectric Coefficient $e_{31,f}$ of AlN and $Pb(Zr_x,Ti_{1-x})O_3$ Thin Films", *Sensors and Actuators*, Vol. 77, pp. 106-112 (1999).

Dubois, M. A., and P. Muralt, "BAW resonators based on aluminum nitride thin films", *IEEE Ultrasonic Symposium*, Vol. 2, pp. 907-910 (1999)

El-Karch, *Fundamentals of Semiconductor Processing Technologies*, Kluwer Academic Publishers, chapter 4 (1995)

Feynman, R. P., "There's Plenty of Room at the Bottom," presented at the American Physical Meeting in Pasadena, CA, December, 1959; reprinted with permission of Van Nostrand Reinhold in *J. Microelectromechanical Systems*, Vol. 2, pp. 60-66 (1992)

Feynman, R. P., "Infinitesimal Machinery," presented at the Jet Propulsion Laboratory on February 23, 1983; reprinted in *J. Microelectromechanical Systems*, Vol. 2, pp. 4-14 (1993)

Fukumoto, A. "The application of piezoelectric of piezoelectric ceramics in diagnostic ultrasonic transducers", *Ferroelectrics* Vol. 40, pp. 217-230 (1982)

Grove, W. R., Philos. Trans Roy. Soc. London 142, 87 (1852)

Guo, R., L.E. Cross, S. E. Park, B. Noheda, D.E. Cox, and G. Shirane, "Origin of the high piezoelectric response in $PbZr_{1-x}Ti_xO_3$", Physical Review Letters, Vol. 84, pp. 5423 –5426 (2000)

Ikeda, T., *Fundamental of Piezoelectricity* (Oxford) New York (1990).

Irving, S. M. Kodak Interface Proc. 2, 26 (1968)

Irving, S. M. "A plasma oxidation process for removing photoresist films", *Solid State Technology*, Vol. 14, pp. 47-51 (1971)

Ishikawa, K., K. Sakura, D. Fu, S. Yamada, H. Suzuki and T. Hayashi, "Effect of $PbTiO_3$ Seeding Layer on the Growth of Sol-Gel-Derived $Pb(Zr_{53}Ti_{47})O_3$ Thin Film", *Japanese Journal of Applied Physics*, Vol. 37, pp. 5128-5131 (1998)

Jaffe, B., R. S. Roth, and S. Marzullo, *Journal of Applied Physics*, Vol. 25, pp. 809-810 (1954).

Jaffe, B., Cook, and H. Jaffe, *Piezoelectric Ceramics*, (Academic, New York) (1971).

Jaffe, B., P. S. Roth, and S. Marzullo, "Properties of Piezoelectric Ceramics in the Solid-Solid Series Lead Titanate-Lead Zirconate-Lead Oxide: Tin Oxide and Lead Titanate-Lead Hafnate", *Journal of Research of the National Bureau of Standards*, Vol. 55, pp.239-254 (1955)

Kirshnawary, S. V., J. F. Rosenbaum, S. S. Horwitz, and R. A. Moore, "Film bulk acoustic wave resonator technology," in *Proc. IEEE Ultrason. Symp.*, Vol. 1, pp. 529–536 (1990)

Klein, L.C., "Sol-gel processing of silicates", Annual review of materials science, Vol. 15, pp. 227-248 (1985)

Ko, S. C., Y. C. Kim, S. S. Lee, S. H. Choi; S. R. Kim, "Micromachined piezoelectric membrane acoustic device", *Sensors and Actuators A*, Vol. 103, pp. 130-134 (2003)

Kwok, C. K., and S. B. Desu, "Low temperature perovskite formation of lead zirconate titanate thin films by a seeding process", *Journal of Materials Research*, Vol. 8, pp. 339-344 (1993)

Kwok, K. W., B. Wang, H. L. W. Chan and C. L. Choy, "Self-Polarization in PZT Films", *Ferroelectrics*, Vol 271, pp. 69-74 (2002).

Lines, M. E., and A. M. Glass, *Principles and Applications of Ferroelectrics and Related Materials*, Oxford:Clarendon, (1979).

Maissel, L. I., and R. Glang, "Handbook of Thin Film Technology", *McGraw-Hill*, chapter 1, 1-26 (1970)

Maluf, N., *An Introduction to Microelectromechanical Systems Engineering*, Artech House, Inc., London, chapter 1, pp.1-13 (2000)

Maluf, N., *An Introduction to Microelectromechanical Systems Engineering*, Artech House, Inc., London, chapter 3, pp.41-83 (2000)

McCoy, J. H., W. Lee, and G. L. Varnell, "Optical Lithography Requirements in the Early 1990s," *Solid-state Technology*, 32 (3), pp. 87-92 (1989).

Muralt, P., T. Maeder, L. Sagalowicz, S. Hiboux, S. Scalese, D. Naumovic, R. G. Agostino, N. Xanthopoulos, H. J. Mathieu; L. Patthey, E. L. Bullock, "*Texture control of $PbTiO_3$ and $Pb(Zr,Ti)O_3$ thin films with TiO_2 seeding*", Journal of Applied Physics, Vol. 83, pp. 3835-3841 (1998)

Muralt, P., D. Schmitt, N. Ledermann, J. Baborowski, P. K. Weber, W. Steichen,; S. Petitgrand; A. Bosseboeuf, N. Setter, P. Gaucher, "Study of PZT coated membrane structures for micromachined ultrasonic transducers [medical imaging]", *2001 IEEE Ultrasonics Symposium. Proceedings*, Vol. 2, pp. 907 –911 (2001)

Noheda, B., J. A. Gonzalo, L. E. Cross, R. Guo, S. E. Park, D. E. Cox and G. Shirane, "A monoclinic ferroelectric phase in the $Pb(Zr_{1-x}Ti_x)O_3$ solid solution", *Applied Physics Letters*, Vol. 74, pp. 2059-61 (1999)

Roberts, S., *Physical Review*, Vol. 71, pp. 890 (1947)

Royer, D., V. Kmetik, " Measurement of Piezoelectric Constants Using an Optical Heterodyne Interferometer", *Electronics Letters*, Vol. 28, pp. 1828-1830 (1992).

Sawaguchi, E., *Journal of the Physical Society of Japan*, Vol. 8, pp. 615 (1953)

Seifert, A., L. Sagalowicz, P. Muralt, N. Setter, "Microstructural evolution of dense and porous $Pb_{1-x}Ca_xTiO_3$ thin films for pyroelectric applications, *Journal of Materials Research*, Vol. 14, pp. 2012-2022 (1999)

Senturia, S. D., "Feynman Revisited," *IEEE Micro Electro Mechanical Systems Workshop*, Oiso, Japan, Jan. 25-28, pp. 309-312 (1994)

Senturia, S. D., *Microsystems design.*, Boston: Kluwer Academic (2001)

Setter, N., *Piezoelectric Materials in Devices*, Ceramics Laboratory, EPFL Swiss Federal Institute of Technology, Lausanne 1015, Switzerland, chapter 1, pp. 8 (2002)

Setter, N., *Piezoelectric Materials in Devices*, Ceramics Laboratory, EPFL Swiss Federal Institute of Technology, Lausanne 1015, Switzerland, chapter 12, pp. 231-260 (2002)

Setter, N., Piezoelectric Materials in Devices, chapter 13, pp. 264-265 (2002)

Seyferth, D., G. H. Wiseman, *Ultrastructure Processing of Ceramics, Glasses and Composites*, edited by L. L. Hench and D. R. Ulrich, Wiley, New York pp. 265-271 (1984).

Smith, D. L., *Thin-Film Deposition*, McGraw-Hill, Inc., chapter 9.3.4, pp. 482-489 (1995)

Suzuki, H., T. Koizumi, Y. Kondo and S. Kaneko, " Low-temperature Processing of $Pb(Zr_{0.53}Ti_{0.47})O_3$ Thin Film from Stable Precursor Sol", *Journal of the European Ceramic Society,* Vol. 19, pp. 1397-1401 (1999)

Su, Q. X., P. Kirby, E. Komuro, M. Imura, Q. Zhang, R. Whatmore, "Thin-film bulk acoustic resonators and filters using ZnO and lead-zirconium-titanate thin films" *IEEE Transactions on*, Vol. 49, Issue: 4, pp. 769-778 (2001)

Tanaka, T. "Piezoelectric devices in Japan", *Ferroelectrics* Vol. 40, pp.167-187 (1982)

Timoshenko, S. P., J. N. Goodier, *Theory of Elasticity*, Third edition McGraw-Hill, Kogakusha, Tokyo, (1970).

Tsang, R. C. W., K. W. Kwok, H. L. W. Chan and C. L. Choy, "Piezoelectric Coefficients of PZT Thin Films", *Integrated Ferroelectrics*, Vol. 50, pp. 143-148 (2002)

Uchino, K., *Ferroelectric Devices*, Marcel Dekker, Inc., New York, chapter 3, pp. 62 (2000)

Uchino, K., *Ferroelectric Devices*, Marcel Dekker, Inc., New York, chapter 7, pp. 156-220 (2000)

Wang, B., K. W. Kwok, H.L.W. Chan and C.L. Choy, "Internal Field and Self-Polarization in Sol-gel Derived PZT Films", *Applied Physics A*, in press.

Xu, F., R. A. Wolf, T. Yoshimura and S. Trolier-McKinstry, "Piezoelectric films for MEMS applications", *11th International Symposium on Electrets*, pp.386-396 (2002)

Zhou, Q. F., H. W. L. Chan, and C. L. Choy, "Nanocrystalline Powder and Fibres of Lead Zirconate Titanate Prepared by the Sol-Gel Process", *Journal of Materials Processing Technology*, Vol. 63, pp. 281-285 (1997).

List of Publication

Kwok, K. P., K. W. Kwok, C. W. Tsang, H. L. W. Chan and C. L. Choy "Dielectric Characteristics of In-Plane Polarized Lead Zirconate Titanate Thin Films on Oxide Layers", *Integrated Ferroelectrics*, Vol. 54, pp. 733-739 (2003)